Advances in femtosecond micromachining and inscription of micro and nano photonic devices

Graham Neale Smith

Doctor of Philosophy

Photonics Research Group

Aston University

October 2011

Thesis summary

This thesis has focused on three key areas of interest for femtosecond micromachining and inscription.

The first area is micromachining where the work has focused on the ability to process highly repeatable, high precision machining with often extremely complex geometrical structures with little or no damage. High aspect ratio features have been demonstrated in transparent materials, metals and ceramics. Etch depth control was demonstrated especially in the work on phase mask fabrication. Practical chemical sensing and microfluidic devices were also fabricated to demonstrate the capability of the techniques developed during this work.

The second area is femtosecond inscription. Here, the work has utilised the non-linear absorption mechanisms associated with femtosecond pulse-material interactions to create highly localised refractive index changes in transparent materials to create complex 3D structures. The techniques employed were then utilised in the fabrication of Phase masks and Optical

Coherence Tomography (OCT) phantom calibration artefacts both of which show the potential to fill voids in the development of the fields. This especially the case for the OCT phantoms where there exists no previous artefacts of known shape, allowing for the initial specification of parameters associated with the quality of OCT machines that are being taken up across the world in industry and research.

Finally the third area of focus was the combination of all of the techniques developed through work in planar samples to create a range of artefacts in optical fibres. The development of techniques and methods for compensating for the geometrical complexities associated with working with the cylindrical samples with varying refractive indices allowed for fundamental inscription parameters to be examined, structures for use as power monitors and polarisers with the optical fibres and finally the combination of femtosecond inscription and ablation techniques to create a magnetic field sensor with an optical fibre coated in Terfenol-D with directional capability.

Through the development of understanding, practical techniques and equipment the work presented here demonstrates several novel pieces of research in the field of femtosecond micromachining and inscription that has provided a broad range of related fields with practical devices that were previously unavailable or that would take great cost and time to facilitate.

Dedication

To all those who have challenged, listened, read between the lines, advised and been there with me and for me with the patience of a saint.

Physics is imagination in a strait jacket ~ John Moffat

Acknowledgements

I would very much like to thank my supervisors Dr Kate Sugden (Aston University), Dr Kyriacos Kalli (Cyprus Institute of Technology) and Dr Alan Ferguson (Oxford Lasers) whose help and encouragement were invaluable in many varied ways throughout this study.

I would also like to acknowledge the financial support of the ESPRC, Oxford Lasers and DTI funded projects without their support this work would not have been possible.

My thanks also go to all the technical support that I received from Amplitude systemes, Aerotech and the engineers at Oxford Lasers. Who, at various times, have helped to make or keep the lasers and stages working.

Thanks goes to all of my collaborators; Fiberlogix with special mention to Dr Thomas Butler, Tanya Hutter of Cambridge University, Dr Peter Wooliams and Dr Peter Tomlins during their time at NPL, Charalambos Koutsides of the Cyprus Institute of Technology, Professor Geoff Tansley,

Dr Laura Leslie and Graham Lee at Aston University, Ronald Neal of Plymouth University, Dr Dimitris Karnakis and Dr Martyn Knowles of Oxford Lasers.

I would like to also acknowledge the collective support and patience of all my former colleagues from Aston University Photonics Research Group with a special mention to Bert Biggs, Ian Johnson, Tom Allsop, Andrew Main, Richard Reeves, Andrew Abbott, Karen Carroll, Yuen Chu, Mykhaylo Dubov, Jovana Petrovic, Yicheng Lai, Jim Harrison, David Webb and Vladimir Mezentsev who have contributed greatly to my learning, sanity and ability to query.

Huge thanks must go to my family for all of their patience, support and kindness throughout my many years of education.

Finally, I want to thank Dr Julia Badger for her love, patience, support and passion for research which has inspired, calmed and focused at all the key moments in the last years.

List of Contents

List of Tables and Figures

Figures

Tables

Definition of terms

Υ is the Keldysh parameter – relative balance between MPI and TI

ω is the frequency of the incident optical field

e is the charge of an electron

m_e is the mass of the electron

c is the speed of light

n is the refractive index of the dielectric

ε_0 is the permittivity of free space

E_g is the electronic band gap

I is the irradiance of the applied optical field

P(I) is the rate of photoionization through multiphoton ionisation

σ_k is the multiphoton absorption coefficient for the absorption of k photons

I^k is the k'th power of the irradiance of the applied optical field

N_t is the free carried population at a time t

N_0 is the initial free carrier population

τ is the cascade time constant

t is the time

E_p is the pulse energy

τ_p is the pulse duration

n_0 is the initial refractive index

z is the propagation direction

Δn is the relative change in refractive index

Λ is the physical pitch of the refractive index profile

n_{eff} is the effective refractive index of the propagating mode

λ is the reflected wavelength

λ_m is the reflected wavelength of the m^{th} order

m is the order of the grating

R is the strength of reflection for a fibre Bragg grating of given length and wavelength

l is the length of the grating

κ is the coupling coefficient of a given grating

M_{power} is the fraction of a fibre mode power propagating in the fibre core

V is the normalized frequency of a fibre

F is the dimensionless load capacity*

F is the load capacity (N)

R outer radius (metres) also written as r_0

r_i is the inner radius (metres)

η is the viscosity (mPa.s)

ω is the angular velocity (radians/second)

h_0 is the film thickness (m)

h_2 is the groove depth of the spiral bearing

δ is the ratio between h_0 and h_2

H is the ratio between δ and $1+\delta$

g_1 is defined in Appendix B

C_2 is defined in Appendix B

a is the groove angle of the bearing

θ is the angular position around measured from the rotational central axis of the bearing

k is the number of grooves

ΔD is the ratio of inner radius to outer radius

Λ_{pm} is the phase mask period

φ_i is the incident angle of illumination

φ_m is the angle of the diffracted order

λ_w is the wavelength of the UV beam used for writing

Λ_{fringe} is the separation of the pattern of interference of the two orders from a phase mask

Δetch-depth is the depth of phase mask structure

$\lambda_{incident}$ is the incident wavelength on the phase mask

Z_T is the Talbot distance – distance at which the wavefront is replicated in periodicity

a_2 is the period of the grating (out of phase spacing)

C_0 is the amplitude of the electric field of the 0^{th} order

C_1 is the amplitude of the electric field of the 1^{st} order

λ_{UV} is the UV inscription wavelength

Λ_Z is the period resulting from 1^{st} and 0^{th} order interaction

$N_{eff}(\lambda)$ is the effective refractive index of the core propagating mode

$n^i_{clad}(\lambda)$ *is the refractive index of the i^{th} cladding mode*

T_i is the minimum transmission of a long period grating attenuation band

κ_i is the coupling coefficient of the i^{th} order cladding mode

L is the length of the long period grating

1 Introduction

Femtosecond micromachining and inscription uses focussed femtosecond laser pulses to fundamentally change materials through the interaction of the pulse and material. The fabrication of intricate microstructures on the surface of opaque materials, or within the bulk volume of optically transparent glassy or polymeric materials, is widely recognized as an important development in the innovation of advanced components in fields such as medicine (stent production) and photonics (micro-devices, sensors). This chapter sets out to introduce the topic of femtosecond laser micromachining and inscription of different materials and will focus on the practical considerations of the subject.

A femtosecond, often shortened to fs, corresponds to 10^{-15} of a second and in femtosecond laser machining specialised lasers generate extremely high intensity pulses, where each pulse has a temporal duration that typically ranges between 50 to 500fs, which subsequently interact with materials. This interaction has a number of interesting properties that can be utilised in shaping and permanently changing the physical, chemical and optical

properties of the material. Recent advances in the development of femtosecond laser sources have accelerated the growth of this field resulting in many exciting novel applications.

The extremely short temporal profiles of femtosecond laser pulses, when combined with tightly focusing optics, produce sub-micron scale material changes that are associated with the parts of the beam where the optical intensity is extremely high, typically reaching $10^{13}W/cm^2$. Under such conditions, intensity-dependent non-linear absorption processes, such as multi-photon absorption and avalanche ionisation take place, leading to permanent structural and chemical changes in a myriad of materials. This is particularly important for transparent materials since they have electronic band gaps too large to bridge with a single photon process and therefore the linear absorption of laser light does not occur. As a result of this there is minimal interaction between the laser and material; however, with a tightly focused femtosecond laser beam the interaction can be triggered and the non-linear effects dominate. Any structuring therefore only occurs around the laser focus and has strong spatial confinement. The induced structural changes can take many forms; index change and void creation are two common examples and can be used to form true 3-dimensional structures. This is only possible because of the non-linear behaviour of the pulse-material interaction at the focus.

In this chapter we discuss the following subject areas: the key concepts of femtosecond pulse and material interaction; the materials that are used as

machinable substrates; a review of the types of femtosecond lasers that are commercially available; an introduction to some techniques applied in the field to date and a review of some of the current applications for this type of technology.

1.1 Fundamental considerations of femtosecond pulse-material interaction

Having first looked at the fundamentals of how femtosecond lasers interact with materials, we will look at the properties of a femtosecond laser beam and discuss a number of parameters that strongly affect the micromachining process.

When many materials are subject to femtosecond lasers exposure they are often structurally modified. There are competing models of modification with strengths and areas of knowledge gaps in each. One such model is that of the fictive temperature of a glass. Within a glass refractive index modification, as the result of femtosecond laser exposure, is the result of a series of physical mechanisms. The glass can be considered to be transparent at the wavelength of exposure, thus at low levels of fluence there is negligible interaction between substrate and femtosecond pulse. This characteristic changes at greater levels of irradiance and the light is absorbed, through multi-photon absorption, in the process ionising the local volume. At this point other ionisation processes like impact ionisation are initiated through absorption of photons by free-carriers in the substrate.

This carrier concentration increases over the duration of a femtosecond pulse. After a period of time, dependent on the material (approximately 1ps in fused silica), this localised free carrier volume transfer the energy to the surrounding glass structure resulting in heating and shockwave formation [**1**].

In the fictive temperature model the refractive index modification is a result of rapid thermal change, changing the glass fictive temperature and thus modifying the local density and refractive index [**2**]. This predicts an increase in refractive index for some materials such as fused silica and a decrease in other glasses. This rationale is supported by Raman microscopy which finds increased intensity of peaks associated with an increase in the fictive temperature of the glass [**3**]. There are a number of inconsistencies with this model. Refractive index profiles in literature are often found to have completely positive or negative index changes. This would result in a violation of the conservation of mass. The model typically is thought to only be applicable to fused silica as no other glass has been found to have truly compelling spectroscopic evidence of density changes with doubt even cast over these with femtosecond waveguides showing inconsistent behaviour with the model [**4**].

Other models for modification of the refractive index of glasses include the creation of colour centres described using the Kramers-Kronig formalism and strain produced by the localised densification. These are discussed in more detail in section 1.3.1 below.

1.2 Nonlinear excitation mechanisms

As touched upon above the nature of femtosecond pulse and material interaction is highly dependent on a range of mechanisms. The mechanisms are described below.

1.2.1.1 Ionisation mechanisms

Photo-ionisation is the term that describes the interaction between the optical field and a dielectric where the bound electrons in the valence band are promoted to the conduction band. There are two main components to this in multiphoton and tunnelling ionisation.

Before going into detail it should be noted that when absorption at near infrared wavelengths occurs through the promotion of electrons to the conduction band from a valence band a minimum energy is required, known as the materials band gap. The absorption of the light can be very dependent on a materials band gap and incident wavelength. When the photon energy is greater than that of the band gap single photon absorption dominates. This is an example of a direct bandgap process. In some materials, especially semiconductors, single photon absorption occurs even if the band gap is greater than the photon through a photon-phonon interaction, an indirect bandgap interaction, resulting in promotion of the electron whilst conserving momentum. Multiphoton absorption becomes important when the direct bandgap energy is greater than the single photon energy. This is especially the case at wavelengths being used in the body of this thesis and with transparent materials and is explored further in section 1.2.1.1.1.

1.2.1.1.1 Multiphoton Ionisation (MPI) & Tunnelling Ionisation

Multiphoton ionisation (MPI) describes the direct absorption of multiple photons by a substrate where the sum of the absorbed photons is greater than the electronic band gap of the medium; this is shown in figure 1-1b. Tunnelling ionisation (TI), shown in figure 1-1a, describes quantum tunnelling of electrons through the potential well barrier into the conduction band. This relies on a strong electric field being incident on the dielectric for this to happen. The two are not distinct processes but instead two special cases of one theoretical model, the Keldysh theory. The theory describes the two as high and low frequency components of the same model with the high being a description of MPI and low TI. The domain between the two cases describes the combination of the two processes and is commonly considered to be the general case for photo-ionisation to occur. A schematic of the three processes involved in the nonlinear photoionization mechanisms is shown in Figure 1-1

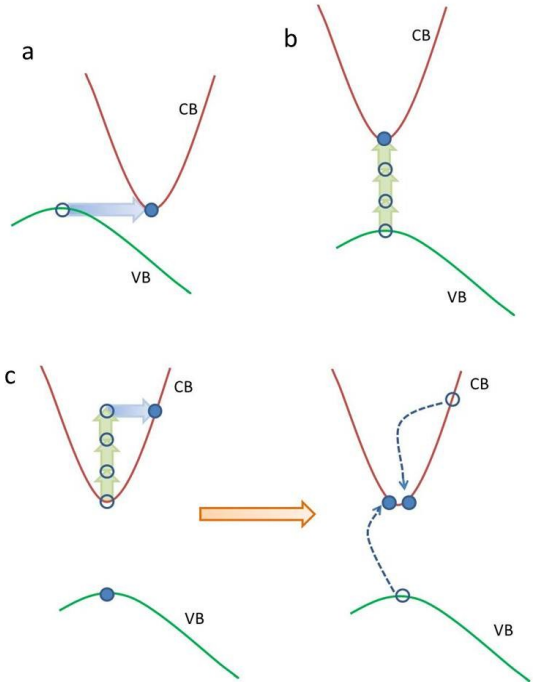

Figure 1-1 A schematic of the three ionisation processes showing a) Tunnelling Ionization, b) Multiphoton Ionisation, c)Avalanche Ionisation: Free carrier absorption with subsequent impact ionization described in section 1.2.1.2. VB – Valence Band, CB – Conduction Band.

The relative balance between MPI and TI is characterised by the Keldysh parameter, γ, where **[5]**;

$$\gamma = \frac{\omega}{e}\sqrt{\frac{cn\epsilon_0 E_g m_e}{I}} \qquad \text{Equation 1-1}$$

Where ω is the frequency of the incident optical field, e and m_e are the charge and mass of an electron, c is the speed of light, n is the refractive index of the dielectric, ϵ_0 is the permittivity of free space, E_g is the electronic band gap and I the irradiance of the applied optical field.

Tunnelling occurs when $\gamma < 1$, multiphoton ionisation occurs when $\gamma > 1.5$ and the intermediate state is when $1 < \gamma < 1.5$. Thus, from the Keldysh formula, when the frequency ω approaches infinity so too does the Keldysh parameter leading to multi-photon ionisation. As ω tends to zero so too does the Keldysh parameter and so tunnelling ionisation corresponds to small values of the parameter. So for a fixed frequency the parameter becomes large with low irradiance and small at high. Thus, MPI is expected at low irradiance and tunnelling at the high limit. If the incident frequency and irradiance are fixed then the parameter is scales with the bandgap of the dielectric material. Thus when then lower bandgap materials are irradiated tunnelling ionisation is more dominant.

The rate of photoionization depends largely on the intensity of the irradiating laser. In the MPI regime the rate is given by;

$$P(I)_{MPI} = \sigma_k (I/h\nu)^k \qquad \text{Equation 1-2}$$

Where σ_k is the multiphoton absorption coefficient for the absorption of k photons. This requires that the minimum number of photons, k, is met so that $k\hbar\omega \geq E_g$. The tunnelling rate does not scale as strongly with the laser intensity than the multiphoton rate does [**6**].

1.2.1.2 Impact or avalanche ionisation

During photo-ionisation many electrons are liberated from their bound states. The incident laser electromagnetic wave is absorbed by these free electrons through a mechanism called inverse Bremsstrahlung absorption [**7**]. Once enough energy is absorbed from the incident radiation free

carriers are liberated through collision based exchanges of energy. This process is called impact ionisation and is unlike photo-ionisation as it is dependent on the free carrier density of a substrate. This means that it grows exponentially with time of irradiation hence referral to it as avalanche ionisation. The free carrier population, N as a result of impact ionisation is given by;

$$N(t) = N_0 e^{t/\tau} \qquad \text{Equation 1-3}$$

Where N_0 is the initial free carrier population, τ is the cascade time constant and t is time. The cascade time constant is linked closely to the irradiance of the incident EM field. As a result of the exponential growth impact ionisation is understood to be the protagonist mechanism over photoionization. The initial seeding of free carriers by photo-ionisation is key though as it determines the initial free carrier population.

It is commonly taken that avalanche ionisation is the mechanism that results in damage within glasses. Pulse durations longer than approximately 250fs [**8**,**9**,**10**] are considered to have significant avalanche ionisation effects. The bulk of the work in this thesis was carried out with pulse durations longer than this and as such resulted in being caused by avalanche ionisation.

1.3 Energy transfer

Irrespective of the physical mechanism ionisation processes give rise to energy being exchanged from incident EM radiation to medium. This

typically results in a localised free electron gas, a Fermi gas, the energy of which is in time redistributed in the local bulk medium. This typically takes place through electron-phonon coupling. The time that it takes for this redistribution is comparatively large as against the time nonlinear absorption processes time scale. This typically means that it is considered as a non-coupled process in the femtosecond regime [**11**]. The end result is that the electrons have a large differential temperature to the bulk lattice. The way that an individual material behaves in the presence of a large non-equilibrium state characterises the modification created.

1.3.1 Modification regimes

There are three common states of post femtosecond exposure material modification in transparent materials. At either extreme of the threshold behaviour are smooth index changes and void creation. The intermediate case is the creation of birefringent refractive index change. Through the multiphoton processes for a fixed pulse duration, laser wavelength and objective lens (and hence NA) the variation of laser pulse energy determines the modification regime for a given substrate exposed to femtosecond laser radiation. The two regimes of most interest to this thesis are the two extreme cases and are the topic of further discussion.

1.3.2 Index change

At just below the threshold for material damage the highly localised femtosecond irradiation creates rapid thermal variation and subsequently material modification [**12**,**13**,**14**]. This rapid heating and cooling, as discussed earlier in section 1.1 in discussion of the fictive temperature model is believed to lead to density and refractive index changes. These

changes are, as such, dependent on the material and laser parameters giving different magnitudes and polarities of refractive index response.

It is thought that in fused silica the response of the material to femtosecond pulses is a density increase through quenching mechanisms post energy deposition [**15**,**16**,**17**]. This increase in the density gives a rise in the refractive index of around 10^{-2} to 10^{-3} [**18**,**19**] as compared to the unmodified bulk of the glass. Other glasses have different thermal diffusion coefficients and as such respond differently leading to different index changes. This supports the rational that the index change is thermal. However, low power high repetition rate and high power low repetition rate lasers are able to induce comparable index changes in spite of quite different inscription temperatures being reached [**20**]. This would suggest that the fictive model is not the only process determining the refractive index change.

One proposed mechanism considers that femtosecond pulses induce colour centres the formalism of which is derived through the Kramers-Kronig relation governing the physical response of a system to an given force, in this case incident radiation and subsequent dissipation of energy out of phase with the incident light within the media of concern [**21**,**22**,**14**,**23**,**24**,**25**,**20**]. This suggests that colour centres are created in sufficient quantities to modify the refractive index. The process relies upon the nonlinear absorption creating a high electron density which in turn leads to concentrations of trapped species known as colour centres. This is

considered to result in a modification in the types of defects found in the exposed volumes. The practical examinations of this in fused silica show resonances at wavelengths associated with the creation of self-trapped exciton defects and non-bridging oxygen hole centres. This provides evidence of colour centre formation which may in turn contribute to refractive index modification. The relative amounts of index change are small compared to the thermal model as annealing processes do not recover the base refractive index in femtosecond modified regions [**19**,**26**].

It has been shown that femtosecond radiation can also lead to densification and subsequent strain in a glass medium which may contribute to the change in refractive index seen [**27**]. What was found by examination of fused silica samples to Raman spectroscopy techniques was that the ring structure (discussed in more detail in section 1.5.1) became more 4 and 3 fold Si ring structures from the unmodified 5 and 6 fold [**28**,**29**,**30**,**31**,**32**]. For this to occur the energy levels of the silica structures have to be more elevated which would happen through the nonlinear processes of femtosecond irradiation. The resulting changes in bond angles give a densification in the modified region leading to refractive index change. This change has been found to be permanent in nature. With the densification of an irradiated volume of material the surrounding bulk experiences stress. These create birefringence and if the densification is approximated to be uniform are able to be related to the level of densification. Through this approach the refractive index change associated

with densification is not believed to account for all of the modified change in refractive index [**18**,**20**].

The resultant refractive index change is understood to be a consequence of all of the above processes and although this has not been fully resolved is considered to be sufficient understanding to fabricate photonic devices using it.

1.3.3 Void creation

At large intensity irradiation the modification created within a bulk transparent material is characterised as being a void. This is created by the formation of plasma through avalanche ionisation at the focal volume [**33**,**34**]. With increased energy in the exposed volume the plasma temperature rises and a highly localised increase in pressure is created. At sufficient energies this results in Coulomb repulsion creating a micro explosion and shock wave [**33**,**34**]. Within the bulk of a material this creates a central rarefaction and densified shell commonly known as a void [**35**,**36**]. Within a bulk these voids are used to create photonic structures such as fibre Bragg gratings and are used as such in this thesis. They have also been used to create structures for OCT calibration artefacts in chapter 4.3.

1.4 Ablation mechanisms

As discussed in section 1.3.2 when the conditions for void creation are met and the energy incident in the focal region is sufficient to create plasma with sufficient energy for Coulomb repulsion to create voids, ablation may occur. The only difference is the depth at which the changes occur. If near enough the surface the plasma will inevitably weaken the surface wall

allowing the pressure on the side walls to be reduced in due course. This causes the removal of material from a substrate and is characterised as ablation.

1.5 Chemical structures of fused silica and borosilicate and glass modification with femtosecond exposure

The composition and structure of both fused silica and borosilicate glass is of consideration as a large amount of the practical work carried out was in either of these glasses.

1.5.1 Fused Silica

The pure form of silica glass fused silica has many useful properties such as its high mechanical stability, high softening temperature at approximately 1100K and is largely chemically inert. The underlying reason for this stability is the structure of amorphous covalent bond structure of silicon and oxygen atoms. Each silicon atom has four oxygen atoms bonded to it in a tetrahedral arrangement where each silicon atom is bonded to two silicon atoms. The bonding of the two silica atoms to an oxygen atom is referred to as bridging oxygen in glass chemistry. It is the tetrahedral arrangement of these atoms that gives fused silica the high degree of stability [**37**]. The arrangement also means that the silicon and oxygen atoms complete their outer energy level shells and thus do not readily react. This is the case for all but extremely electronegative ions such as fluorine which are able to break down the bond structure and is the reason for using acids such as HF or ABF to work with fused silica.

The optical qualities of fused silica, such as refractive index and density are largely dependent on the thermal history of the glass [**15**]. These are often a product of the processes used to make the substrates with different types of fused silica exhibiting different refractive indices and impurity levels leading to different transmission characteristics. Fused silica contains OH as a result of its fabrication and the amounts of this vary from single to over 1000 ppm. This OH bond is relatively much weaker and is broken forming what are called non-bridging oxygen hole centres (NBOHCs). These formations are optically active and contribute to the refractive index of the glass. Other common impurities include Al, Ca, Fe, Na and Cu but at concentrations of around 0.1 ppm.

1.5.2 Borosilicate glass

Borosilicate glass is a commonly used glass and is often chosen because of its low thermal expansion coefficient. Borosilicate glass is composed of silicon and boron oxides. Unlike fused silica this alone does not make them inert and so other elements are added, typically sodium or potassium to chemically stabilise the glass. Borosilicate has a similar structure to fused silica; the boron atoms replacing the silicon ones forming networks of bonds. The electron valence of boron leads to it naturally wanting to form BO_3 triangles hence the use of alkali metals to create more stable tetrahedral BO_4 structures. Borosilicate glasses often show a degree of medium range order that fused silica does not.

1.6 Experimental factors that affect the interaction

There are a number of experimental factors affecting the femtosecond pulse and material interaction. The key ones are briefly discussed below.

1.6.1 Repetition rate

The effect of the pulse repetition rate on the material-pulse interaction is shown to have a significant effect on the profile of the index change at higher repetition rates (typically in the MHz region). This is shown to be due to the thermal diffusion of the material being longer than the pulse to pulse separation [24]. This means that the material is thermally loaded when the next pulse is incident at the focal region. This effect has not been observed at lower repetition rates in the kHz range.

1.6.2 Write direction

The choice of write direction and objective lens are critical to determining the characteristics of a femtosecond inscribed or ablated substrate. The two key writing geometries are longitudinal and transverse writing and are parallel and perpendicular in translation direction relative to the beam path. The work presented here uses transverse writing. This is because the long working distances required of the low NA lenses and spherical aberration degradation to the beam quality generated through the amount of medium the beam has to penetrate make it unattractive for the work carried out. These are avoided by using the transverse writing technique, however, with low NA lenses an amplified laser when focused can result in a focal asymmetry. This can lead to elliptical cross-section which, although can be compensated for can by slits [**38**] or lenses, leads to asymmetric index profiles.

It should also be noted that when writing structures it can often be useful to write in the same direction relative to the field. This can be due to factors such as pulse tilt and material structure. However, for a number of the samples written and presented here this was not applied as the write times would become excessively large for an individual device, for example when writing phase masks (section 4.2).

1.6.3 Polarisation

It has been shown that the rate of photo-ionisation is affected by the polarisation state of the incident radiation. The selection rules that apply to linearly and circularly polarised light result in different ionisation cross-sections. Initial experimental work showed that the ratio of cross sections, σ_c/σ_l where σ_c is the ionisation cross section for circularly polarised light and σ_l is the ionisation cross section for linearly polarised light, to be 2.15 ± 0.4 [**39**]. Theoretical predictions of this have been based on perturbation theory and result in comparable numbers [**40**]. The effect has also been shown to be dependent on the number of photons being absorbed [**41**,**42**]. The models and latest practical work suggest that the ratio is greater than 1 if $N < 4$ and less than 1 if $N > 5$ [**43**,**6**,**44**], where N is the number of absorbed photons. This supports the idea that as N becomes large the cross section ratio tends to zero. This works on the assumption that the photo-ionisation processes are dominated by MPI [**6**].

In terms of femtosecond laser polarisations effect on optical properties it was demonstrated that when waveguides were written with circularly polarised light they induced greater index change and subsequently lower

transmission losses [**45**]. The area is still of some contention and is an area that will need further examination to be fully understood.

1.6.4 Self-focusing and filamentation

Transparent materials have an intensity dependent refractive index known as a Kerr non-linearity. This takes the spatial variation of intensity across a laser beam and if above the critical power for the medium creates a spatial variation in the refractive index across the beam diameter. This apparent index modification acts as a focusing lens to the beam and is known as self-focusing. As the beam radius decreases the effect increases leading to the beam focusing itself before the intended geometric focus or indeed collapsing in the most extreme cases. Practically the effect of self-focusing can be negated through the use of high NA lenses and by keeping the laser peak power low. This works by achieving the intensity dependent material modification threshold whilst being below the power threshold for the Kerr effect to take hold.

In contrast to self-focusing plasma self-defocusing is able to be induced during femtosecond pulse material interactions. It requires the number of free carriers, created during photo-ionisation, to be sufficient to that at focus the plasma creates an effective reduction in the refractive index. This acts to defocus the laser beam. The two effects can be balanced, creating beam waists that last over several Rayleigh lengths and this is called filamentation [**46**,**47**,**48**,**49**,**50**,**51**,**52**,**53**,**54**,**55**]. This process can lead to excessive undesired damage and so has not been sought in the work in this thesis.

1.6.5 Pulse duration

The duration of the pulse incident on the material is critical to the nature of the pulse-material interaction. When the thermal response behaviours are in the nano and micro second time domain a pulse duration of around 1ps and below does not interact concurrently with the material thermal processes [**56**,**57**]. This enables the interaction to be largely athermal leading to less heat affected zone and a more Gaussian distribution of index modification.

The pulse duration also scales the maximum peak power through the relation

$$peak\ pulse\ power \approx \frac{E_p}{\tau_p} \qquad \text{Equation 1-4}$$

Where E_p is the pulse energy and τ_p is the pulse duration. This exact relation is dependent on the pulse shape for the exact relation, for example for a $sech^2$ pulse it has a factor of 0.88. This strongly affects the interaction of a pulse with a given material as the interaction is dependent on the peak pulse power relative to the modification and ablation.

1.7 Materials

One of the least understood, yet most crucial aspects of femtosecond micromachining is the precise nature of the interaction of the laser pulses with the substrate materials. The material properties affect the plasma as it

interacts with it. Materials can be divided into two groups for classification, transparent and non-transparent. Figure 1-2 shows a range of both types of materials and their ablation/damage thresholds. The values for the material thresholds are taken from published work and are for a number of different wavelengths and pulse durations [**58**,**59**,**60**,**61**,**62**,**63**,**64**,**65**,**66**,**67**]. The values can be used to illustrate the general trends but should not be taken as finite points.

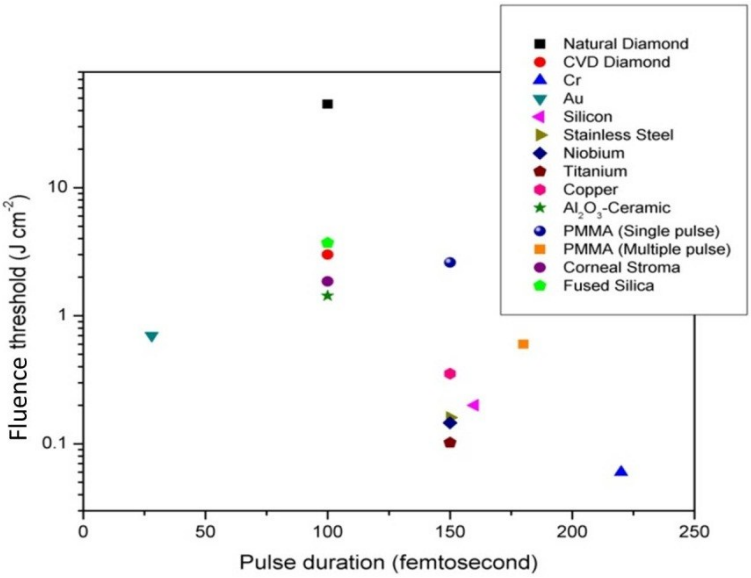

Figure 1-2 A plot of the energy thresholds for modification vs. pulse duration, for a range of materials, with the values taken from a literature survey.

Most material thresholds have a small range of values attributed to them arising from the laser parameters and techniques being applied being different between groups conducting the research. A good example of this is given in the paper by Sanner et al [**67**], where the range of values quoted

for the ablation threshold for fused silica is given as 2-12 J cm^{-2}. This range is by no means an anomaly or the widest range published, for example the value for natural diamond is given as 10-80 J cm^{-2} [**60**] where the value fluctuates widely across a specimen surface. The reason for the range in values can be explained by considering that there are a number of ways of measuring the thresholds and even defining them [**67**], there are also differences in the exact composition of the materials used and their source, as well as differences in the experimental set-up. The variation in material and the dependence on small variations of impurities and dopants can lead to significantly different thresholds. The values also do not reflect the range of repetition rates that are available and the subsequent change in energy threshold [**68**,**69**]. There is also a dependence on the wavelength of the laser as this will determine the physical mechanisms involved from multiphoton absorption, impact ionization, free carrier absorption and many others.

It should be noted that the chart also reflects the work carried out using the lasers that have been practically available in laboratories around the world. The vast majority of these systems have a repetition rate of about 1 kHz and are Ti: Sapphire amplifier lasers. This will potentially bias the results of the plot as the lasers that may be best suited to a given material may not be reflected in the work carried out to date. A good example of this may be Poly(methyl methacrylate) **(**PMMA) where at the correct wavelength a particularly short pulse may suit the material in which the chain length of the molecules is long and the thermal sensitivity is high. The short pulse

duration would potentially enable the confinement of the resultant shockwaves to be significantly greater.

1.7.1 Non-transparent materials

As one would expect, the use of femtosecond lasers with non-transparent materials is typically limited to working on the surface in either ablation or modification [**70**]. There are a number of non-transparent materials that have been studied as shown in Figure 1-2. Each material has a number of different properties that affect the energy threshold. For non-transparent materials, the band gap is the most important contributor when looking to determine the energy threshold. This will, as detailed in section 2.1, determine the process by which the photons interact with the material. The interaction of femtosecond pulses with non-transparent materials causes excitation of the majority of electrons, creating a plasma-like state which immediately creates disorder in typical lattice structures. This means that the process is typically considered to be athermal as it occurs before the lattice has come to an equilibrium state through the carriers. There is some debate as to exactly how athermal the process is but there is little disagreement that the reduction of the heat affected zone (often abbreviated to HAZ) is significant as compared to the longer pulse durations that had previously been studied [**71**]. It should be noted that in the case of metals because the valence and conduction bands overlap the density of electrons is already ≥1. In this case the absorption coefficient, from linear absorption, is typically high (of the order of 10^5-$10^6 cm^{-1}$) corresponding to small skin depths of 10-30nm. In this instance the non-linear absorption becomes much less important. This is often true of a

range of non-transparent materials outside of the semiconductor family, where competition and interference between non-linear and linear processes is more readily seen. The potential for the use of non-transparent materials, either on their own, in multi-layered combinations or, in combination with dielectric materials, for a range of applications holds a great deal of future development capacity and will be a subject of continued research for a number of years to come.

1.7.2 Transparent materials

Transparent materials also rely on non-linear absorption and subsequent ionization to create either ablation at the surface or index modification within the bulk. The exact mechanisms are not fully determined. However, work on modelling the processes involved is beginning to compare well with practical results and illuminate the mechanisms [**72**]. The mechanism for the energy transport from pulse to material is commonly thought to be through nonlinear absorption. A femtosecond pulse of sufficient energy when focused inside a material will optically breakdown. At this point a proportion of the energy is transferred to the lattice via excitation of the electrons in a multiphoton absorption process. These electrons reach thermal equilibrium within several femtoseconds and seed the subsequent avalanche ionisation which absorbs the energy in the tail of the pulse. It is assumed that the energy that does not go into the ionisation is stored as kinetic energy in the electrons. The recombination time for electrons in fused silica is of the same order as most of the pulse durations as shown in Figure 1-2 at 170fs [**73**]. It is commonly assumed that the mechanical and thermal changes on the time scale of a pulse are negligible. In the next

picosecond a proportion of the energy in the electrons is transferred to the lattice. During this time there is plastic deformation occurring which propagates at the speed of sound covering about a micron in 0.1ns. This pressure or shockwave separates from the hot focal volume in a matter of nanoseconds. This is then followed by thermal diffusion acting in the microsecond timescale where the thermal energy diffuses out of the focal volume. Beyond critical energies these processes give rise to permanent changes in structure that creates one of two commonly accepted forms in the shape of voids [**74**] or smooth index changes [**75**]. The difference between the two depends on whether the pulse is above or below the damage threshold of the material concerned.

Void creation is achieved when the focusing is very tight and the pulse energies used are high. This has the effect of creating huge pressures at the point of focus and subsequently on the surrounding material. The surrounding material experiences a pressure wave moving away from the peak intensity forming a rarefied region of material followed by a region of densification. When the pressures created, through the focusing and pulse energy, are great enough a void may be created [**76**].

Smooth index changes are achieved with pulses below the structural damage threshold. They too create rarefied areas; however, as the pressure exerted by the focal volume is much smaller the resultant index change gradient is smoother leading to structures that can be used for waveguiding. The effect of the pulse repetition rate on the material-pulse

interaction is shown to have a significant effect on the profile of the index change at higher repetition rates (typically in the MHz region). This is shown to be due to the thermal diffusion of the material being longer than the pulse to pulse separation [**69**]. This means that the material is thermally loaded when the next pulse is incident at the focal region. This effect has not been observed at lower repetition rates in the kHz range.

It should be noted that there are competing mechanisms for explaining the effects of pulse material interaction such as tunnelling ionization; however, work by Keldysh has shown that they are just two boundaries of the same process under different conceptual approaches [**77**].

1.7.3 Heat Affected Zone

The nature of the timescales involved in both transparent and non-transparent material interactions with femtosecond pulses, and the subsequent structural changes, offer up insight into the advantages of micromachining with ultrashort pulsed lasers. The electron-phonon scattering time, of approximately 1 picosecond, is greater than the pulse duration and so the pulse has ended before the excitation of the ions has begun. This means that theoretically the heat diffusion outside of the focal area is minimized [**71**]. This extra control on the locale of micromachined change adds a level of precision not afforded to lasers of >50ps pulse duration. This reduction in the heat affected zone is often important in many applications. The reduction can lead to fewer, if any, micro-stress fractures being created when machining materials which, for example, are used for heavy strain loading thus reducing the chances of fracture. Also, to

induce changes in a material using a femtosecond laser it is not necessary to have dopants to seed the absorption process. The effect of the nonlinear ionization can be used, with great care and refined technique, to produce a confined and reproducible material change that can be put to practical use.

1.8 Fibre Bragg grating and Long Period Grating theory

Gratings are periodic structures used to modulate the propagation of light with periods ranging from between 100nm-100μm. Using constructive and destructive interference the manipulation of light is broadly classified into fibre Bragg gratings (FBG) and long period gratings (LPG) at nm and μm periodic structures. Whilst the fundamentals are well understood for UV inscribed periodic structures in doped glass fibres the use of femtosecond lasers is a relatively recent and an area of on-going study. The use of direct-write point by point written gratings is the subject of further discussion in chapter 5; however, a summary of the basic theory applied to each is discussed below.

1.8.1 Fibre Bragg grating theory

Fibre Bragg gratings are periodic refractive index modulations that act as a wavelength selective mirror within the core of an optical fibre. Typically gratings are assumed to have a sinusoidal refractive index profile, models developed around UV modification that act as a useful first approximation in femtosecond direct-write point by point (PbP) inscription. Taking a sinusoidal model the index profile can be described as;

$$n(z) = n_0 + \Delta N \, sin(2\pi \, z/\Lambda) \qquad \text{Equation 1-5}$$

This leads that the wavelength specific reflection is given by;

$$\lambda = 2n_{eff}\,\Lambda \qquad \text{Equation 1-6}$$

Where λ is the reflected wavelength n_{eff} is the effective refractive index of the propagating mode and Λ is the physical pitch of the refractive index profile.

The model for more realistic, non-sinusoidal refractive index profiles, give rise to the recognition that more than one reflected wavelength can propagate. The number of reflected wavelengths is proportionate to the number of Fourier components present in the index modulation. This is described by;

$$\lambda_m = 2n_{eff}\,\frac{\Lambda}{m} \qquad \text{Equation 1-7}$$

Where λ_m is the reflected wavelength of the mth order, gratings are referred to as mth order gratings. There is a trade-off between the strength of the gratings, related to the number of periods in a given grating length, and the ability to physically modulate the refractive index in a given pitch. This is an area of especial interest to femtosecond inscribed PbP gratings that on the whole prefer to write 2nd or higher order gratings.

Using coupled-mode theory [78] the strength of reflection for a uniform sinusoidal grating of a given length l, wavelength λ and coupling coefficient κ is given by;

$$R(l,\lambda) = tanh^2(\kappa l) \qquad \text{Equation 1-8}$$

Where the coupling coefficient κ is given by;

$$\kappa = \frac{\pi\Delta n}{\lambda} M_{power} \qquad \text{Equation 1-9}$$

Where M_{power} is the fraction of fibre mode power propagating in the fibre core, approximated to 1-V^2 (where V is the normalized frequency of a fibre) and Δn is the amplitude of refractive index modification. The result of this is that as the change in refractive index of an index increases, so too does the grating strength. The same can be said of the length of the grating.

1.8.2 Long Period grating theory

Where typically FBG periods of a few hundred nanometres are common, long period gratings have periods of the order of hundreds of microns and overall lengths of several centimetres. These structures create coupling to modes that are propagating in the same direction. The resulting coupled modes are either higher order or cladding modes in multimode and single mode fibres respectively. In the case of the single mode fibre this introduces what is in effect a loss. This loss is dependent on the interaction between the mode and the cladding material and evanescent coupling to the surround media. This has uses in sensing as the wavelength sensitivity is extremely dependent on the surrounding environmental conditions [**79**,**80**].

Through direct write inscription femtosecond LPG can be produced with a range of periods that are highly tuneable. These index changes are inscribed while the use of precision motion stages and shutters control the periods inscribed.

1.9 Goals of the research

In this research I have hoped to progress the state of the art in both micromachining and its use with direct write inscription based techniques

to create devices for sensing and other applications. The work embodied here explored what can be achieved in mostly transparent materials as a means making these devices compatible with existing integrated arrangements. The work starts with the development of micromachining techniques in the planar, as shown in the early sections of chapter 3, with the regular geometric space that affords and moves into making more complex structures utilizing the techniques developed in the later sections of this chapter to facilitate the production of devices for other experimentation in microfluidics and chemical sensing. In chapter 4 the work moved into the inscription parameter space and was used to initiate and develop femtosecond written phase masks and OCT phantom artefacts. Chapter 5 moves to combine the knowledge base built up from the work demonstrated in chapters 3 and 4 to a more complex geometry of the fibre optic. This cylindrical geometry posed extra complications to the standard techniques which had to be overcome. The work then finishes with a combination of both inscription and ablation in the same practical device for the detection of magnetic field strength using wavelength sensing.

2 Practical systems used

2.1 Laser processing systems and techniques

2.1.1 Types of femtosecond laser available

The results of a market survey on femtosecond laser sources are presented in Table 2-1 (Amplitude Systemes; Coherent; High Q laser; Kapteyn-Murnane Laboratories; Raydiance). There are a number of ways of evaluating femtosecond lasers, each parameter set leading to a different profile of applications that they suit. The parameters chosen for this summary are wavelength, energy per pulse, pulse width, repetition rate, average power and the key amplification medium of the source. There are, of course, other parameters that are also fundamental but for reasons of space have not been included for example, the M^2 value, peak power, beam diameter and polarization. These parameters should not be overlooked, however, when considering which laser source is applicable to a given task.

The M^2 factor, also known as the beam quality or beam propagation factor, is commonly used as a measure of the beam quality [**81**]. For diffraction

limited Gaussian beam the divergence is thus given by:

$$\Theta = M^2 \left(\frac{\lambda}{\pi\omega_0}\right) \qquad \text{Equation 2- 1}$$

where Θ is the half angle beam divergence, λ is the wavelength and ω_0 is the beam radius at the beam waist. A diffraction limited beam has an M^2 of 1 and is considered Gaussian. The level of divergence that a beam has will limit the degree to which it can be focused and since the M^2 factor is a measure of this it is a good indication of how a laser beam will focus given a certain numerical aperture objective lens. When combined with the optical power of a laser it determines the laser fluence achievable. Typically femtosecond lasers will have an M^2 value of between 1 and 1.5, in most applications a value closer to 1 is usually preferable.

The peak power is a parameter that is typically considered when deciding what material you wish to ablate or into which you wish to inscribe a structure. The key being that the peak power must exceed the material threshold energy so that work may be carried out. This can be done by comparing the many sources of material thresholds (see Figure 1-2 for published results) against the specifications of the systems supplied. The peak pulse power, ppp, is given by:

$$ppp = F.\frac{Average\ power}{Repetition\ rate.\tau_p} \qquad \text{Equation 2- 2}$$

where $\tau_p$is the pulse duration and F is a factor determined by the shape of the pulse; for a $sech^2$ pulse the factor is 0.88, for a Gaussian it is 0.94.

The beam diameter needs to be taken into consideration when designing the optics that a femtosecond laser system will require or, of course, vice versa. It is important to control the beam divergence and aperture size of the lens as through miscalculation of these much of the beam quality, wavefront, energy profile and peak energy may be lost or reduced.

Most of the sources in table 1 are linearly polarised. Although the polarisation is not generally an issue, care should be taken when designing the system to make sure that the polarisation for any beam is known at any given point. As an example, when using an autocorrelator to monitor the laser, an orthogonal polarisation state may be required to that which your laser outputs. There is also work on the polarisation state relative to the direction of beam-substrate translation; this was covered in more detail in section 1.6.3.

There are currently two key types of femtosecond laser commonly commercially available. They may be grouped into amplifier and oscillator systems. The details as to how they work will not be covered here but may be found in references [**82**,**83**]; however, differences in terms of the output pulses will be discussed.

The wavelength ranges of the types of laser are determined by a number of factors. There are two main bands covered by the fibre lasers at 1030-1045nm and around 1550-1560nm. The two bands correspond to the dopant used in the lasers cavities. The conventional C-band erbium window is at 1530-1565nm and ytterbium sources operate at around 1030-1050nm [**84**].

There is a third much smaller group of fibre lasers operating at around 800nm. Bulk amplifiers and oscillators, are also governed by the amplification material chosen. They typically use Ti: Sapphire and ytterbium and as such commonly operate at wavelengths around 800nm and 1030-1050nm.

The energy per pulse is a parameter to be considered in a similar way to the peak power. The pulse energy required will depend on both the material and the chosen application. Machining of a crystal for instance will typically require a much greater energy per pulse, for example fluences up to and above 80 Jcm^{-2} **[60]** for natural diamond, while for index change in PMMA fluencies above 0.6 Jcm^{-2} **[64]** cause permanent change. The energy per pulse of these types of laser is detailed in Table 2-1. The oscillators typically have energies in the range of 1-100s nJ per pulse, whereas the fibre lasers offer energies in the μJ range and amplifier pulse energies typically fall in the mJ range. The choice of pulse energy for a given application is critical as most materials have a small window of energies between the desired effect, say index change, and damage. The other consideration is that to control the energy, and other parameters, incident on a sample is significantly easier when not having to operate at the extreme limits of attenuators or with insufficient laser energy after the losses experienced through the system.

Type	Wavelength (nm)	Energy per pulse	Pulse width (fs)	Repetition rate	Average power (W)	Key material	Company
Amplifier	800	0.3-6mJ	25-130	1 or 5 kHz		Ti:Sapphire	Coherent
Amplifier	1030	10μJ-1mJ	400-500	0-100kHz		Diode pumped	Amplitude
Amplifier-multi pass	Tuneable	0.25-20mJ	<25-100	1-20 kHz	3.0 to 50	Ti:Sapphire	Kmlabs
Amplifier-Regen	1035	0.4-1mJ	350-500	1-100kHz	1.0 to 2.0	Ytterbium	High Q
Amplifier-Regen	1055	1mJ-5μJ	650	10-100kHz	0.100 to 0.200	Nd:Glass	High Q
Amplifier-Regen		3mJ	60-160	100/250	0.3 to 0.75	Ti:Sapphire	Coherent
Fibre	780		100	50MHz	0.02	Erbium doped	IMRA
Fibre-Amplifier	810		<150	75MHz	0.1	Erbium doped	IMRA
Fibre	1030	0.5-10 μJ	100-700	30-2MHz	20		Amplitude
Fibre	1043	2μJ	500	200KHz	0.4	Ytterbium doped	IMRA
Fibre	1043	10	700	200KHz	3W	Ytterbium doped	IMRA
Fibre	1045	10μJ	700	100kHz		Ytterbium doped	IMRA
Fibre	1552	1-10 μJ	<800	1Hz-300kHz	3		Raydiance
Fibre	1552	5-50 μJ	<800	1Hz-100kHz	5		Raydiance
Fibre	1560		100	50MHz	0.06	Erbium doped	IMRA
Oscillator	800	3-10nJ	<12	80-100MHz	0.250 to 0.900	Ti:Sapphire	Kmlabs
Oscillator	800		<20	80MHz	>0.300	Ti:Sapphire	Coherent
Oscillator	1030	20-500nJ	200-500	10-50MHz	1 to 5	diode pumped	Amplitude
Oscillator	1060	1.4nJ	<150	72MHz	>0.100	Nd:Glass – diode pumped	High Q
Oscillator	1030-1053	2-300nJ	~350	10-80MHz (fixed)	0.150 to 3	Ytterbium	High Q
Oscillator	790-870		100-300	73MHz	>0.200	Ti:Sapphire	High Q
Oscillator-Cavity dumped	800	>60nJ	100	0.5-1MHz	0.06	Ti:Sapphire	High Q
Oscillator-Cavity dumped	1040	>500nJ	<400	0.5-1MHz	0.5	Ytterbium	High Q
Oscillator-Cavity dumped	800	30nJ	<15	1kHz-4MHz			Kmlabs

Table 2-1 Table showing the market survey of femtosecond sources and basic properties

Femtosecond pulses are considered ultrashort and as table 1 shows they range greatly in practical terms. There are effectively two or three classifications of pulse duration. There are the extremely short pulsed lasers, with pulses typically in the 10s of femtosecond duration which are most commonly, although not exclusively, oscillator lasers. The next region is about 100-350 fs that are often amplifier lasers. The final group is from 350-800 fs and is largely occupied by fibre and amplifier lasers. The pulse duration makes a significant difference to the pulse-material interaction and the pulse energy required.

Repetition rates of commercially available systems range greatly from single kHz through to 100MHz. The range leads to a significant difference in the applications of each. There is some evidence to suggest that better quality waveguides, for instance, are written with lasers operating in the MHz regime rather than kHz [**68**]. On the contrary often for micro-machining ablation lower repetition rates in the 1-300 kHz range tend to be chosen because they have higher pulse energies which are above the ablation threshold. For these lower repetition rate systems there is also less thermal loading due to the pulse train spacing. Repetition rates and the resultant thermal loading, or absence, offers clear advantages of one repetition rate over another for a specific task.

In conclusion the parameters of a chosen laser will strongly influence the effectiveness of work in particular area. The parameter windows are relatively small for high quality results in any given application.

2.1.2 Techniques employed

There are several different techniques employed when making micro-machined devices through inscription and ablation. Some of them are techniques applied to both regimes and others are applied more specifically to one or the other. Typically using a laser to perform micro-machining involves complex physical processes and is dependent on fine parameters of the material and laser. Theoretical models exist and are touched upon in other sections of this chapter, however, they are often considered to be only a guideline and require refinement for optimal processing when using a

practical system. In this section some of the basic methods and techniques applied to micro-machining are explained.

2.1.3 The basic system

Systems tend to either operate by having the sample fixed and the laser beam moving or by fixing the sample to a moving stage, or set thereof, and having a fixed objective lens, Figure 2-1. There is also the option to use galvanometric systems where the beam is manipulated using mirror(s) and obviously a combination of all three. Each of the layouts has its own pros and cons depending on the main purpose of use, for instance when the desired sample is small and is required to be machined quickly then galvanometric systems can be most advantageous, however, when operating over a larger area these systems suffer from spherical plane effects and correcting for these often leads to a loss of sharpness in the focusing. This is especially important for femtosecond work where the depth of focus, due to the nonlinear nature, is so small.

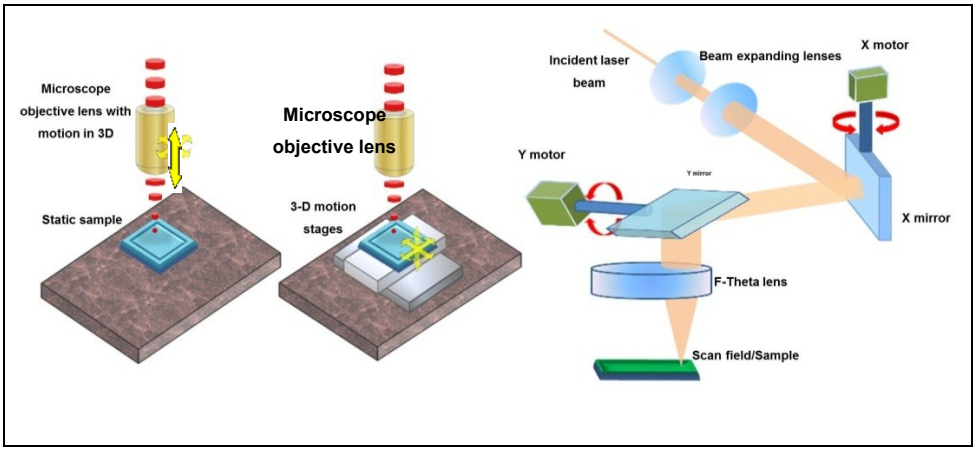

Figure 2-1 A schematic of three types of focusing arrangement from left to right a static sample with moving objective, a moving stage with static

objective lens and a galvanometric set up with motion controlled by mirror angle.

Often the most practical systems use a partially fixed objective, where the objective is also on a stage but often remains stationary when working at a given depth in the sample, and use mechanical or air bearing stages to move the sample. These are often programmed by computer linked drive control units. The majority of stages operate some version of CNC (Computer Numerical Control) system [**85**] each of which have their own protocols, however, the techniques used are applicable to most if not all systems of this sort.

2.1.4 Common terminology & basic techniques

There are a number of terms applied to certain types of machining that describe the fundamental technique applied to working on a work piece and these are defined in Table 2-2. The first of which we will consider is percussion drilling. This is a process of firing a number of pulses on a given area, each pulse removing a very small volume of material, thus leading to the creation of a hole. Typical laser repetition rates over 1kHz allow removal rates to be viable for use. This technique is used for the creation of small holes through or in materials. In general the material removal rates are relatively constant for small depths (to ~100 μm) after which the removal rate operates as the square root of the depth. Thus the time taken to double the depth is typically in excess of four times that of the initial hole. This occurs because as the beam penetrates to the bottom of a hole energy is lost to the material and the nature of Gaussian beam paths, after focusing, means that the energy available at the bottom decreases as the

wing that is clipped is inversely proportional to the aspect ratio increase. Typically helical trepanning produces some of the smoothest side walls and most uniform holes but takes longer and tends to be best applied to smaller artefacts.

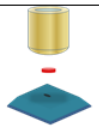	**Single shot drilling** - The process of using a single laser pulse to drill, this is rarely used.
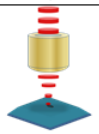	**Percussion drilling** - The use of a number of laser pulses at a repetition rate spacing above that of the length of the pulse used to remove material. Can lead to surface spatter which can lead to micro-cracking, deformation of hole shape and achieving high aspect ratios is often difficult.
	**Trepanning** - This is essentially percussion drilling with circular motion, often a pilot hole is drilled and then a spiral motion followed by circular finishing. The technique suffers from the same drawbacks as percussion drilling. The hole size formed by this motion is, to within the radius of the plasma, the diameter of motion. The holes produced by trepanning are generally more circular and accurate than a percussion drilled hole, however, they are larger in size.
	**Helical drilling** - The process of quantizing the ablation steps reaching breakthrough only after a number of passes described by a spiral motion. This often has a more circular geometry than trepanning and also minimises the load placed on the opposite face to that of the focus. It tends to also give less recast, however, takes significantly longer to process.
	**Cutting** - Cutting through a sample using a series of pulses through motion of the beam or sample, often multiple passes are required. **Etching / Milling** - Removing a defined depth of material through control of pulse energy and/or number of pulses per location.
	**Rastering** - The motion of moving back and forth over an area with lines separated by a given pitch. By varying the pitch this can lead to the removal of material from an area or in trenches. Typically these form square wave patterns although other forms are also used.

Table 2-2 A Table of the common techniques often used in hole drilling, surface texturing and micromachining with a brief description of their mechanism.

The choice of technique is largely determined by constraints such as process time, objective availability, precision, finish and artefact dimension and target aspect ratio. If dimensions smaller than a few microns are

required typically one would not use trepanning or helical drilling but would use a percussion or pseudo single shot regime. If, however, a large microfluidic chip were required or a smooth finish to the side of a hole of sufficient diameter were required a trepanning operation combined with stage movements would be employed. This is useful for channels or holes of approximately >10 microns depending on the specific objective used. Typically, unless operating at extremely high speeds, the precision of the technique is not the limiting factor, often being negated by careful tuning of parameters like speed of motion and vector contouring profiles. Each application requires careful consideration of the relative merits of each and their suitability.

2.1.5 Other considerations

There are a number of other parameters and components to be aware of that can be critical to the finish and quality of a desired object. It is important to consider the desired aspect ratio or etch depth, the NA and working distance of the lens, the position of the focus in the sample, the beam polarisation, the speed of the moving parts and an inspection mechanism.

The aspect ratio is defined by the ratio of depth to width of an artefact, for example, a microfluidic channel or hole through a ceramic. The etch depth is the effective write depth of an inscribed feature such as a waveguide or diffractive element inside the bulk of the material. To optimise both of these parameters the choice of lens, power and beam shaping are fundamental. If aiming to write a deep slot into a substrate one would

typically choose a lens with a low NA and long working distance so that it could operate at a distance and over a range of positions without being coated with the debris created by the plasma and avoiding contact with the material. Ideally most of the work should be done with a static z component and the right choice of lens, however, there are times when stepping the lens towards the sample is necessary to achieve a specific depth or profile. The position of the focus required to ablate a slot, when scanning, is typically not at the midpoint of the desired slot depth. Through empirical experience it comes out at typically 1/3 of the depth but the exact position will change depending on the sample and other parameters. The exact theoretical understanding of why this is the case is not fully understood, but was outside the remit of this thesis. There are also issues to do with shielding by the walls when looking to achieve high aspect ratio side walls. This is because the pulses wings are clipped reducing the power of the pulse.

The speed of any scanned motion, as with repetition rate, will affect the rate of removal of material. This is because the integrated fluence will be varied by the change in the speed of motion as the number of pulses per unit volume will be less. A variation in the repetition rate would have the converse effect. That is to say that if the pulse rate increases by a factor of 2 that the removal rate would increase linearly, assuming constant pulse energy. Whereas a doubling of the speed would half the removal rate or create a series of dots rather than a line.

There are two types of polarisation that can be used, linear and circular polarisation. The polarisation is believed to affect the write quality of inscribed lines such as waveguides. The current thinking is that a polarisation orthogonal to the direction of write for straight waveguides, or circular for curved ones, is preferable and results in smoother tracks [**45**]. Polarisation parallel to the direction of write is not favourable since it produces less smooth tracks. There are other techniques employed such as combining cylindrical lenses with the regular microscope objectives to refine the width of written lines.

The ability to fully inspect and align a sample pre- and post-inscription or ablation is of fundamental advantage to any system. The use of confocal systems and inspection methods to inspect during writing has also developed considerably in recent years [**86**]. A standalone camera can also be used to monitor the sample. The exact design and components used will not be uniform across all systems but the importance and advantage gained by their inclusion are extremely significant to the complexity of the fabricated devices.

2.1.6 *Post Processing*

There are a few post processing techniques that are important in relation to femtosecond micromachining. The most common technique is to wet etch using either hydrofluoric acid (commonly abbreviated to HF and is hydrogen fluoride in water solution) or ammonium bifluoride (ABF is chemically NH_4HF_2 and a diluted version of HF in a salt form, although used in water solution). The whole process involves inscribing the material

(below the ablation threshold) using the laser focal spot then placing the substrate in the acid. The acid preferentially etches the inscribed areas at a rate of 50:1 in fused silica [**87**] and as such removes the inscribed area selectively. This technique offers the ability to make smoother structures in transparent materials with smaller features and higher aspect ratios. It is also possible to fabricate subsurface channels that would otherwise take a sequence of layer deposition stages or lithographic techniques. There is a downside, in that the use of these chemicals adds additional processes and time over direct ablation and involves the handling of hazardous chemicals. Figure 2-2 shows work done in optical fibre. The fibre has been exposed by femtosecond laser inscription below the damage threshold then wet etched using HF producing very narrow, high aspect ratio channels through the fibre core.

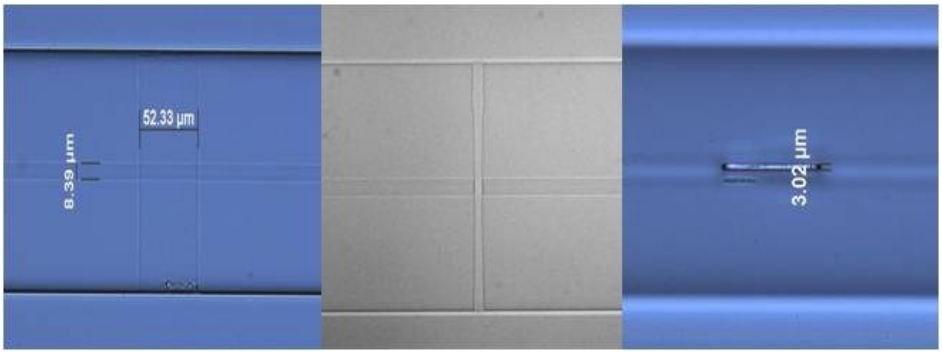

Figure 2-2 Micro-channels fabricated in standard fibre using fs inscription and chemical etching [88]. Device made with Dr Yicheng Lai, Dr Kaiming Zhou and I.

The use of heat treatment, cycled and constant, may be important for femtosecond micromachined structures. In theory, the thermally induced

stresses created by the shockwaves propagating in the material around the plasma can be thermally annealed out through heating the substrates post inscription. Heat treatment thermally relaxes the material such that the stress is released and the permanent change of the inscription is all that is left. This effect is still the subject of study and its ability to offer further understanding of the plasma-material interaction will most likely be of fundamental impact [**89**].

2.2 Lasers used

There were three systems used for the work completed in this thesis. The primary system has been titled Aston micromachining with other work having been carried out on another femtosecond laser system at Aston nominated as the Low rep system and finally some work was carried out in the Nanophotonics Research Laboratory at the Cyprus University of Technology. For ease the systems have been detailed individually as a reference for future system parameters in the text. Unless stated otherwise the system used was the Micromachining Lab at Aston University. Table 2-3 shows the lasers used at each of the three systems and the key laser parameters.

Laser	Amplitude s-Pulse HP	Coherent Tsunami-Spitfire	HighQ Laser Femtoregen IC 355
Pulse duration	450 fs	80fs	350 fs
Pulse energy	1.1 mJ @ 1kHz	0.75mJ	20 µJ @ 100 kHz
Average power	1.1 W		2 W

Repetition rate	1-100 kHz	1 kHz	Single pulse - 100 kHz (TTL-Trigger)
wavelength	1030 nm	800 nm	1035 +/- 5 nm
Beam quality	TEM	TEM_{00}; $M^2 \leq 1.5$	TEM_{00}; $M^2 \leq 1.25$
Laser Material	Ytterbium	Ti: Sapphire	Ytterbium
Laser Type	SSDP	Regen-Amplifier	SSDP

Table 2-3 A table showing the key parameters of the three lasers used in the course of study

2.2.1 Aston University micromachining laser

This consists of an Oxford Lasers J-series system containing an Amplitude Systemes s-Pulse HP femtosecond laser. The laser specifications show a high peak power ideally suited to ablation work in a range of materials. Through the beam delivery optics the system also allowed inscription regimes to be accessed post attenuation. Figure 2-3 shows the basic layout of the system before reaching the vertical stages and microscope objective. The enclosure contains the laser and the main beam delivery elements of the system such as safety shutter, dielectric turning mirrors, beam expanders, optical attenuator and trepanning head and polarisation optics.

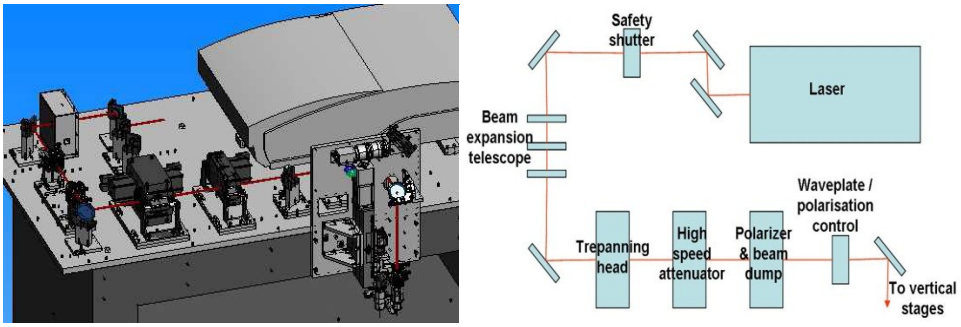

Figure 2-3 Schematics of the system layout showing key beam delivery optical arrangement. Image on the left from Oxford Lasers.

The dielectric turning mirrors are specially coated for broadband near infrared laser operation and are set for 45 degree angle of incidence. The mirror diameters are 25 or 50mm.

The beam expander, located before the trepanning head in the beam path, was used to vary the size of the laser beam prior to entering the machining objective lens. Through its use beam divergence and the risk of damaging the attenuation and trepan optics was controllably reduced. The final focal spot size was able to be manipulated through adaptation of this via a 2x or 4x beam expansion achieved using a pair of plano-concave and plano-convex singlets with focal lengths of (i) –50mm and +100mm or (ii) –50mm and +200mm respectively. Both singlet lenses are mounted on four axis mounts for ease of adjustment.

Laser attenuation was operated via a half waveplate and thin film polariser pair. The waveplate is mounted on a motorised rotary stage for CNC control of incident laser power. A quarter waveplate located immediately after the laser attenuator provides circular polarisation of the laser beam. The polarisation was also able to be controlled via a CNC mounted polariser; however, this was rarely used outside of initial trials.

The focussing optics assembly mounted on the z-axis was fitted with different machining lenses depending on the study. There were four lenses used in total. Two air-spaced triplet lenses of focal length f=+66mm and +33mm which were broadband coated for 670-1064nm and consist of a

laser aplanat doublet and aplanatic meniscus combination to minimise spherical aberration. The remaining two lenses were high magnification Mitutoyo objectives MPlan APO NIR 100x of focal length f=+2mm, NA=0.50 and an Mplan Apo 20x of focal length f=20 mm with an NA=0.42. At this point the beam is focused vertically downwards towards the work piece mounted on one of a series of jigs which in turn are mounted on Aerotech 1000 high precision air-bearing stages. The two jig mounts used were a vacuum mount jig and a generic clamping mount. Typically the clamping mount was used the clamping one as this gave the most reliable stable work piece under sometimes rapid stage movements. There were also occasions where the sample was affixed directly to the jig mount if the working area was larger than the clamping holes allowed. The stages were also set to be able to mount two fibre clamps (Elliot Martok) with a small mechanical distance and direct separation of 20cm. These were used to mount optical fibre for micromachining and grating inscription.

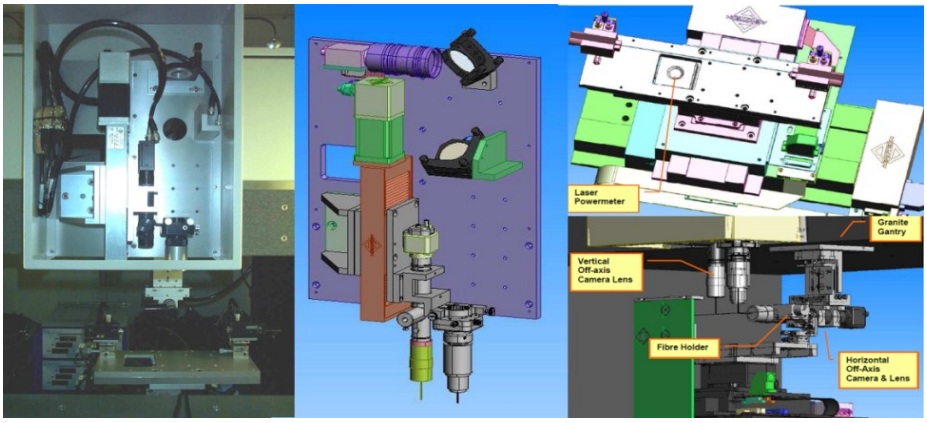

Figure 2-4 Shows the vertical stage beam delivery and Aerotech stage arrangement for the micromachining laser system. CAD images courtesy of Oxford Lasers.

2.2.2 Aston University Ti: Sapphire Low repetition rate system

The low repetition rate femtosecond system is based around a Ti: Sapphire mode locked regenerative amplifier laser. The laser is a Spectra Physics Tsunami oscillator and Spitfire amplifier set up. The system generates femtosecond pulses at 1 kHz at 800nm with typical pulse widths of 100fs with pulse energies around 0.75mJ. The system was adapted to have attenuation control using a polarizer on a rotation stage controlled by Labview software. The motion of the stages was controlled by the same Labview software. The stages used were Aerotech 1000. The system was designed for grating writing and there was a rotation stage on top of the x-y stages. This was used to position the fibre angle relative to the fixed objective. The fibre was clamped at both ends with a coverslip arrangement where the fibre is oil immersed. This counteracts the curvature of the fibre and the distortion of the curved surface that the incident light encounters. This set up is shown below in Figure 2-5. This system was used for some of the work carried out in the initial sections of chapter 5.

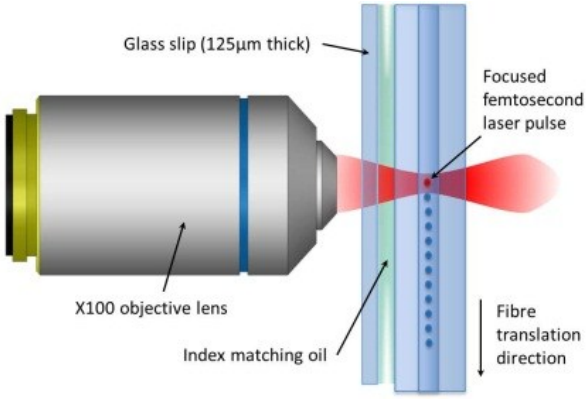

Figure 2-5 A schematic showing how a microscope cover slide and refractive index matching gel are used to negate the curvature of the optical fibre when inscribing.

2.2.3 *Cyprus Nanophotonics Research Laboratory Laser*

During the course of studies a significant amount of time was spent working at the nanophotonic lab at the Higher Technical Institute, Nicosia, Cyprus. The work was carried out in conjunction with co-supervisor Dr K. Kalli and was largely focused on ablation with some later work on inscription.

This system is based around a femtosecond laser system (HighQ Laser Femtoregen IC 355) emitting 300fs pulses at 1035 nm and operating at a repetition rates of between 1-100 kHz. The system was set up again using Aerotech stages and attenuation control based upon the software control that came with the laser system. Figure 2-6 below shows a schematic of the layout used for beam delivery.

The initial work was based upon setting up an optical path and machining objective set up to be able to work in both planar and fibre. The figure below shows the set up largely used during work carried out in this laboratory. The top down method was employed as this is able to be versatile and machine areas and volumes, using manual controls added to the setup, that the main lab could not achieve. The set up was then added to by two goniometers that allowed planar samples to be laid perpendicular to the direction of write. This is important as samples that were to be characterised both in ablation and inscription needed the parameters to be kept as close as possible to uniform.

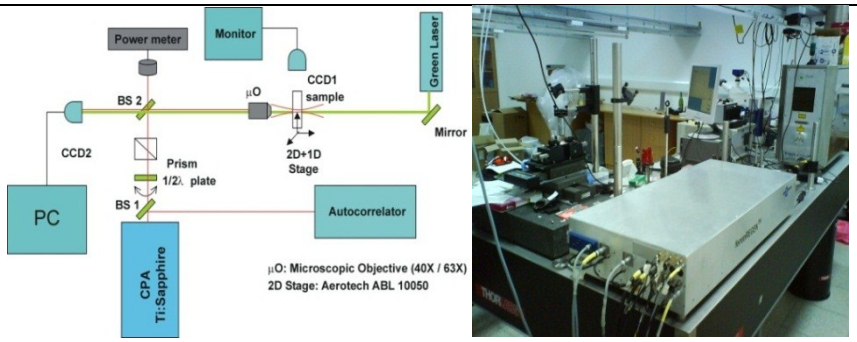

Figure 2-6 Schematic of beam path and photograph of the nanophotonic lab at HTI, Cyprus.

The method for finding the focal position with respect to the sample was based upon the creation of fluorescence that was observed when a white sticker was placed underneath the sample. This fluorescence changed in both colour and shape with relative depth. This allowed us to repeatedly position the z-position of the objective relative to the sample surface to within a very small variation, typically around 1 μm.

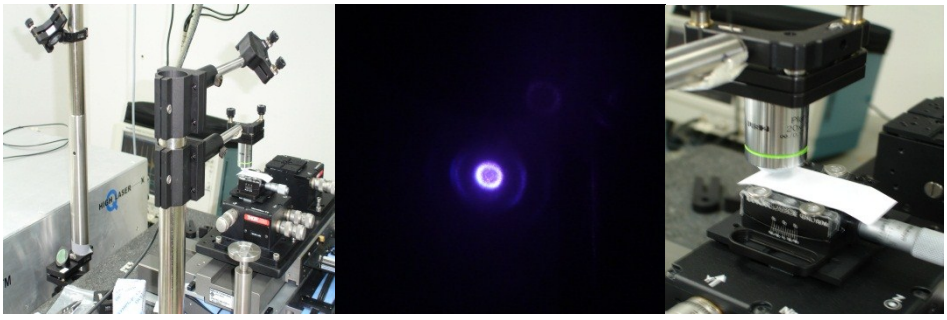

Figure 2-7 Showing the focal arrangement, plasma and fluorescence and positioning of the objective relative to the mount with goniometer.

Later work utilised the initiation of 2nd and 3rd Harmonic generation by the interaction of the pulse and focal plasma. This, in a similar way, created green and indigo/blue circles which characterised the depth of inscription.

The use of this technique and the surface fluorescence detection allows most samples to be adjusted to avoid tilt to within two or three microns using a three corner point focus finding technique. The possibility of using 3D defects to position a sample was not needed in the work carried out here as single step processes were generally preferred. As a means of testing a focus value a range of lines and spots can be written at the surface with small variation in z, this allows a visual test of the finest and cleanest spots/lines to confirm focus height. This does result in surface deformation and is avoided where possible.

2.3 CNC stage control

A critical area of femtosecond micromachining and inscription is the precision translation required for the direct write technique to be applied to any given substrate. Several variations have been used to create simple straight lines from masses on compressed springs to air bearing computer numerically controlled (CNC) stages. All of the three systems used in this work used the Aerotech A3200 control racks and air bearing stages. These are controlled by a series of commands that control position, velocity, acceleration and a number of other vital control mechanisms required for laser direct write processing.

The vast majority of the code used in this thesis was created by hand and used basic programming techniques, such as loops and IF commands, to create more complex shapes. Most code was programmed in relative mode with absolute commands being used for movements at a fundamental

level. This is compiled and fed into the rack which in turn creates high precision and accuracy movements on the air bearing stages.

The stage control through the combination of precise programming and sample mounting with fundamental understanding of the laser pulse-material interaction become critical to the success of a micromachined device.

2.4 Computer Aided Design packages

In this thesis the use of Computer Aided Design (CAD) modelling and design were applied to a range of micromachining tasks and a brief overview follows.

2.4.1 Computer Aided Design (CAD) & rapid prototyping

There are a number of applications of femtosecond micro-machining where the complexity and rapid prototyping required are less suited to programming the motion line by line. This is clearly shown in the complexity of the microfluidic device illustrated by Figure 2-8 below.

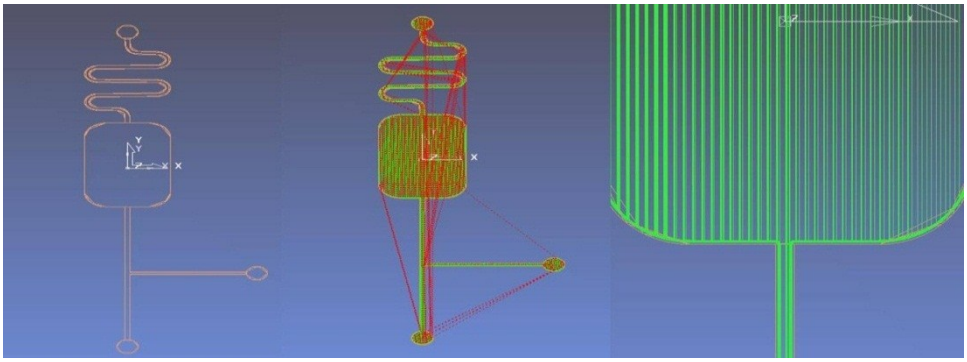

Figure 2-8 Computer Aided design images, from left to right 1) An plan view of a computer designed microfluidic device, 2) the machine path lines shown for work piece with green representing the path of the laser ablation

and red being the skimming non ablation transit, 3) a close up of the tool path for ablation showing rastering and a finishing edge pass.

To code this line by line would be extremely time consuming and to change something like the machining pitch could take considerable effort going through the code line by line. In these situations the use of CAD software packages can be a significant advantage in being able to vary the parameters (such as pitch, write speed and scaling) quickly and design complex structures that would otherwise take significantly longer. Although it is not impossible to code some of the more complex structures the plausibility and economy of doing so when the software packages are available becomes more weighted in favour of the automated approach [39].

2.4.2 CAD package used (Delcam, Solidworks and SolidCam)

For the work carried out in this thesis using more complex shapes than can easily be coded the combination of the CAD package offered by Solidworks and the CAD to machine code software offered in Delcams' Powermill software or the add on to Solidworks, SolidCam. The model would be created in the Solidworks framework and then, if using Delcam, converted to an .IGES or .vda format. This when imported into the Powermill software was converted to machine code based on user inputs for parameters such as speed, pitch and style and angle(s) of raster scanning. The parameter file for this was customised to the system and optimised to perform the motions in the general case optimal conditions. Often the code outputted would be optimised further to suit the particular application. In the case of the spiral blood pump the style of spline created was not able to

be converted to a format capable of being processed limited by the file formats licensed with the Powermill software. This work was carried out using the add-on SolidCam. This package used enabled the beam path to be calculated in two separate spline sets that were subsequently stitched to create the final fluted curve. This is discussed further in section 3.7.

2.5 Beam delivery

The delivery of the laser beam to the sample of interest is of key importance to the quality of output achieved. The key topics of interest in the main system of use are discussed here.

2.5.1 Lenses

The work was largely carried out with 4 lenses. Two aspheric doublet micromachining compound lenses and two Mitutoyo long working distance near infra-red microscope objectives. The two machining lenses were of different working distances of 33 and 66mm. These lenses were used for work where either large areas needed to be removed or deep features have to be created. They were also required for trials of soft focusing techniques. These lenses, although not aberration corrected, were corrected to best-fit standards which were sufficient to achieve the features desired. The two Mitutoyo microscope lenses were of 50x and 100x magnification with NA of 0.42 and 0.50 respectively. The M Plan Apo NIR series lenses are designed to operate between 480-1800nm which well suited the 1030nm incident laser light. The choice of high NA lenses with long working distances allows the writing technique to include inscription and machining within samples. The high NA avoids self-focusing within a

substrate at most power ranges and the long working distance allows for what is termed transverse focusing allowing greater flexibility in write design. These lenses were largely used for inscription, however, some of the work in fibre was carried out with them as they allowed for smaller focal spots and more controlled machining with complex substrate geometry.

2.5.2 Telescoping

Telescoping was used for two practical purposes. The beam when exiting the laser had a width of approximately 3mm where the entrance pupils of the objective lenses were often larger. Thus, to achieve fully diffraction limited focusing the beams would have to be expanded to fill the entrance pupil. Although this was done occasionally it was found that for most of the work this was not necessary and was as such was often set to an intermediate position that suited a range of lenses. The telescoping also enabled the trepanning heads, discussed below, to work on a more consistent basis with reduced reliance on an ultra-fine beam pointing stability over the duration of writing.

2.5.3 Trepanning

Trepanning is essentially percussion drilling with circular motion, often a pilot hole is drilled and then a spiral motion followed by circular finishing. The technique suffers from the same drawbacks as percussion drilling. The hole size formed by this motion is, to within the radius of the plasma, the diameter of motion. The holes produced by trepanning are generally more circular and accurate than a percussion drilled hole; however, they are larger in size. In this system this was created by controlling two prisms

mounted in two continuous motion Aerotech rotation stages. As the light passes through one prism it is refracted slightly from the original path. When this light then is incident on the second prism depending on the relative prism positions the beam is returned to a parallel but offset beam path. By carefully controlling the relative motion a circular or helical beam path can be created at focus. This radius can be actively controlled and is used to create better holes in micromachining. It is commonly preferred to the use stages to do this as it is not only quicker but often yields higher tolerance artefacts as compared to high speed small rotation stage movements where the stages are often optimised for other larger processes.

Helical drilling is the process of quantizing the ablation steps reaching breakthrough only after a number of passes described by a spiral motion. This often has a more circular geometry than trepanning and also minimises the load placed on the opposite face to that of the focus. It tends to also give less recast, however, takes significantly longer to process.

2.6 Materials processed

Although the focus of the work presented here has used Borosilicate and Fused silica or corning smf-28 a range of other materials have been processed during the study including; stainless steel, GaAs, PMMA, polyamide tubes, CVD diamond, Sapphire, Shapal and Macor. A few examples of some of these are briefly shown below.

2.6.1.1 CVD diamond-creating carbonitic wires

There are a number of groups studying the potential uses for femtosecond lasers to manipulate the properties of diamond including making waveguide structures. The initial work carried out here was with the intention of creating carbonitic wires on or near the surface of the CVD diamond samples. After comprehensive cleaning by Shi Su, of Aston University, the samples were mounted in the Micromachining system at Aston University. At this point I aligned and wrote a series of test samples at low inscription energies using a 100x Mitutoyo lens. Through varying the pulse energies between 390-1100nJ and inscribing a rastering structure of 100x100µm at a pitch of 10µm the samples were inscribed. Through exposure the diamond bonds break forming carbon like wire structures. These were then examined using SEM by Shi Su and Andrew Abbott at Aston University. Some of the results are shown below in Figure 2-9.

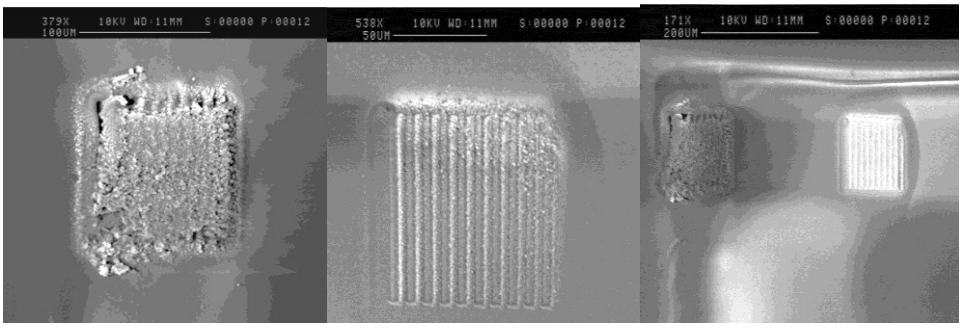

Figure 2-9 SEM magnified images of the diamond surface after the 1100nJ, 950nJ inscription and a lower magnification SEM image of both. SEM taken by Shi Su and Andrew Abbot.

The figures were analysed in collaboration with Shi Su. The figure shows SEM images of the area after inscription at the surface of the substrate. The diamond surface seems to have been 'graphitized' from the SEM photo. The second image shows the diamond surface machined where the grooves become obvious and there are no over-burn graphitized areas detected. This is shown more clearly in Figure 2-10 below where the exposed and unexposed regions can clearly be seen. This shows that the effective write diameter was approximately 5μm. The result is a graphitic channel that was sufficient for initial resistive measurements could be made and characterised for device design.

It should be noted that during the inscription only a few of the regions were on the surface of the sample. This was because extreme difficulty was experienced in achieving sample flatness acceptable using the 2x2mm samples provided. This was mainly down to two aspects, the lack of a goniometer that did not hamper the vision system and a frosted back

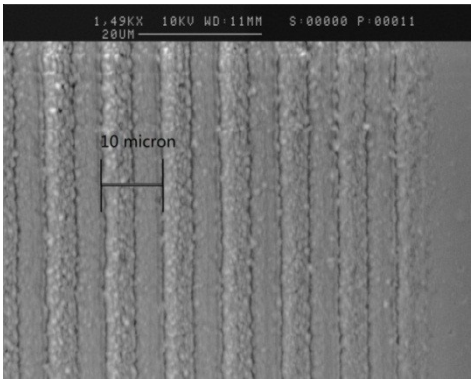

Figure 2-10 High magnification of 950nJ power level laser machining area showing the grooves structure of the exposed and unexposed regions.

Writing parameters; λ=1030nm, τ_p=450fs, x100 Mitutoyo lens, υ=10 mms^{-1}. SEM taken by Shi Su and Andrew Abbot.

surface of the substrate. These were not fully overcome in the initial trial conducted here and as such tilt most likely played a significant factor in the depth of the inscription. Whilst this is not as significant in most transparent materials with indices of around 1.5 the index of diamond is 2.49 and thus aberrations occur that would deform the focal region significantly. To continue further with this work adaptive correction for these would be required using spatial light modulators or similar. Further work will need to tackle the alignment and beam deformation in order to conduct thorough parameter testing. The application of direct write inscription in diamond to this particular problem was felt to be limited and as such this work was not continued in the remit of this thesis.

2.6.1.2 Stainless steel

A common material used in laser micromachining is stainless steel. In a trial where slots were machined with different bridge separations between them the results show clean exit slots but rounded entrance ones. This was caused by having the focus too deep and not using a sacrificial layer to negate this effect. A common technique would be to use a thin layer of copper or similar metal and then post process removal the layer to leave clean entrance slots. The wall structures created were able to be extremely thin, a few micron wide, with several hundred microns of depth. Once again the level of kurf and melting or recast is minimal if non-existent as shown in the SEM images in Figure 2-11 below.

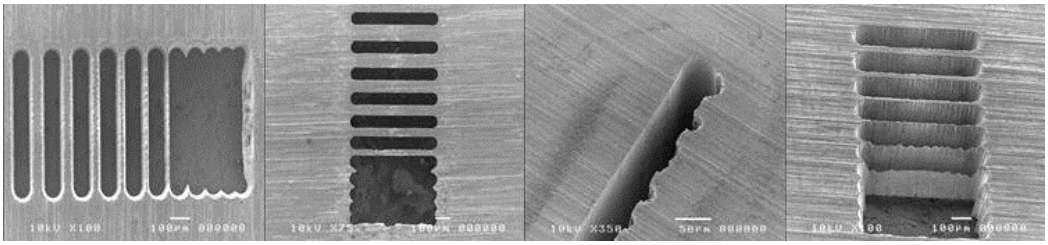

Figure 2-11 SEM images of the slot Entrance, Exit, parameter test and angled image showing the thin bridges left from left to right respectively. SEM taken by Oxford Lasers.

2.6.1.3 Ceramics

Ceramics are of key interest to a number of industries including print and engine manufacturers where the holes created are used to control precisely the jet flow created to improve efficiency of combustion of print quality. To this end the ceramics of Macor and Shapal are of prime current interest. Prior testing with ns lasers do not yield good results in these ceramics often not even being able to process them to a good hole quality if a machined hole can be created at all.

2.6.1.3.1 Macor

A sample of Macor was tested and a range of hole sizes drilled using trepanning and spiral trepanning. A number of the holes seen in Figure 2-12 below are near straight edged, to within a few 10s of microns from top to bottom, and clear through the 1.5mm thick sample with hole dimensions down to 10s-100s of μm. There are no signs of blackened edges or damage that are common with other laser ablation techniques in this material and

high repeatability is shown on the two series of 6 holes to the right of the image.

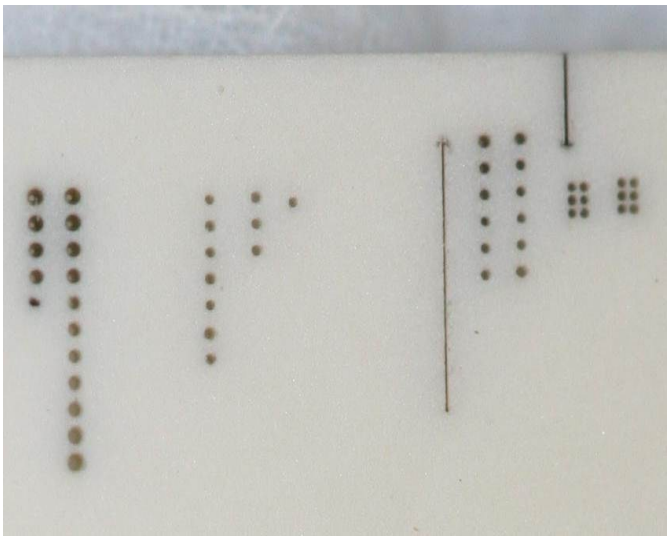

Figure 2-12 Macor test sample showing a range of holes drilled through the ceramic using femtosecond micromachining. The sample here shows holes ranging from 10s-100s of microns in diameter.

2.6.1.3.2 Shapal

Sheets of 0.5mm thick Shapal were machined in a series of holes again to examine the results and quality. Although the exit holes show deformation of shape, most likely due to the focal height being a little too high in the sample, the results show good quality entrance holes and no damage or kurf at either entrance of exit holes.

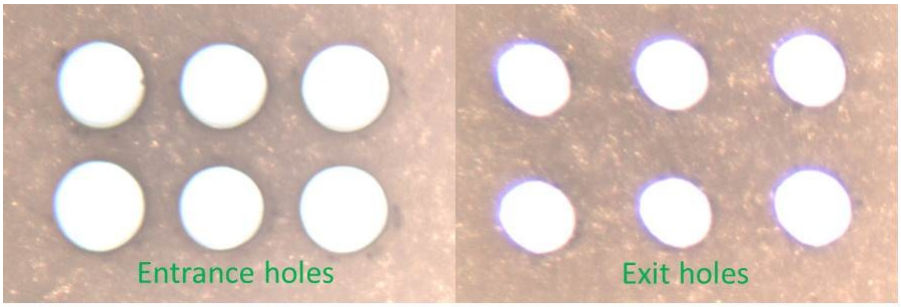

Figure 2-13 Shapal test sample showing consistent holes drilled through the ceramic using femtosecond micromachining. Images taken by Oxford Lasers. The holes here are of the order of 100 microns in diameter.

2.6.1.4 Polymers

There were three main areas of work in polymers. The exploration of creating fibre Bragg gratings in polymer optical fibres, selective layer ablation of multiple layer polymers carried out at high speed for laser cutting of OLEDs (in collaboration with Oxford Lasers) and creating leak tests in polyamide tubing. The majority of these trials were carried out using the Aston University micromachining laser system. It was operated at low repetition rates, to avoid as much unwanted thermal load as possible, and at 1030nm. Unfortunately this not ideal laser wavelength was the only one with suitable focusing objectives so lower two photon wavelengths were not able to be utilised. Having said this, there were a number of positive results. Figure 2-14 shows an entrance hole in polyamide tube used for drug delivery and some initial samples of multiple layered polymers where the selective removal of a single polymer layer was examined.

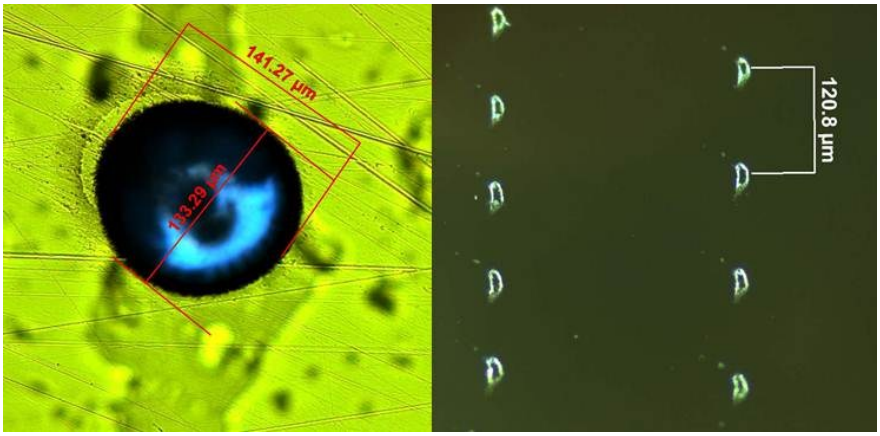

Figure 2-14 Polyamide tube with hole through only one arm and machined OLED like multi-layer polymer aiming for selective removal of a single polymer layer.

The polyamide tube result enabled a hole to be produced through only one arm of the tube with no adverse effect on the inside of the tube opposite. This had not been achieved using previous techniques and although further work would be required to optimise the hole shape, to make it more uniform, through using a pilot hole and spiral trepanning the required flow rate was achieved. The trials with the OLED like multi-layered polymer was found to slightly damage the second polymer layer, however, through optimisation of the pulse energy and focus height this should be correctable.

Point by point inscription of fibre Bragg gratings has yet to be fully achieved and in collaboration with Ian Johnson and Dr Kyriacos Kalli several attempts in a range of polymer optical fibres and planar substrates were attempted. As with other groups around the world no definitive

grating response has been recorded in spite of promising microscope images like those shown in Figure 2-15below.

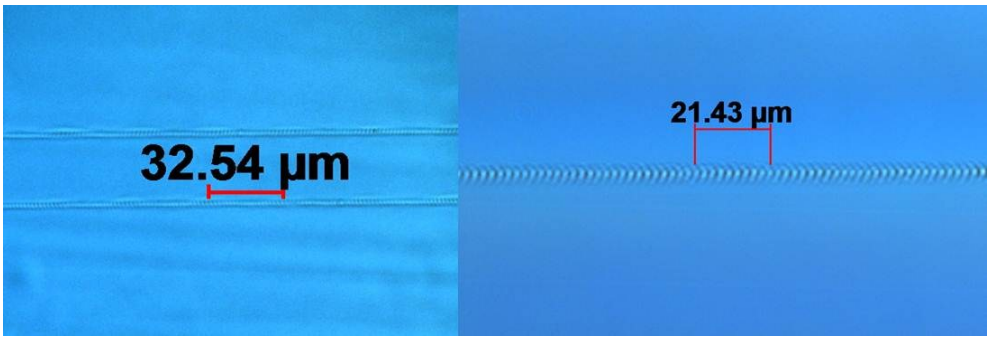

Figure 2-15 Showing inscription in planar PMMA and Cytop fibre

There are three critical limiting factors that were found during these studies. First the consistency of polymer samples is very variable especially when dopants have been used to induce index change to give core guiding. This variability combined with the non-linear excitation mechanisms for a wavelength of 1030nm gives very fine limits around the index modification and damage thresholds of the various polymers. This means that the process is extremely hard to repeat with any significant certainty from sample to sample. The second issue is that the lasers used have both the wrong wavelength, as touched upon above, and too much power. The fine control of attenuation at the lowest powers was found to be critical and yet hard to achieve. To do this with more precision a higher extinction ratio polarising attenuator set up would be required to those available during experimentation. The third is that most polymers have attenuation losses that increase significantly outside of the visible. Thus to characterise a grating with the disadvantage of significant losses experienced for 1550nm transmission becomes hard to measure a significant grating response.

2.7 Substrate preparation

Samples were prepared using alcohols to clean the substrates fully. This was found to be critical to avoid dust or particulate obstructing the beam and at times not allowing it to create ablation or inscription. The substrates would also be polished to be optically flat and parallel to each other. This was crucial for the ablation on the surface where etch depth was critical as any sample misalignment was extremely detrimental to the work as the focal spot is so tight that a misalignment of 1 micron can lead to a sample not being ablated or an etch depth change which can be critical for certain pieces of work.

2.8 Characterisation methods

A range of optical and physical methods were used to characterise the micromachined and inscribed artefacts. These are outlined below.

2.8.1 Optical (i.e. transmission and reflection microscopes)

The vast majority of the work pieces demonstrated in this body of work were examined using a transmission microscope. The artefacts were evaluated using an Axioskop 2, Carl Zeiss, Germany using a range of microscope objective lenses. There were also other reflection scopes that were used for non-transparent characterisation which allowed characterisation of processed ceramics and metals.

2.8.2 Profiling

Various methods of optical profiling were undertaken including white light profiling. The nature of working with transparent materials often with a bottom micromachined surface roughness of approximately 10s-100s of

nm, if not greater, and with high aspect ratios left the use of most techniques challenging. The nature of the scattering from surface roughness, optically transmissive (as opposed reflective) properties of most glasses used at the wavelengths of inspection and the use of high NA lens, required for high resolution, clipping feature edges from high aspect ratios led the characterisation of artefacts using profiling techniques to be undertaken with great care. The techniques were trialled especially in the work on microfluidic bloodpumps demonstrated in chapter 3 but also in characterising some of the shapes created in prior work and in characterising some of the phase mask inscription properties shown in chapter 4. The profiler used was a NT9100 profilometer from VEECO Wyko. The scans were carried out by Charalambos Koutsides at the Nanophotonics Research Laboratory in Cyprus and the data was personally analysed. The use of profilometry only became available towards the end of the work and as such a reliance on using polymer moulds and optical microscope proved to be the basis of artefact refinement.

2.8.3 Polymer moulds

With the use of profiling methods being challenging as described above with transparent material, thermally setting polymers were used to characterise the devices created. Through the use of Polydimethylsiloxane (PDMS) moulding compounds available from Dow Corning, *Sylgard*® 184 Silicone Elastomer, the thermally setting two part mixture forms moulds with minimal shrinkage. The compound was also chosen for the low viscosity and deep section cure. These allow for the compounds to cure in

high aspect ratio devices and give nanometre resolution replication of the original device within the deep recesses of the artefact. The methodology is taken from Prof. Robert White's methodology (see appendix A), note that the chemicals used were substituted for the Dow Corning compound Sylgard 184 otherwise the method was followed exactly. These moulds were used to provide easier scanning of the artefact and a more accessible way of characterising the bottom of the micromachined area.

2.9 Principle iteration process of artefact creation

The methodology used in the creation of the artefacts in this thesis took a singular general form. This iteration process was followed in all cases with varying numbers of process loops for each given application. The initial choice of lens, energy, speed of motion and other key parameters came from initial parameter testing and theoretical calculations of pulse overlap and material thresholds, spot sizes of lenses. The general process is set out in the flow chart in Figure 2-16. It is important to note that this process is rarely fully completed in the work presented in this thesis as room for development is found in many of the proof of principle applications presented in the following chapters. The final, or near final, solutions are presented with the understanding that the process was developed using this iterative method.

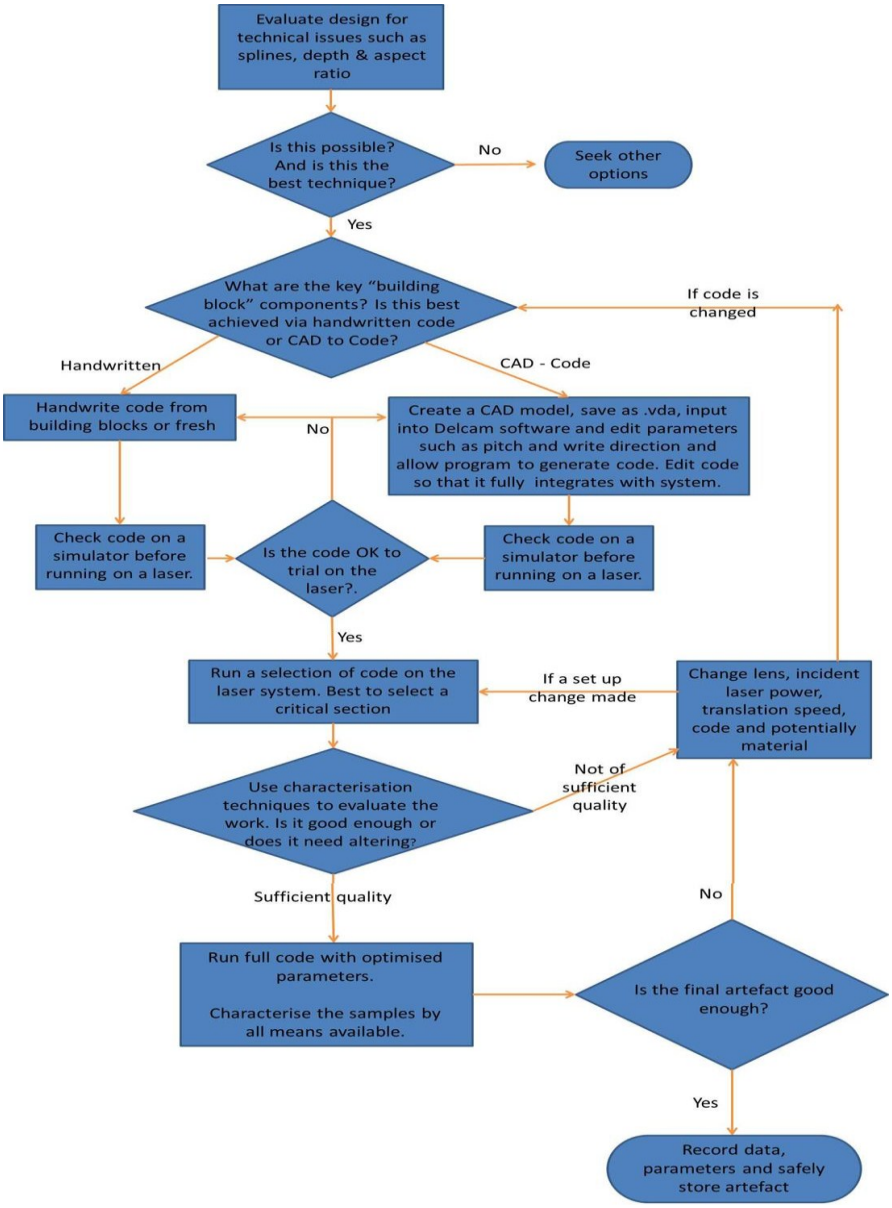

Figure 2-16 A Flow chart showing the iterative process steps involved in creating an artefact. The process may contain many loops and may never be fully complete depending on the application.

3 Planar Micromachining

The work presented in this chapter was designed by me with the exception of the microfluidic mixer which was undertaken with Oxford Lasers. The profiling scans were processed by Charalambos Koutsides with analysis carried out by me. The two projects in sections 3.6 and 3.7 are collaborative and the details of the workload are presented there.

3.1 Introduction motivation and techniques

The field of planar micromachining has a number of applications from the creation of holes and slots for purposes such as printing and filters for astronomy. Whilst a range of work was carried out in a number of materials as discussed in section 2.9, the focus of this chapter was the use of femtosecond micromachining in the field of optofluidics. This is the field devoted to the integration of microfluidics and optics. The body of this work was carried out in either fused silica or borosilicate with all of the bio-compatibility, mechanical and thermal properties and optical transparency these glasses possess as discussed in section 1.5. These devices are designed

to be integrated photonic or optoelectronic devices where fluids are optically characterised.

Femtosecond micromachining has opened up the ability to micromachine complex 3D structures; these structures are now typically able to be achieved without the need for multiple processing steps. Typically the devices that are desired are being made in glasses so that they can be optically interrogated and require high aspect ratio features. These features because of their use in optofluidics need smooth surfaces and high aspect ratio walls. This is so that the fluidic properties desired in microfluidics can be achieved and maintained in a lab on a chip device. A range of materials are used for these purposes including PMMA [**90**], Foturan [**91**], pure and doped borosilicate and fused silica [**92**,**93**,**94**,**95**]. As discussed earlier the advantages of borosilicate and fused silica make them ideal for study in these fields and hence the work in this chapter focuses on the use of these materials.

Most prior work has utilised photolithographic techniques adapted from the microelectronics industry. This entails fs exposure, annealing and HF etching [**96**,**87**,**92**], the process is time consuming, taking up at least 5 hours per chip [**96**], expensive and uses hazardous chemicals in a three step procedure. Another technique relies on the writing of the desired structure in a metal coated layer with subsequent exposure and etching [**97**]. Once again this leaves the prototyping, manufacturing and development cycles with long lead times and often the results that contain cracks and debris.

Both system and software development has led to the improvement in repeatability of pure ablation techniques and this paper aims to set out the potential of pure ablation for use in micromachining device prototyping and demonstrates that high aspect ratios are achievable with a fast one-step process. The quality of the results shows a step forward for pure ablation as a method of rapid prototyping and low volume manufacture.

The use of these chemicals was largely avoided in this thesis with the emphasis being on trying to reduce the use of HF or similar through using micromachining techniques as described in section 2.1.2. The following work describes the progress through initial trials in rapid prototyping and creation of high aspect ratio devices through the development of increased quality of surface finish and into practical devices including the creation of a transparent centrifugal blood pump test artefacts.

3.2 High aspect ratio paper and rapid prototyping

The laser used for this work was an Amplitude-Systemes s-Pulse HP fs laser that produces pulse widths of between 450-550fs, pulses at rep rates of 1-100 kHz at a wavelength of 1026nm and average powers of 550mW. The laser is incorporated into an Oxford Lasers machining system that consists of air bearing stages mounted on a granite bed for stability, optical power control and a vision system for high accuracy alignment. With applications such as these the system was driven by Delcam Powermill software which allows 3D CAD drawings to be inputted and translated directly into control code which drives the system.

The glass used was Standard BK7 microscope slides of 3mm thickness. The sample was mounted on a jig on a 3D stage with the beam delivered through a machining objective on a linear stage. The beam was focused by an air-spaced triplet lens of focal length 66mm an NA of 0.16 and a working distance of 45.4mm. The devices were designed using CAD software and imported into the Delcam software. The parameters for the pitch, scan depths, speeds of translation and approach, power and laser repetition rate were set after iterations as described in section 2.9. Both samples were written at 1 kHz rep rate, with pulse powers of 250nW and at typically 1mms^{-1} translation speeds.

Figure 3-1 shows a microfluidic device where channels of width 80µm were ablated using the Powermill software to control the system. This structure demonstrates 90° bends as well as curves, holes and well/mixing/separating areas. The pitch was set to give a demonstration of the aspect ratios achievable and the potential for a pure ablation approach.

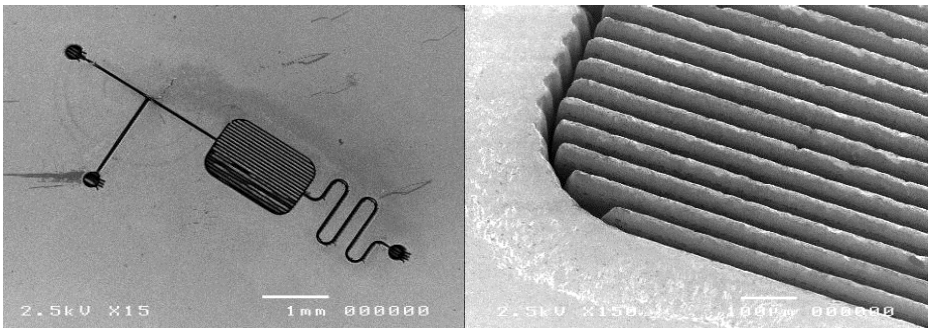

Figure 3-1: (a) SEM picture of the whole device (b) SEM of a device zoomed in on the fine (50µm pitch) ridges that were machined into the main fluid channel. SEM taken by Oxford Lasers.

A second device, being twice the size of the first sample, was fabricated to show the easy variation of parameters and the speed at which prototyping can be done. The holes are 600μm deep, the channels are ~290μm deep and 260μm wide. Both devices were written in under one hour from start to finish and no post fabrication cleaning has been carried out.

Figure 3-2 Microscope images of the second device showing (a) and (b) the steep sided channels and quality of the machined edges and (c) the quality of the machined bends

The first device was subsequently scanned using the white light profilometer by Charalambos Koutsides at the Cyprus Institute of Technology. The results are shown in Figure 3-3, Figure 3-4 & Figure 3-5.

Figure 3-3 shows the mixing channels clearly distinct to the remaining narrow columns. The lack of bottom surface information is due largely to the high aspect ratio of the channels. This makes it impossible to scan at high resolution over the entire depth and so it appears as a lack of information, i.e. black.

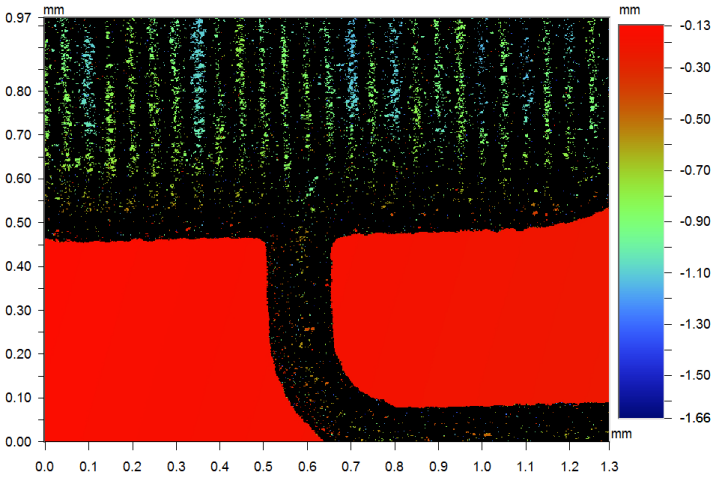

Figure 3-3 A 2D colour representation of the entrance from serpentine area to the milled mixing area. Image formed at x20 magnification. Profiling done by Charalambos Koutsides, processed by me.

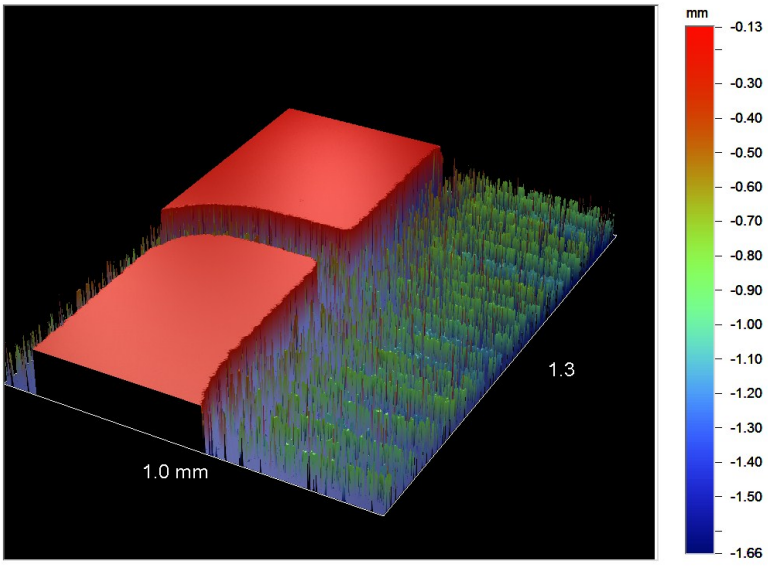

Figure 3-4 A 3D representation of the fluidic channel entrance to the mixing zone. It shows the high aspect ratio walls achieved and the mixing channels as thin columns. Profiling done by Charalambos Koutsides, processed by me.

The figure demonstrates the high aspect ratio achieved through the multiple scans undertaken at different heights and choice of objective. The edge roughness at the top of the unablated region (represented in red in figure 3-4) is also seen again. This would be removed by using an edge scan to finesse the corners.

The top of the mixing channels was magnified and re-scanned. The results of this are shown in figure 3-5. It shows the thin nature of the machined areas and the slight rounding of the top of the remaining high aspect ratio channels. This is due to the Gaussian nature of the beam forming a taper at the top surface when the lower depths are being machined. The removed area is shown to be around 10μm in width. As characterised through the use of optical microscopes and moulds the depth of these channels were found to be in the order of mm, leading to very high aspect ratio channels. This means that the slight taper seen here at the very top of the remaining material channels is largely insignificant as liquids would be highly unlikely to come close to this height within the channels.

The work demonstrates the degree of flexibility that this technique offers and the speed at which prototyping can be carried out. The work set out above shows the potential to use pure fs ablation to rapidly prototype microfluidic structures. Optimisation processes (i.e. pitch separation, write speed, laser power, cross hatching operations and so forth iteratively tested as described in Figure 2-16) allow the system parameters to be easily modified to further improve the end result. It is also of note that the control

software also allows easy rescaling. The ability to ablate structures that are 2mm deep and the aspect ratios that accompany them created over a much shorter timescales than previously demonstrated, shows the potential for this work and served as a useful starting point for the continuing work.

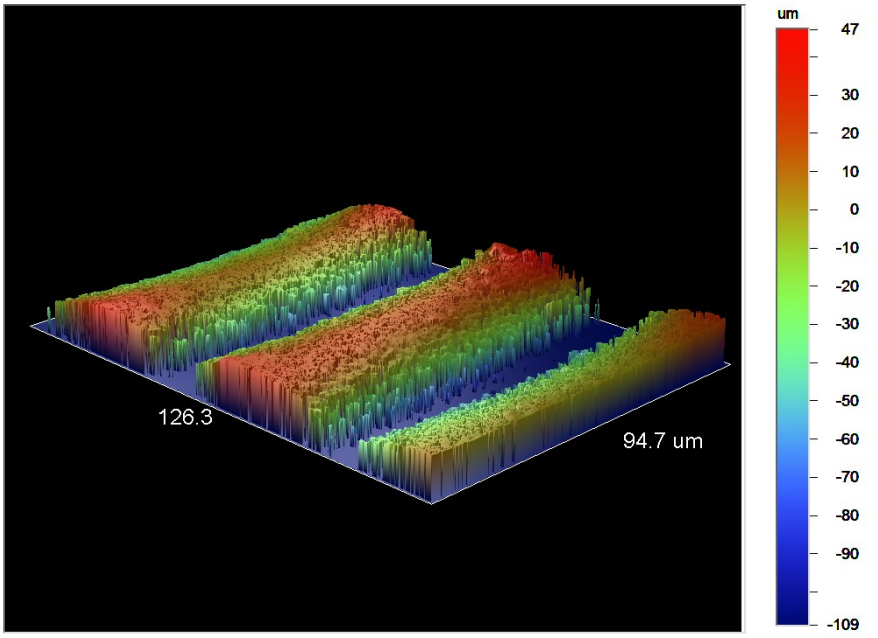

Figure 3-5 50x mag of top surface of the mixing channels showing the machined channels to be approximately 10µm wide. Profiling done by Charalambos Koutsides, processed by me.

3.3 Controlled shape generation + splitter

The CAD optimised approach as used to generate initial test samples was developed further for a number of the more complex devices. However, the generation of shapes using programmed motion was investigated to allow

fine control of the ablation feature. It was found that fine control of constructing the basic building blocks was an important aspect of the tool set required to create more complex structures. The initial trials with shape generation are set out below.

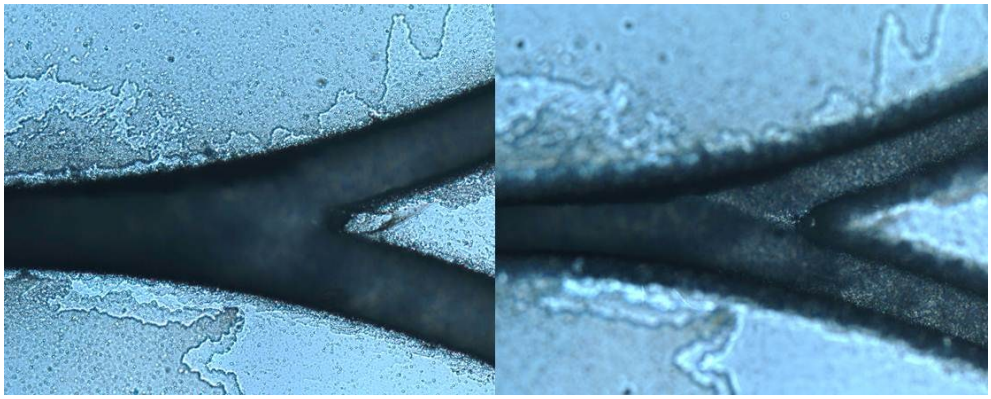

Figure 3-6 A micromachined splitter machined in fused silica microscope slides. The images show the top and then bottom of the channel. This was taken with a x20 microscope objective.

Figure 3-6 shows the machining of a splitter. This was achieved using minimal overwrite of the initial straight section. The results show sharp edges with no damage and smooth bottom surfaces. The sample had not been cleaned before the microscope images were taken to show how little recast was created. The sample may easily be cleaned to remove the minimal debris created and seen in the figure.

Various shapes were trialled initially in fused silica and BK7 glass but also Macor ceramic. The shapes typically of interest other than holes as set out in prior sections included cones, hemispheres, splitters and columns. These

were attempted through the use of positive and negative feature generation leaving concave and convex shapes as the resultant.

Through the use of coding loops, lens selection and fine stage control the angles and curvatures of the given shapes were able to be set resulting in cones of different radii and slope angle or micro lens like structures of controllable curvature. This is achieved through control of the loop counters and their effect on the vertical and horizontal pitch and total arc counts at each level. This is shown in Figure 3-7 below. This technique was demonstrated in a number of materials and selections of profiles are shown below.

Figure 3-7 shows a non-symmetric cone micromachined into a Fused Silica sample. The profile shows clearly a defined high aspect ratio edge, to the top of the resultant image, and variable slope on the opposing side. The slope at the bottom of the image shows a controlled curved slope. This was trialled to demonstrate the potential for the creation of highly controllable surface reliefs.

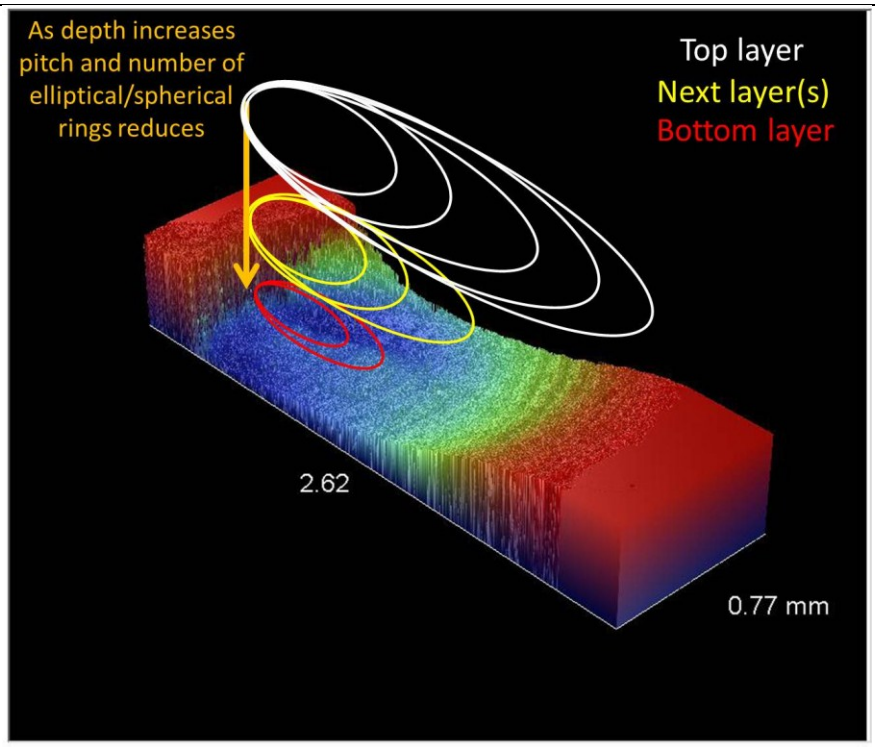

Figure 3-7 A schematic showing how through control of the pitch of the machined arc and the number of arcs completed in a given level when combined with control over each vertical step height (between each processing level shown in different colours) a range of shapes can be created.

When the data is processed the degree to which the slope is controlled becomes obvious. This is shown in Figure 3-8 where a line profile is taken along the dotted yellow line in the 2D image. The resultant profile shows the curvature of the slope changing and the high aspect ratio of the slope that can be achieved.

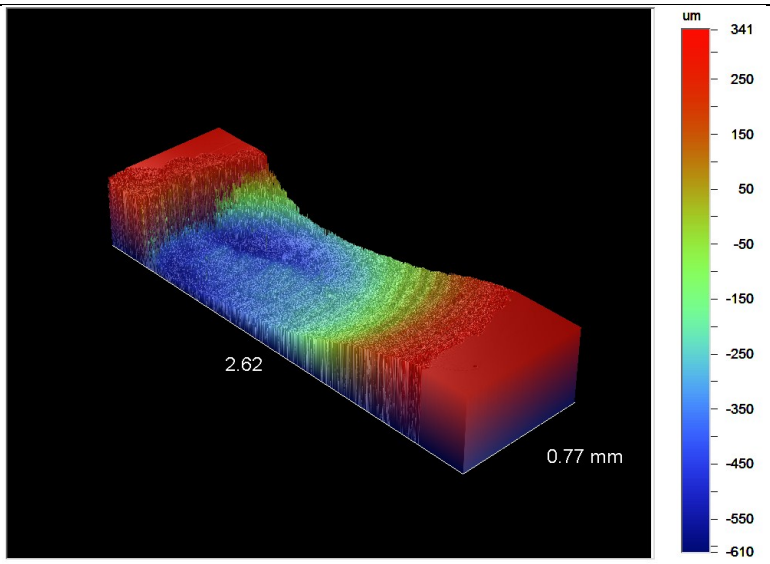

Figure 3-8 3D profilometry scan at a magnification of x20 showing a micromachined cone with deliberately curved profile on one side and high aspect ratio on the other. Profiling done by Charalambos Koutsides, processed by me.

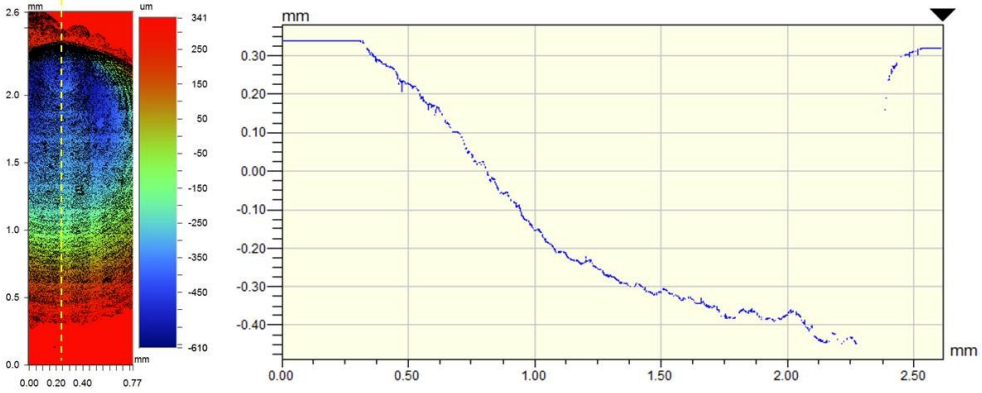

Figure 3-9 A 2D representation and profile recorded along the yellow dotted line showing the controlled curve of the bottom of the cone and high aspect ratio of the top side of the cone (left and right respectively on the profile plot). Profiling done by Charalambos Koutsides, processed by me.

The ability to control the aspect ratio at a chosen aspect ratio was demonstrated further by creating a linear profile instead of the curved one demonstrated above. This is shown in Figure 3-9. The slopes of this slope were deliberately controlled to be done in a series of steps. This would be of importance to those considering the shaping of devices to act as lenses in a range of applications including, microlenses and THz lens creation.

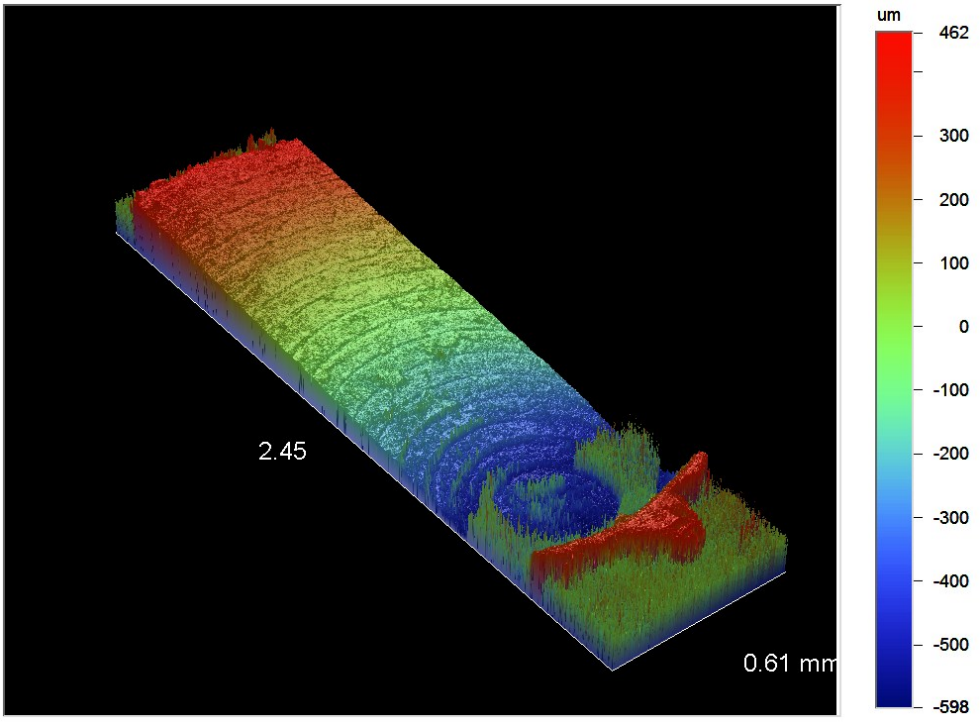

Figure 3-10 3D profilometry scan at a magnification of x20 showing a micromachined cone with deliberately linear slope profile on one side and high aspect ratio on the other with step like structures created. Profiling done by Charalambos Koutsides, processed by me.

The slope is shown for the linear sloped non-symmetric cone machined. This clearly demonstrates the controlled variations that can be achieved. This is shown in figure 3-10 below.

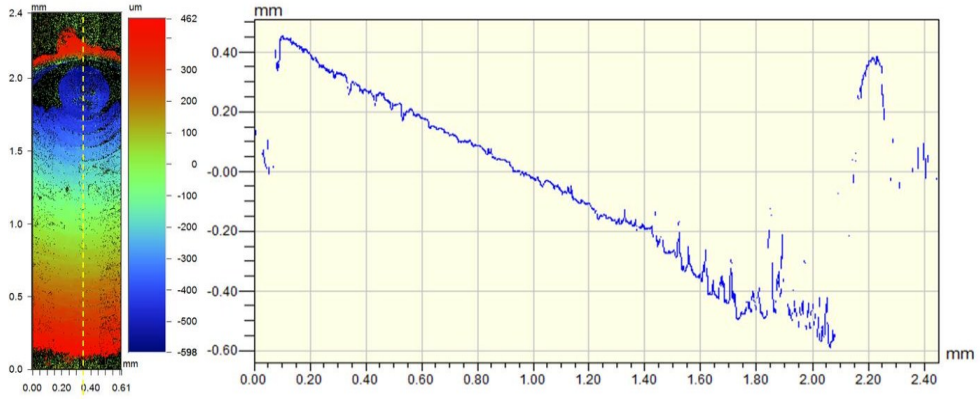

Figure 3-11 A 2D representation and profile recorded along the yellow dotted line showing the controlled linear slope of the bottom of the cone and high aspect ratio of the top side of the cone (left and right respectively on the profile plot). Profiling done by Charalambos Koutsides, processed by me.

Figure 3-11 shows the potential to create more complicated Fresnel and other corrective/adaptive lenses through selective removal of material. The figure shows a slice in a larger circular pattern of such a structure. This variation in ridge pitch, height and channel depth can be easily varied through control of the stages and choice of lens. It shows the potential for rapid prototyping of these devices, however, the surface roughness would need to be either improved or post-processed to make these viable devices at most wavelengths.

The technique has applications in THz devices, micro lens creation and other fine feature creation. It is unlikely to replace lithographic techniques

for the creation of textured surfaces due to the write times involved but the techniques show promise for rapid prototyping of small scale devices.

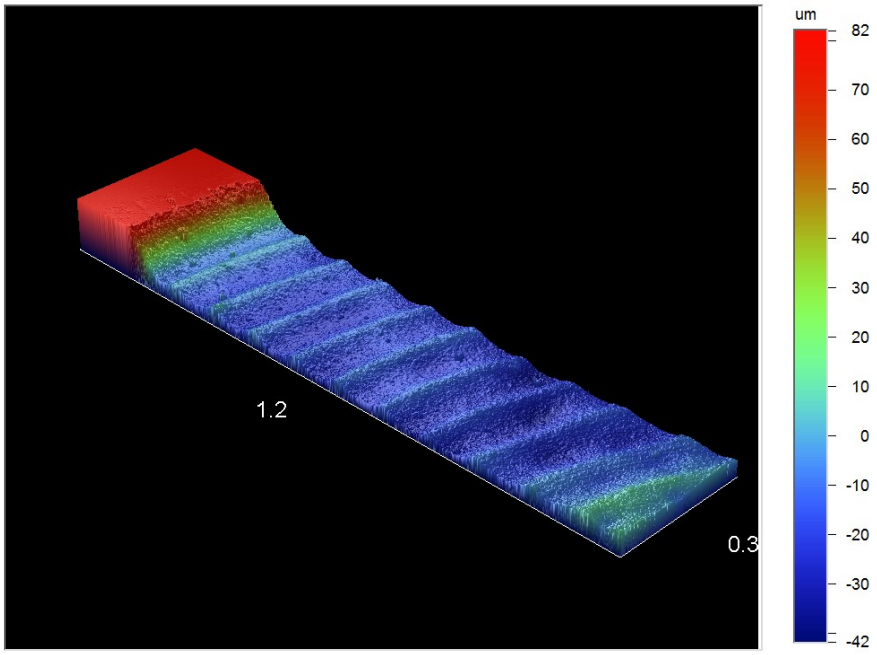

Figure 3-12 A radial pattern of surface relief created using the selective removal of material through fine control of the coding. The scan was taken at a 20x magnification. Profiling done by Charalambos Koutsides, processed by me.

The most significant limit to the process being used for optical materials alone is that the surface structure left at the bottom face is often rough and acts as a scattering centre. This may be improved through complex rastering patterns, however, the fundamental limit of the spot size being the area having sufficient energy to heat the glass to the 1700 degrees required to liquefy and smooth will limit the potential to create optically smooth surfaces. The use of post processing may assist in this but was not investigated as a focus of the work presented here.

3.4 Smooth surfaces

As partially described above one of the key limitations to femtosecond micromachining is the surface roughness of the resultant sample surface. The side wall quality is generally very acceptable as often this is smoothed by the side of the filament type plasma focal spot created. This means that the roughness is generally accepted to be sufficient for most applications. The largest surface roughness is created at the base of a machined area. Here a ploughed ridge and furrow or dappled surface relief is left after ablation. This is often accentuated when the debris created by prior ablation then obstructs the further ablation by blocking the beam or attenuating it. If unaltered this can lead to micron sized defects being created. To work around this a number of techniques were applied including extraction, focused air flow over a work piece and working in liquids. For most applications the combination of extraction and focused air flow were enough to remove the particulate matter without coating the objective lens or allowing it to resettle on the area of write. The use of liquids was experimented with when working on GaAs, however, this largely led to a coagulated string of debris that was not removed in the improvised set up and was thus found to be largely ineffective.

Traditional laser machining techniques suggest the use of soft focusing. This is a description of using a high power laser such as a Copper vapour laser to effectively melt the glass resulting in a smooth surface. This is achieved by both moving the sample away from focus and reducing the power significantly. This has the effect of increasing the working area and

reducing the temperature the material attains. The technique relies on the temperature exceeding that of the melting temperature of the glass. This then allows surface tension to dominate and upon cooling form an optically smooth surface. This technique does not work with femtosecond lasers for a number of reasons. Firstly the spot sizes created are often too small to create the dimensions often required to create anything more than a very small area of melting. This leads to inconsistencies of surface on larger scale of several to tens of micron. The second reason is that due to the use of focused beams to create nonlinear excitation mechanisms the power of a femtosecond laser does not need to be as great. This results in soft focusing not having sufficient power to melt the glass away from the focal spot, and certainly not on the scale that would improve the surface finish.

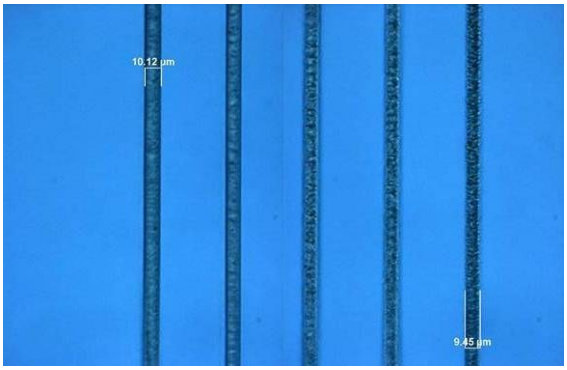

Figure 3-13 A microscope image of a BK7 slide with decreasing pass number from left to right. The number of passes are (from left to right) 16, 8, 4, 2 and 1 at 8µJ per pulse.

Figure 3-12 shows a test carried out where the number of passes along the same line at the same height was undertaken. It showed quite visibly that when the number of passes increased there was an observable smoothing of the channel left. Although the dimensions of the channel are slightly

increased the result is clearly better if not optically smooth. With any device the write time would have to be taken into account and the cost-benefit would need to be considered. The improvement is thought to be due to the fact that all of the potential material that could be removed would be. This is not considered to involve any melting effect as would be observed with soft focusing of a high powered laser due to the low thermal nature of the femtosecond pulse-material interaction.

Even when a surface has been finished with care, debris can become an issue obscuring the beam and leaving a modulated surface relief. This can be seen in Figure 3-13 where an etch depth test resulted in areas of roughness creating a dappled effect. This issue can be reduced through the use of air jets and liquids and was done so for most future machining. This works to remove the ejected material away from the channel or area of interest. In doing when the matter settles it is away from the work area or has been removed using a filtered vacuum arrangement. This avoids results of this nature and was found to be vital in efforts to reduce the roughness seen. The roughness seen when this profiling scan was analysed was *Ra* 493.66 nm, *Rt* 20.5 μm and was taken with a magnification of x20.

There are a number of options to improve this, including the use of high powered lasers and HF acid to finish these features, however, the use of HF was avoided as the focus of the development away from inscribe and etch techniques and no high powered lasers were available to try the soft focusing.

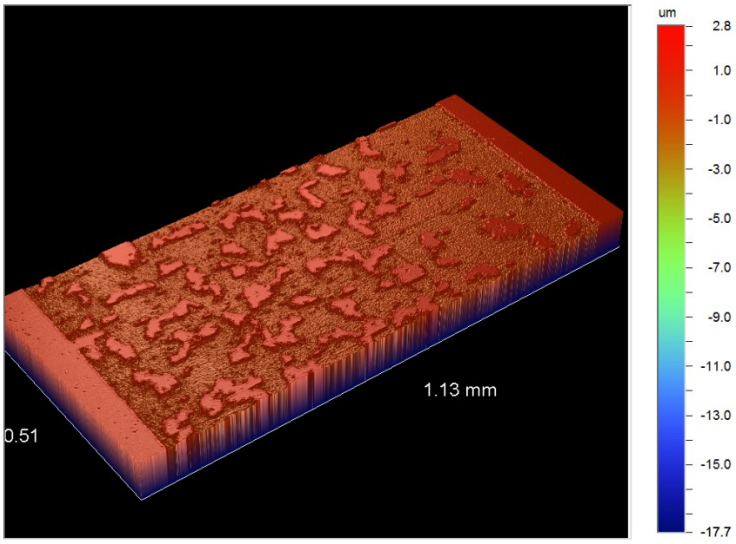

Figure 3-14 Etch depth scan profiled. The profile shows the result of unwanted debris re-settling on the surface and obscuring machining of the desired region. Profiling done by Charalambos Koutsides, processed by me.

It was found that if the number of passes could be reduced to create a specific depth it would result in a finer surface roughness. This when combined with cross rastering, rastering with translation lines at differing angles in the same focal plane, resulted in a surface finish that was sufficient for use with fluids. This has to be qualified by adding that the lamina flow at the surfaces was not examined in great detail in the initial trials presented in the next sections. The liquids served to even out the roughness, as an index matching fluid does, resulting in surfaces that could be viewed optically.

3.5 Aspect ratio control- slopes for other materials

The structures demonstrated in section 3.3 were not only able to be created in transparent material. The creation of high aspect ratio columns of different dimensions was achieved in Macor as well as Fused Silica. The results show a very circular column being left when the substrates are machined away. The remaining structures have, for their dimensions, good mechanical strength due largely to the lack of stress or damage created during the machining. Figure 3-14 shows one of the columns fabricated in Macor.

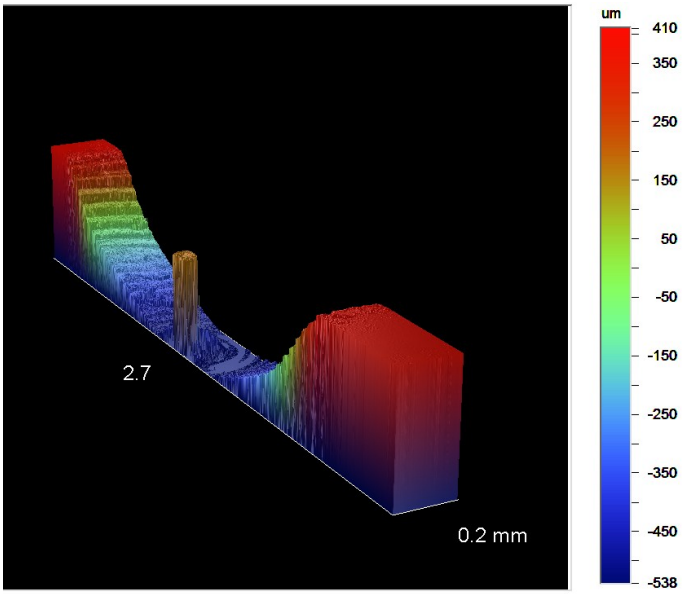

Figure 3-15 A single column formed through control of machining forming an antenna like structure in the ceramic Macor. Profiling done by Charalambos Koutsides, processed by me.

Through taking a profile through the centre of the column a measure of the dimensions of the column was achieved. The column was measured to have a height of 0.706mm with a width of 0.076mm highlighted in the

yellow channel in figure 3-15 below. Although not a record aspect ratio, the control of the aspect ratio is of particular interest to those working in antenna. The bowl like feature was created to demonstrate that it could be formed to be symmetrically and act as a focusing "optic".

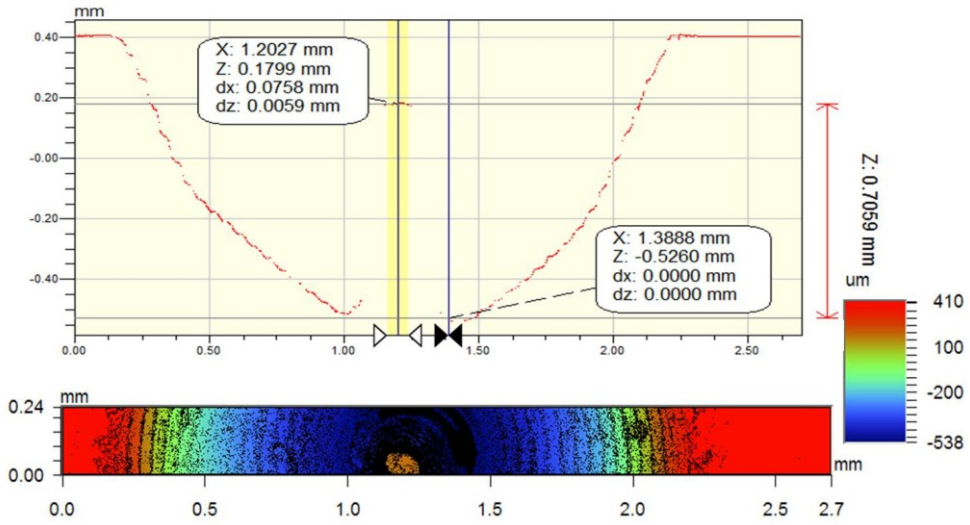

Figure 3-16 Profile and 2D plot of the column structure created though removal of Macor around a central zone. Profiling done by Charalambos Koutsides, processed by me.

3.6 Chemical sensing devices

The work in this section was carried out with Tanya Hutter of Cambridge University who had previously worked with these cantilevers and together the designs were adapted to facilitate the use of femtosecond laser micromachining in their fabrication. The machining was carried out entirely by me.

The use of microfluidic test beds for chemical sensing is a growing field. They allow for chemical testing with very small samples and so facilitate more rapid development of chemicals at much lower costs. The devices designed and fabricated here are designed to be used with functionalised sensors to detect tiny amounts of specific compounds. The details of the chemical functionalization were not the focus of this research and so have not been discussed in detail.

3.6.1 Design and reasoning

There were two types of design that were the focus of chemical sensing devices both based on cantilever approaches. For clarity they will be discussed in detail below.

3.6.1.1 Micro-cantilever sensors

Micro-cantilevers are extremely sensitive sensors that rely on the development of surface stresses to create a detectable change. Through chemical functionalization of the gold top surface they can detect the presence of compounds or chemical structures. Through the selection of the coating layer a specific analyte can be chosen and detected. Thus when combined, several cantilevers with different functionalization can be used to detect a number of properties of a chemical compound. The bonds created between probe and analyte are through the hydrogen bonding, electrostatic and van der Waals forces. The interaction of the analyte produces either tensile or compressive stresses through attraction (bends upwards) or repulsion (bends downwards) respectively. The amount of deflection depends on the amount of analyte that bonds to the probe and can cause both static and dynamic modes. The dynamic modes are in effect

a microbalance using the resonance as a means of determining the mass of the additional analyte. The basic outline of motion is shown below in Figure 3-17.

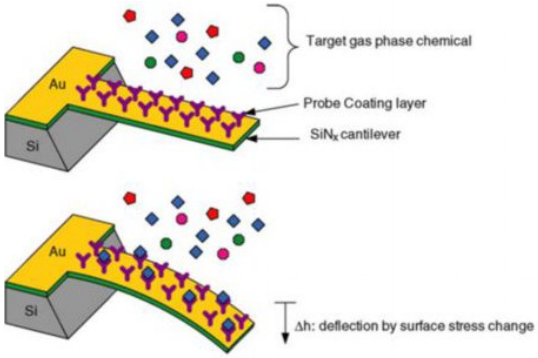

Figure 3-17 A schematic showing how the presence of analyte creates a bend in the cantilever. Image by Tanya Hutter.

The sensitivity of these sensors can be calibrated for in advance by changing the thickness or cantilever length. They are commonly examined via either electrical signals produced by the bending motion changing a materials resistance i.e. piezoresistive detection, or by using a laser beam and quadrant detector. The technique that these prototypes were designed for were going to be characterised by using phase shifting interferometric microscopy which allows for multiple sensor readout based upon the displacement of all of the cantilevers using only one light source.

Using these cantilever chips coated with different monolayer probes these devices can be used to detect the presence of chemicals and compounds in both gases and liquids. The traditional techniques for building these cantilevers into devices use lithographic methods. Although well-

established these techniques do not offer rapid prototyping that the development of designs and combinations of layers requires and are often quite expensive due to the mask creation as the number of levels of the microfluidic device increase. This is where micromachining comes into play in this work. The designs in Figure 3-18 below demonstrate the proposed development of the levels.

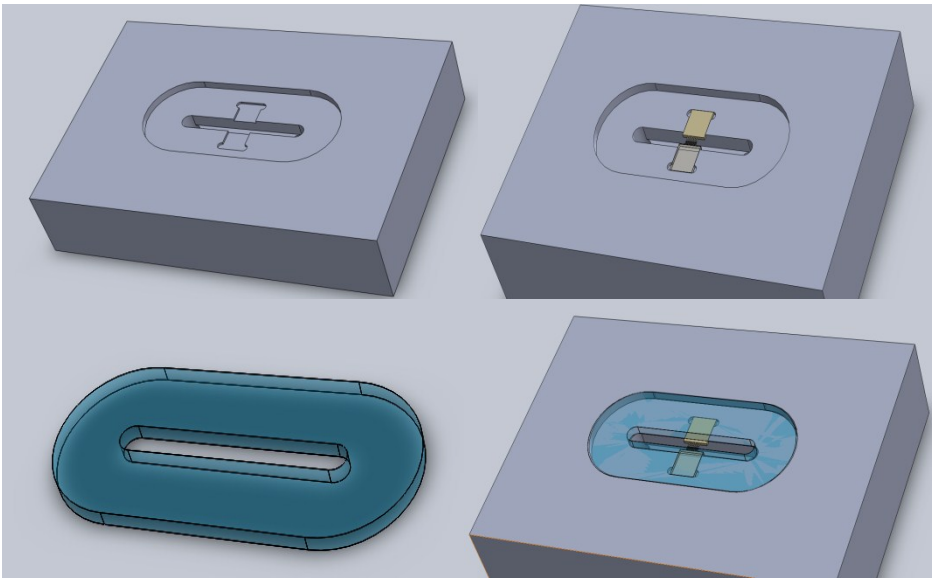

Figure 3-18 Designed micromachined slots, with cantilevers, PDMS seal and all together then a glass slide is place on top to seal the whole cell and to allow optical readout. Design in collaboration with Tanya Hutter.

The design parameters were specified to closely fit the cantilever devices, allow microfluidic motion of liquids and be bonded with both glass and PDMS. This meant that the choice of Borosilicate and fused silica substrates was optimal. The dimensions specified by the chemical collaborators were as shown in Figure 3-19 below. The depth of the central micro channel is 615nm, and the depth of the micro cantilever slots is 315um.

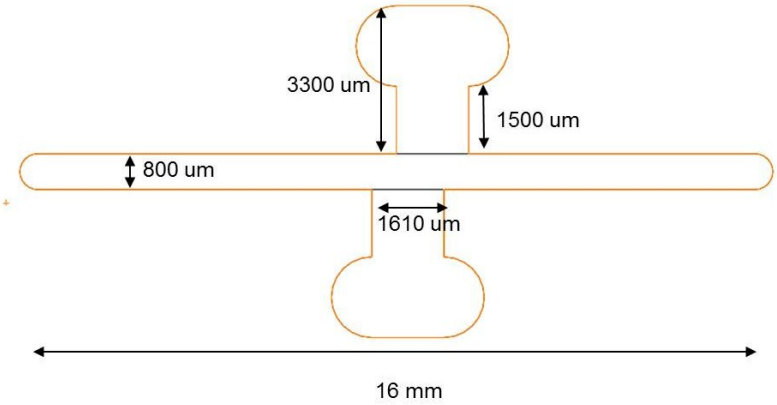

Figure 3-19 A schematic showing the dimensions of the designed chemical sensing model part with the cantilevers being placed in the two wells either side of the central microfluidic channel.

3.6.1.2 All fibre micro-cantilever sensors

Through the tapering and functionalization of an optical fibre and using it as a coupling device to another fibre another form of cantilever sensor can be created. This has been demonstrated [**98**] by using micro-precision stages and v grooves; however, it does not form part of a practical device outside of the laboratory. The use of femtosecond micromachining to form a stable and accurate substrate with microfluidic channel and fibre grooves was also experimented with and the prototype results presented in this chapter.

The vibration of the fibre cantilever is detected in a coupled power variation. The frequency response of the oscillations is dependent on the amount of analyte the probe layer has detected and can determine the concentration. The advantage of these devices is the low cost, small size and lack of free-space optics.

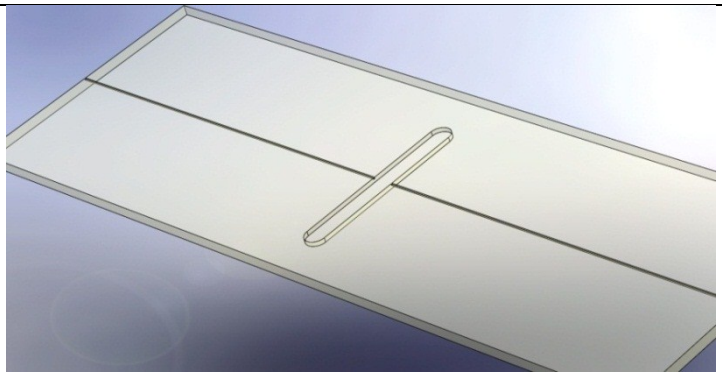

Figure 3-20 A single fibre groove split into two by a channel for a liquid or gas to be present. Design in collaboration with Tanya Hutter.

3.6.2 Application

Both types of sensor have the ability to be used as remote chemical sensors, or for the detection of various chemicals in gaseous states for example in the detection of ammonia, a biomarker for kidney problems in the parts per billion regime. These can also be used to detect air pollution and be used in a range of industrial and agricultural applications for the detection and treatment of processing of crops and safety devices. The focus of the work presented here is as a demonstration that the femtosecond laser micromachining techniques developed can be used to prototype a range of microfluidic structures and structures at lower cost and time than the traditional lithographic techniques.

3.6.3 Results

The initial devices were fabricated in borosilicate glass slides and through varying the lens, power and focus height the dimensions specified were iteratively met. The work in both examples presented below was carried

out using the Aston micromachining system operating at 1 kHz, using the f=66mm objective lens. This initially led to the device being flat, as shown in Figure 3-21 below.

Figure 3-21 A picture taken of an initial chemical sensor device showing the smooth side walls and design shape being achieved. The length of the artefact was 16mm as shown in Figure 3-19.

The design was altered and a step was added to the central channel as seen in Figure 3-22. In all three images you can clearly see the high aspect ratio created and relative transmission levels. The level of surface roughness reduction was thought to be sufficient given that the channel would be in liquids of approximately the same refractive index and as such would aid to reduce the effect of the surface roughness. As discussed later in this chapter there are techniques being currently developed to overcome these issues.

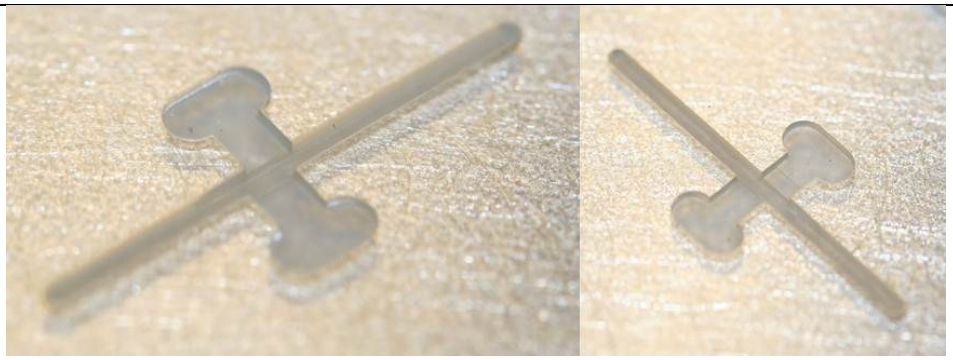

Figure 3-22 Through iteration the images show a ledge for both sides so that the cantilevers rest above the base of the central channel.

The dimensions of the key parameters were measured using a transmission microscope and the key images are presented in Figure 3-23 and more broadly in the schematic of the design in Figure 3-19.

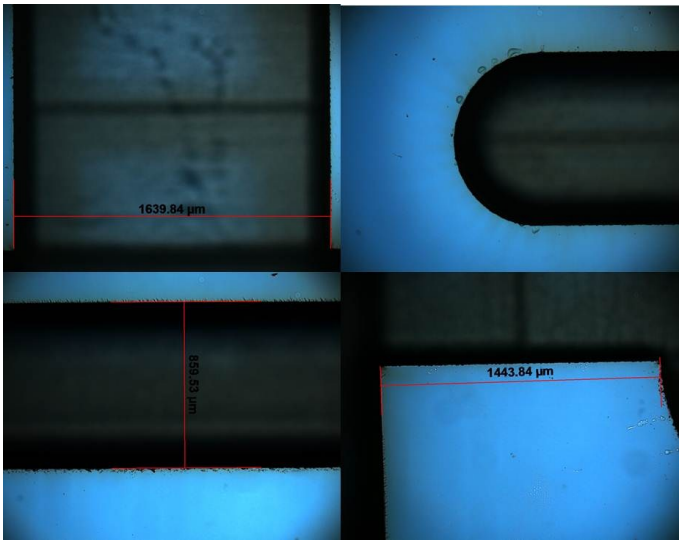

Figure 3-23 Microscope images taken showing the parameters meeting the design and smooth, undamaged side walls with good aspect ratio channels.

The devices were tested by Tanya Hutter at Cambridge University and were found to be too close to specifications in the width of the area to insert

the micro-cantilever chip but after iteration the devices showed initial promise for use in their sensing applications.

The fibre cantilever developed from the initial designs proved to be more of a challenge. The complexity had increased from the single channel to a three fibre array. The grooves proved to be a good way of consistently holding the fibres, however, the alignment between the opposite sides proved to be a challenge when used in practice. This should not have been due to the alignment of the channels as the stages have nm accuracy, however, it was thought that in future devices the device width could be shortened to reduce any potential issues from the fibre bending under the unsupported weight. Although this may sacrifice sensitivity it is expected that this will not adversely affect the device too much.

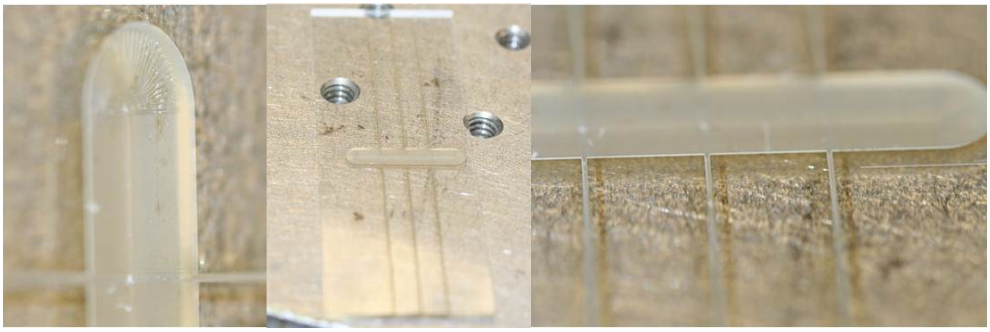

Figure 3-24 A 3-fibre cantilever sensor device. Images show the result of CAD to G-code oddity at a curved central channel, the overall device and 3 V-grooves for the fibres to sit precisely in. The slides used are 26x76x2 mm.

It is a feature of the way the CAD to G-code produces curves that on occasion it can create the fan structure seen in Figure 3-24 above. This occurs when the stages start working from the inside out, the discretised nature of the motion (i.e. a curve being made of a series of straight lines)

results in the edges causing the beam to be refocused at the corners creating the ridges. The figure also shows how well the v grooves are tapered. This tapering was deliberately created by reducing the number of passes at lower depths, by doing this it created a sloped side wall and the desired v shaped groove.

3.6.3.1 Conclusions

Section 3.6 has demonstrated the rapid prototyping of devices for chemical sensing and shown how some of the techniques developed earlier for the structuring of planar substrates through femtosecond laser micromachining machining. The techniques have allowed for development of techniques for chemical analysis that are not readily available using traditional methods with a versatility to iteratively develop full sensors in a short time frame. The challenges of surface roughness will need to be met; however, the work shows the potential for further study.

3.7 Transparent radial coupled centrifugal impeller blood pump

This work was carried out with Professor Geoff Tansley, Dr Laura Leslie and Graham Lee at Aston University. The designs were created in prior work by Professor Geoff Tansley and underwent only minor iteration during the course of the work presented here. Laura and Graham contributed to some of the characterisation and iterations. I undertook the machining work alone. The last profiling result was scanned by Charalambos Koutsides at CUT; the data was then processed by me.

Fluid mechanics has contributed to solving several issues in the fields of biological, physiological and in the development of artificial organs. The artificial heart valves and pulsatile ventricular devices have been the focus of a lot of study with an ageing population suffering more and more from heart related ailments. The development of non-pulsatile devices has become a key focus of the next generation of artificial hearts. These blood pumps have the advantage of being comparatively simple, compact, easy to handle and relatively inexpensive as compared to the displacement ventricular artificial organs. The main flaws that have been identified with this type of device have been in the development of Thrombus formation from excessive heat and force caused by friction. This previously made the devices useful for only a few days. Through the development of magnetically suspended impellers devices are now in patients and have the patients are alive after several years. This has been achieved through fine control of the etch depth of the radial arcs.

Blood is typically considered to be a disperse particulate suspension. The fluid dynamics of which in Couette flow regimes is largely not well understood. When blood experiences shear stresses, cells frequently undergo functional changes or even cell death. This causes significant implications for the engineering design of implantable devices. This is carried out; however, as yet the level of shear at which damage occurs is ill-defined. Preliminary evidence suggests cell exclusion may mitigate shear-induced damage, but this has not been rigorously investigated thus far [**99**].

The fundamental behaviour and response of cells within blood when subjected to shear stress, and testing the hypothesis of beneficial cell exclusion from areas of high shear stress is the prime motivation for developing impeller pumps. To fully optimise this characterisation is required of the blood velocimetry. This is particularly difficult in devices made out of metal when the interrogation is carried out optically. The traditional milling techniques applied to steel cannot be applied to glass as they either cause micro cracks or opaque finishes. Through the use of the ultra-short properties of femtosecond micromachining these issues can be overcome for initial trials. This section details how these initial test samples were developed and characterised.

3.7.1 Theory of blood pump

The key aspects of consideration in the design and analysis of a blood pump are the geometric form and biological constraints. The two will be discussed briefly in the context of this architecture.

3.7.1.1 Geometric constraints

The first design constraints that were considered are the inner and outer diameter. Due to the planned method of inspection in pre-existing equipment the outer diameter was specified to 2.5 cm with an inner diameter of 0.8 cm. The relationship between the two radii forms the parameter ΔD, the ratio of inner to outer radius. This parameter then is related to the bearing load capacity by the equation,

$$F^* = \frac{Fh_0^2}{\eta\omega R^4} = \frac{3\pi}{2}(1 - \Delta D^4)g_1 C_2 \qquad \text{Equation 3-1}$$

Where, F^* is the dimensionless load capacity, F is the load capacity (N), R outer radius (metres), r_i is the inner radius (metres), η is the viscosity (mPa.s), ω is the angular velocity (radians/second), h_0 is the film thickness (m), g_1 is defined in Appendix B, C_2 is defined in Appendix B, ΔD is the ratio of inner radius to outer radius. This clearly shows that for a fixed outer radius, set by the testing machinery (seen in **Figure 3-25** below), as the inner radius increases the bearing load capacity reduces i.e. as the surface area increases so too does the load capacity. This means that the parameters that are available to be experimented with are the groove depth, groove angle and the number of grooves.

The test rig shown in Figure 3-27 shows the blood bearing interface being connected to the drive shaft and a load cell monitoring the axial force and load capacity with any given rotation speed. The unit is currently made of stainless steel and has yet to be fully adapted for optical inspection. The imaging of the channel will be facilitated by keeping the fabricated glass bearing static while rotating the other face. This is possible because the forces on the blood cells are identical to those experienced if the bearing was the rotated part. In this way the flow can be observed using microscopy techniques at various points along a single spiral arm facilitating the characterisation of the flow and cell exclusion patterns.

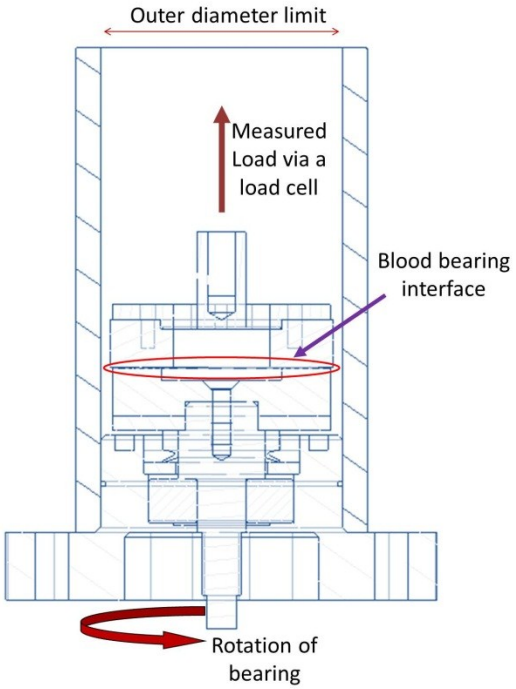

Figure 3-25 A schematic of the blood bearing test rig inspection set up. The bearing or facing surface is rotated via the bearings below, the blood acting as a lubricant at the same time as being accelerated and the load cell measures the load. The optical inspection arrangement will be arranged around this design to be fixed on one arm while the secondary (non-grooved) face rotates.

3.7.1.1.1 Groove depth

The relationship between the groove depth and the load and thrust of the grating is critical in the understanding of the workings of the impeller. The ratio of the film thickness and the groove depth gives a parameter referred to as δ, where δ = film thickness/groove depth. The choice of the pair of values depends on the desired load capacity so for a load of 12N groove depths of 200µm and film thicknesses of 70µm would be appropriate with the prediction of an optimum value of δ=0.35. The load capacity is critically

dependent on the groove depth, for a given film thickness and vice versa. This key dependence means that the groove depth is of key dependence to the performance of the bearing.

3.7.1.1.2 Number of grooves

The number of grooves has a direct effect on the load bearing of an impeller. The load bearing of a bearing can be increased from 0 to 10N by increasing the number of grooves from 0 to 5. This is a sharp increase that plateaus with further increase in groove number. By increasing the number of grooves to 20 an extra 2.5N of load can be achieved. For the initial trial the number of grooves was chosen to be 15 which represented a near optimised value without leading to significantly increased writing time.

3.7.1.1.3 Bearing angle

The angle of the groove has an important role to play in the increase in load capacity. This has been found to be optimal for angles between 12-17 degrees. This has been incorporated into the bearing angle design.

3.7.1.1.4 Non-geometric physical factors

The speed of rotation plays a significant role in the increased capacity to take load in these bearings. The linear relationship was not a key factor in the design, but the material would have to be able to withstand rotation speeds of at least 2000rpm and was part of the reason for the choice of fused silica for its mechanical properties. At these rotational speeds loads of 12.5N are feasible.

3.7.1.1.5 Spiral shape construction

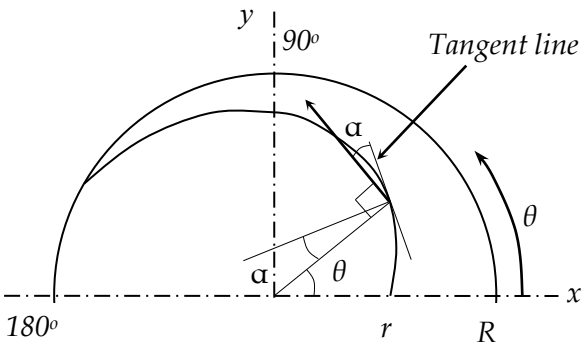

Figure 3-26 A schematic showing the design curve of the radial spiral.

The spiral chosen for study was previously designed in prior work. It was chosen to be a logarithmic spiral defined by the equation,

$$r(\theta) = r_i e^{\theta tan\alpha} \qquad \text{Equation 3-2}$$

The radius of the spiral is a function of the angular position around the rotational centre of the bearing.

Combining all of the above factors the spiral was designed to have an angle of 15 degrees, 15 grooves an inner diameter of 0.8cm and outer diameter of 2.5cm and experimenting with the groove depth. This results in a design that looks like Figure 3-27 below.

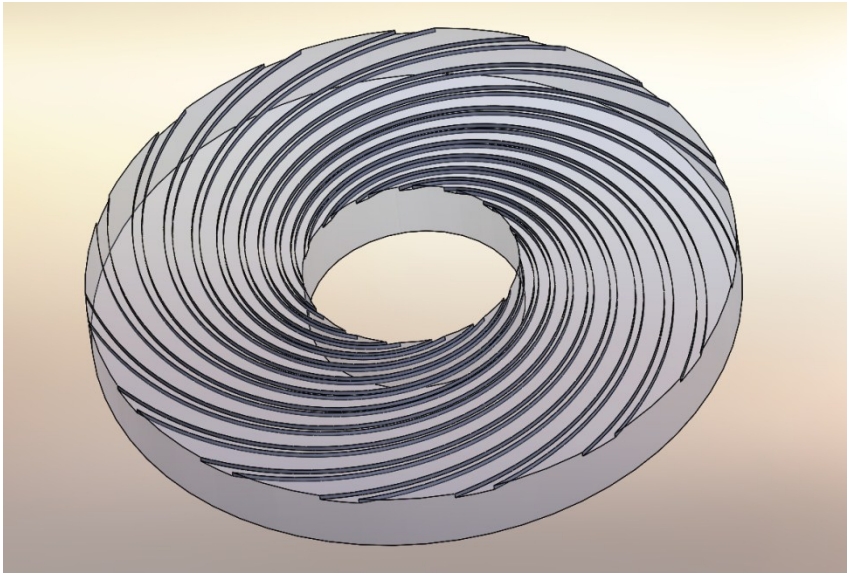

Figure 3-27 A schematic of the final blood pump design showing 16 spiral grooves with a groove depth of 250µm. Design in collaboration with Professor Geoff Tansley, Dr Mark Prince and me.

3.7.1.2 Biological considerations

The blood cells in human blood are subjected to shear stresses in prosthetic devices; these have only recently become the focus of flow dynamic study in rotational systems. The work has mostly been based around haemolysis (red cell collapse) after stress has been applied. The mechanisms that control the process of haemolysis in these pumps are barely understood. Cell membranes are thought to strain harden as a result of shear stresses, white blood cells also have been studied, but the fundamental processes are little understood. The lack of fundamental understanding results in rules of thumb defining the minimum gaps and hence stresses caused during Couette flow. These stresses that the blood can be subjected to before haemolysis and leukocyte apoptosis (cell death) occurs are critical to the

functionality of a ventricle assist device. The aim with this device design had been to reduce the exposure to the higher shear stresses and reduce the detrimental effects they have. This is hoped to be achieved through exclusion of cells in Couette flow through the use of the spiral which provides regions of low shear stress. The hope is that the cells will migrate to these areas leaving the plasma in the areas of higher stress.

3.7.2 Rational for using a transparent material

Although these structures have previously been developed in metals and form practical industrial devices the ability to study a number of facets of the cell behaviour in these types of devices to characterise the protective effect in the flow mechanisms has been a challenge. The ability to track cell numbers, cell identity in various regions of the bearing in real time cannot be achieved. The techniques used to do the characterisation are optically based and rely on microscope type techniques and thus the use of transparent materials is critical.

3.7.3 Models and coding issues

The model parameters outlined above were imported into a CAD model. This model was then attempted to be processed using a CAD to machine code software package. This had many issues with the complexity of the splines and small nature of the groove channels. To counter the issues the model was simplified using SolidCam to one groove and then again into two parts. The spiral was separated into two halves along the major spline axis. This significantly reduced the computational demands on the processor, allowing it to complete the computation of the spline. The code that was produced was then optimised by thorough parameter control and

removal of computer generated commands that were developing unwanted features. The two sets of code were then combined and then the rotationally wrapped using coding techniques. These were iteratively improved over the course of several trial runs of single arcs. At this point the lenses were chosen and write speeds optimised to be the f=33mm doublet lens and a write speed of $5mms^{-1}$.

The decision to use computer generated code and then post optimise it was taken as the complexity of the variable spline creation from equations would have been non-trivial and extremely time consuming. Whilst domain knowledge was, as a result, inputted through post processing of the code rather than from base code the result was a complex array of code that enabled machining trials.

3.7.4 Results of trials

The results of the initial trials showed a number of very positive achievements but also two issues that would need amending before significant testing could be started. Initial work focused on achieving the desired range of depths, the aspect ratios of the side walls and the channel widths. These were all achieved with the variation of lens, write power, speed and code. The primary test criteria were reviewed using the PDMS moulds and microscope images. An initial trial is shown below in Figure 3-28.

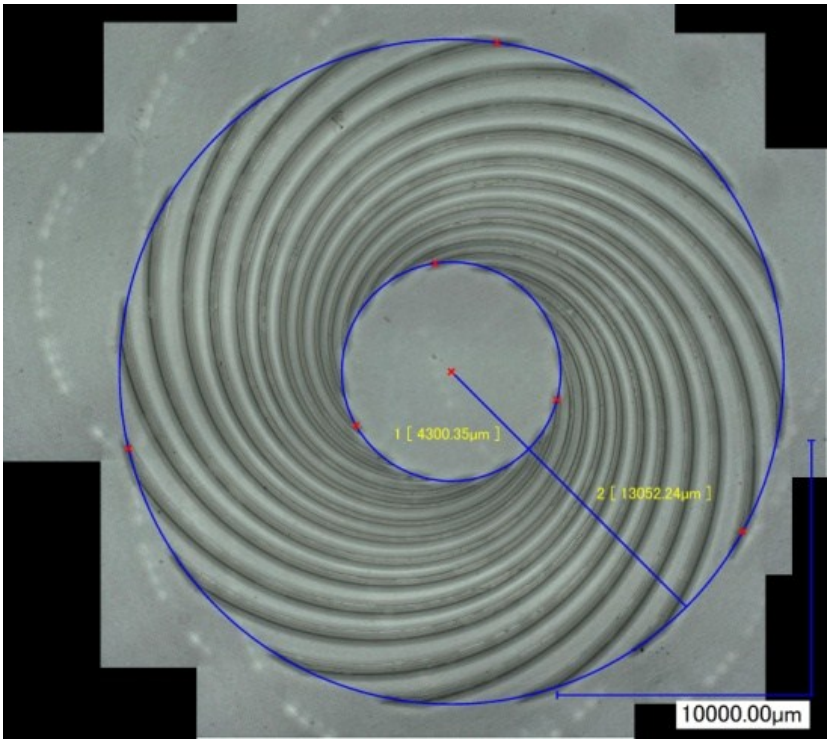

Figure 3-28 A stitched image taken by a digital microscope (Keyence) showing the machined spirals before it was machined out of the planar sample.

The figure shows a series of digital scope measurements stitched together to form the complete spiral bearing that is still set in the body of the glass substrate. The subsequent steps involved a series of angled tapered cylinders being cut so that the final disk was left free. Through using the angled taper away from the key feature of interest, i.e. tapered towards the centre for the inner radius and away from it at the outset a near vertical side wall was able to be created. This forms the final device as shown in Figure 3-29.

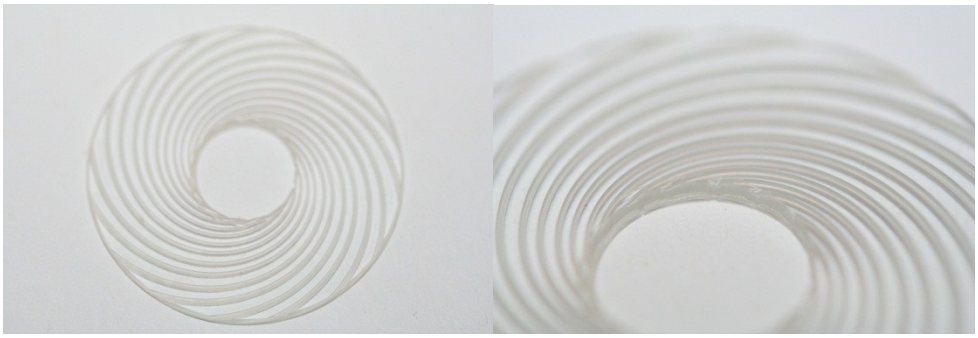

Figure 3-29 Finished trial device photos showing the disk with the radial grooves, the transparency of the machined channels.

The features were examined and measured using transmission microscopes and the key feature diameters are shown in the Figure 3-30.

The use of both microscopes and laser scanning profiling techniques demonstrate the two challenges to the works progression in the surface roughness of the bottom surface and the central groove that forms. The central groove is a result of the combination of the two sets of code splines creating an effective overlap of the machining. This is also exacerbated by the edge clipping that reduces the machining power towards the edge of

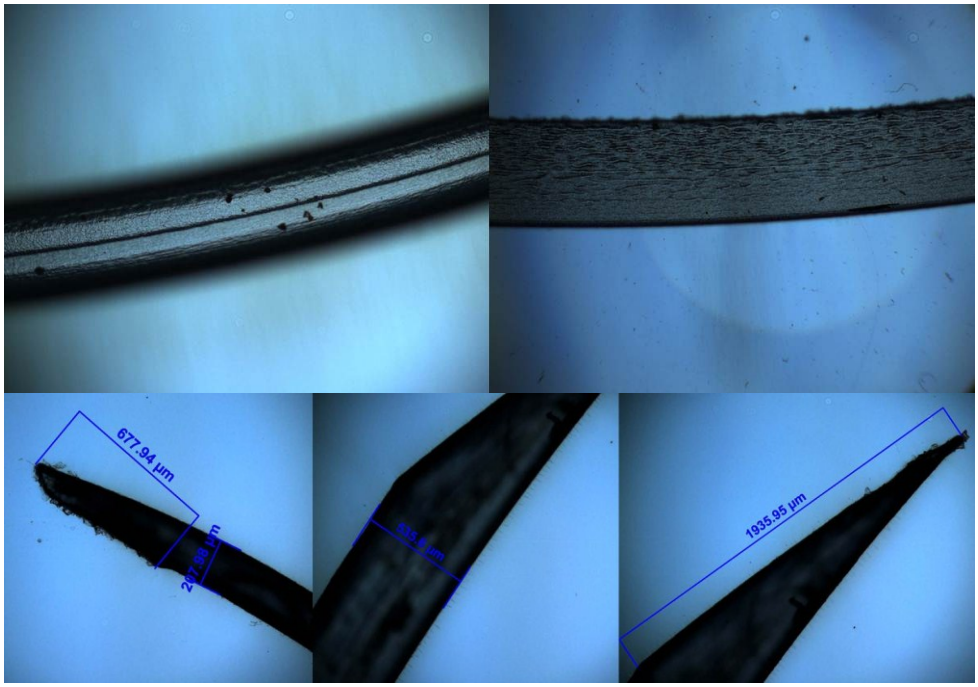

Figure 3-30 Microscope images taken to characterise the dimensions of the device. Images show clearly the central dip (highlighted further in profile scans below), bottom surface and critical flow entrance and exit dimensions.

the channels. This means that to attain the overall channel depth the centre has effectively been over processed. This is thought to be able to be corrected through altering the code to either reduce the power at during the central spline runs or to remove some of the passes for the central region as the depths are close to the final write depth.

The effect of the surface roughness is one that effects nearly all femtosecond and nanosecond machined transparent media. The use of complex rastering techniques can improve this, but rarely leaves an

optically smooth result even after extensive cleaning without the use of HF or similar. Even with the use of these chemicals the final surface finish is still not true optical quality. This may be able to be resolved through re-flowing the glass. When temperatures of around 1700K for fused silica are produced at the surface the glass reached liquid temperature and through use of surface tension the glass can become optically smooth. This has been applied for many years with CO_2 lasers but can also be achieved with glass processing techniques. This was not applied to this work but is the subject of further experimentation and is potentially to be a viable means of finishing these devices to an optical quality without using HF acid.

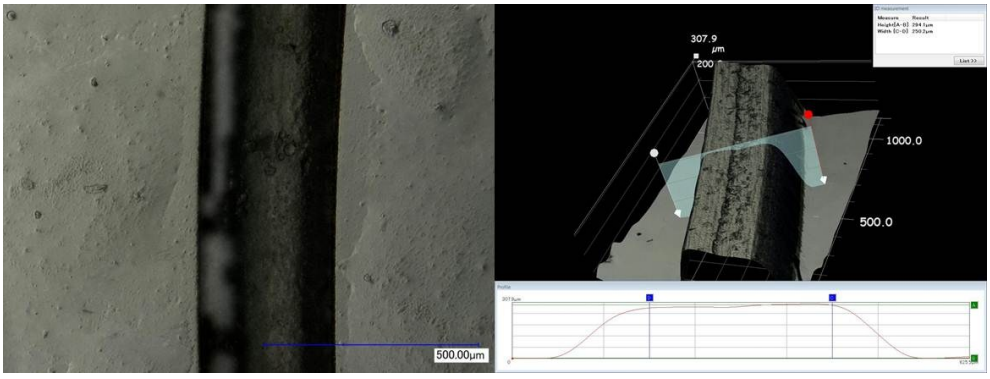

Figure 3-31 A digital microscope image showing the focus of both the top and bottom of a radial arm and a compiled profile using the digital scope of a PDMS mould taken of an arm showing the two surfaces present at the bottom of the arms.

Figure 3-29 shows clearly that there is a step in the bottom of an arm in the device. This is due to the code being combined from two separate arms due to the complexity of the shape and the CAD conversion software not being able to process it as one body. It should be possible to compensate for this through either finding a conversion package that can process the full CAD

model of through coding the spiral arm using the mathematical expressions developed by others in prior work. This second option was not fully explored due to the time consuming nature, however, with the latest version of the Aerotech stage control the splines would be able to be handled and should result in processing of a flat bottom surface feature which could be processed as detailed above. For confirmation of the PDMS mould scan the white light interferometer was used and figure 3-30 shows two scans of two separate parts of the same arm showing clearly that there are two steps.

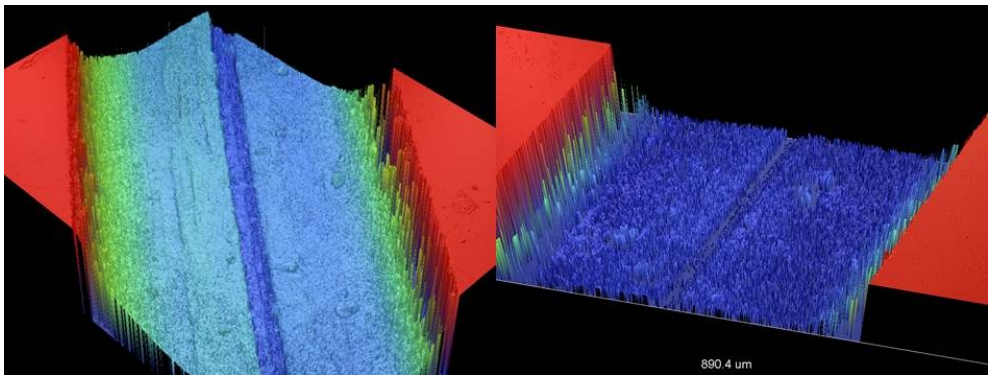

Figure 3-32 Two scans of a single radial arm showing on the left a two-step ridge and on the right a central groove within the machined channels. Profiling done by Charalambos Koutsides, processed by me.

3.8 Planar micromachining conclusions

Through the development of techniques to achieve the best surface roughness, fine control of the machined shape and aspect ratio-including creating very high aspect ratios and a development in the ability to work with non-micromachining experts to create practical devices that have enabled work to be carried out either at lower cost, in shorter development

times or to facilitate work that otherwise would not easily be achieved the potential and application of techniques has shown great promise. The challenges faced are considered to be surmountable through the use of post processing and improvements in the parameter files used for CAD-machine code software. Current work is on-going in exploring both areas with the assistance of material experts to gain more fundamental insight into how these transparent materials may be better produced specifically for micromachining including looking at processing steps in glass production and the subsequent effect on the fictive temperature. These combined with more flexibility in the wavelength of operation should yield the desired results in the near future.

4 Inscription

Having been able to process complex machining tasks and seen promise the natural course of this work was to examine the potential for inscription to be developed using some of the techniques that had been achieved to create practical devices that met real needs within photonics.

4.1 Introduction to femtosecond inscription and mechanisms

Femtosecond laser interaction with materials with pulse energies below the material damage threshold commonly known as inscription has been the focus of increasing research examining the potential for highly localised index change within the bulk of transparent materials. The reaction of the material leads to rarefaction and compression of the localised area within the focal plasma. This combined with physical chemistry changes to bonds in the form of breaking colour centres and crystalline structures gives rise to both positive and negative index change dependent on the material in question. The vast majority of work carried out has been to create waveguide structures using the resultant index modification or induced

stress fields from written defects to guide light through a range of materials. Whilst this has been achieved with low pulse repetition rate lasers very successfully the typical speeds of translation being below mms^{-1}. This combined with the main laser system's parameters not being ideally suited to the task being at 1030nm and with longer pulse duration of 500fs used for waveguide research and the nature of the optical set up not being ideal for inscription as for other tasks meant that other avenues were explored for the technology using similar techniques. The two key areas of study shown here were in the production of standard and complex phase masks for fibre Bragg grating (FBG) production and for use as phantom calibration artefacts for Optical Coherence Tomography (OCT). The two have non femtosecond prior production techniques for their fabrication but through using femtosecond lasers some advantages were sought and achieved. Both areas demonstrate the potential for the techniques to be developed to yield more robust and in the case of the OCT phantom a more accurate and comprehensive calibration device. The nature of the direct write techniques also lends itself to the artefacts and masks being rapidly prototyped especially important in the progression of complexity of both.

4.2 Femtosecond inscribed and micromachined phase masks

4.2.1 Introduction to phase masks

Phase masks have been used for the production of fibre gratings since Bennion *et al* first demonstrated their use to produce side etched gratings in 1986 [**100**]. In 1989 Meltz *et al* [**101**] showed that gratings could be directly

written into fibre using an interferometric approach involving a UV lasing exposure. However, it was the combination of these two approaches – UV writing through a phase mask by Hill *et al* in 1993 [**102**], that provided the necessary momentum for fibre Bragg gratings to become a mass produced commodity item.

There are many ways to classify gratings and some definitions that need to be expressed. First the gratings considered here are all transmission gratings. These diffract light to the opposing half space from the incident direction i.e. through them. This leads to spectral separation or beam-splitting depending on the incident light. There are also two fundamental types of gratings; amplitude and phase. The first periodically blocks light from passing through creating diffraction and the second uses phase of light to periodically alter it, often with two or more levels within each grating period, to again diffract the light only this time using it all.

Phase masks utilise periodic phase changes on the illuminating light created by periodic corrugations of the physical surface of the grating. These are commonly known as surface relief gratings. Typically surface relief transmission gratings are made of Fused silica. The periodic structure creates phase change through inducing periodic optical path length differences as the illuminating light passes through it. Fused silica with an index of approximately 1.5 has a large difference in refractive index compared to air at 1. The alternative is volume phase gratings which are imbedded within substrates. These historically have been produced by

forming grating structures inside dichromated gelatin (DCG). This is then sandwiched between two glass substrates and the edges sealed. These typically have significantly lower ΔRI and typically are larger in physical size to have the same diffraction efficiency. This induces a susceptibility to angular and wavelength sensitivity that surface relief gratings do not exhibit.

There are a number of definitions to make clear about the physical structure of surface relief gratings. The period of a grating is defined to be the distance between the equally spaced grooves. The resolution of a grating is the inverse of this and expressed in lines per mm. The depth is defined as the peak to trough measurement and from here on is referred to here as the etch depth. The duty cycle is the ratio between the linewidth and the grating period. The aspect ratio is the ratio of depth to width as in micromachining. It should be noted that although the figure shows a trapezoidal grating profile there are a number of other profiles such as rectangular and sinusoidal that are used for certain applications. The diffraction efficiency of a grating is defined as the proportion of incident light in a specific diffraction order and is largely dependent on the fine tuning of the other variables defined above.

Most commercial masks are produced using holographic steppers to create interference patterns; these illuminate photoresist (polymer) coated fused silica substrates. Polymers are by nature highly sensitive to environmental and thermal variations and so are used only as a step rather than the final

mask. Post exposure the resists are chemically developed using semiconductor etching techniques to leave solely fused silica. This produces high fidelity masks with diffraction efficiencies of close to 100%.

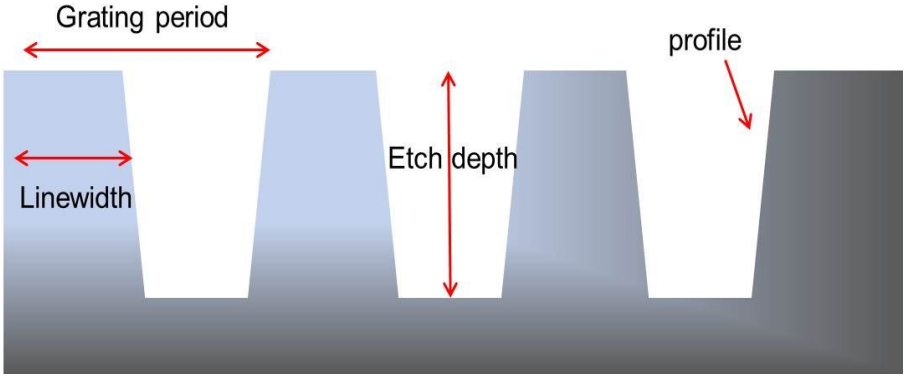

Figure 4-1 A schematic showing the definition of the terms describing the grating properties

The phase masks utilized in grating inscription are used to spatially modulate the UV-writing beam and are typically surface relief structures, with the gratings most often etched in fused silica (because of its low absorption of UV-NIR wavelengths) either through a holographic or electron-beam process. One of the advantages of electron-beam lithography over the holographic technique is that complicated patterns, such as quadratic chirps and Moiré patterns can be written into the mask's structure. However, lithographically induced phase masks usually are generated by stitching together small subsections (400µm x 400µm) of periodic corrugations on the mask substrate to fabricate large phase structures. An error in the precise positioning of the various subsections results in what is commonly referred to as stitching error **[103]**.

Holographically induced phase masks, on the other hand, have no stitch error. The masks act as precision diffraction gratings that upon irradiation by a monochromatic source divide the light evenly between two or more orders. These created orders interfere in the area behind the phase mask where they overlap and this interference pattern is recorded in the fibre to create the FBG.

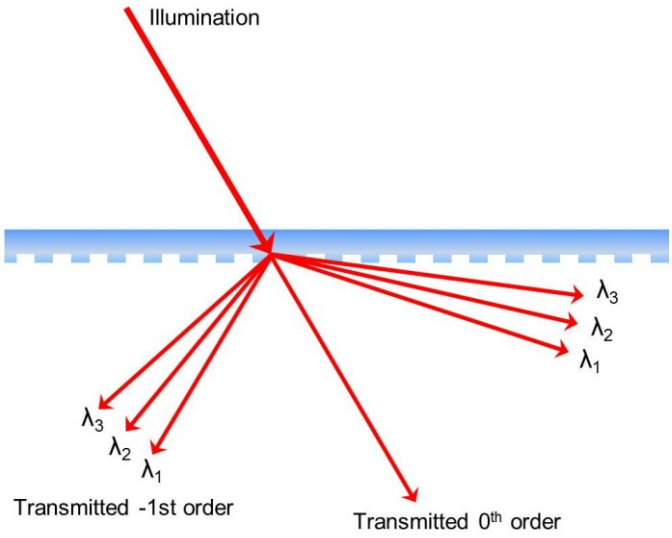

Figure 4-2 A schematic showing how when illuminated a phase mask creates ±1 diffraction lines and the transmission of the 0th order without deviation.

The incident and diffracted beams follow the general diffraction equation,

$$\Lambda_{pm} = m\frac{\lambda_w}{\sin\phi_m - \sin\phi_i} \qquad \text{Equation 4-1}$$

where Λ_{pm} is the mask period, φ_i is the incident angle, φ_m is the angle of the diffracted order, and λ_w is the wavelength of the writing UV beam, and m is the diffraction order from the mask. The m=0 order corresponds to the transmitted beam. In the simple case where the incident UV radiation is normal (φ_i = 0), the positive and negative orders have equal diffraction angles. The interference formed between the beams of various orders (m = ±1, ±2…) are used to generate the fringe pattern that inscribes a Bragg grating in optical fibres. In normal incidence equation 4-1 becomes,

$$m \cdot \lambda_w = \Lambda_{pm} \cdot \sin \phi_m \qquad \text{Equation 4-2}$$

Typical masks use either the +1/-1 (or 0/-1) orders optimized to diffract light equally and maximally into the plus and minus first orders (or zero and minus first order). Manufacturers optimize the mask designs to suppress additional orders where possible. The fringe pattern, Λ_{fringe}, created by the interference of two orders, with maximal suppression of all other orders, has half the phase of phase mask period, Λ_{pm}.

$$\Lambda_{fringe} = \frac{\Lambda_{pm}}{2} \qquad \text{Equation 4-3}$$

The suppression of the 0th order (far field) is able to be calculated in the case of a surface relief fused silica transmission grating as follows. If we assume that the duty cycle is 0.5 then we can say that half of the illumination passes through the grating trough and the other half the ridge. To achieve complete suppression the two have to be perfectly out of phase, via

variation of the optical distance between the fused silica and air is exactly half of the illuminating wavelength.

$$(n \cdot etch\ depth) - etch\ depth = \frac{\lambda_{incident}}{2} \qquad \text{Equation 4-4}$$

This can also be expressed as;

$$etchdepth = \frac{\lambda_{incident}}{2 \cdot (n-1)} \qquad \text{Equation 4-5}$$

Where n is the refractive index of the grating material. Taking the index of fused silica to be 1.5 this equation reduces to,

$$etch - depth = \lambda_{incident} \qquad \text{Equation 4-6}$$

This is a scalar approximation and does not hold for illumination wavelengths only a few times greater than the grating period.

Whilst most commercial development of this technology has used phase mask technology another approach was proposed by Mihailov et al in 1994 **[104]**. In this instance an amplitude mask, with line spacing of between 5 and 120 μm was imaged to produce higher order gratings. The advantage of this approach is that the mask structure can be easily and quickly manufactured without the need for lithographic technologies but first order gratings are difficult to make and the imaging optics required is quite costly. They also suffer from reduced light throughput as half is blocked intentionally to create the amplitude mask and create the subsequent diffraction efficiency loss.

4.2.2 Rational for using femtosecond inscription

Whilst the quality of commercially available phase masks is extremely good the use of them in other new areas such as femtosecond beam

inscription of grating structures and photonic bandgap printing can lead to their destruction or a requirement for rapid variation. The cost of phase masks, especially when out of the regular known recipes, combined with their susceptibility to surface damage such as scratches and dirt with the lengthy cleaning process means that if a thermally and environmentally stable sub-surface index feature could be produced it would have great benefits. This is in addition to the ability to rapidly prototype a more complex phase pattern that is in the nature of femtosecond direct write inscription. The nature of the mask fabrication method also demonstrates a potential for swift adaptation and tuning to meet specific applications through two routes; the manipulation of coding the motion of the sample relative to the inscribing laser beam, and control of the parameters for both the host material and inscribing laser. These factors, when combined, were believed to be significant cause for investigation of this area. The masks produced have been used to fabricate grating structures that can, and have been, used to write fibre Bragg gratings in smf-28 and doped substrates.

4.2.3 Experimental Work

The design, coding and fabrication of the phase masks demonstrated here were undertaken by me. The gratings inscribed using the masks were produced by Dr Kate Sugden at Aston University and the evaluation of the results was assisted by Dr Kate Sugden, Dr Kyriacos Kalli, Ian Johnson and Dr David Webb. The profiling was undertaken by Charalambos Koutsides with analysis performed by myself.

4.2.3.1 Fabrication of the masks

A number of diffraction patterns were inscribed into the bulk volume of glass samples with a variety of periods. Figure 4-3 shows a set of patterns written in such a glass substrate. The substrates used were made of pure fused silica supplied by Ibsen Photonics. The samples had dimensions of

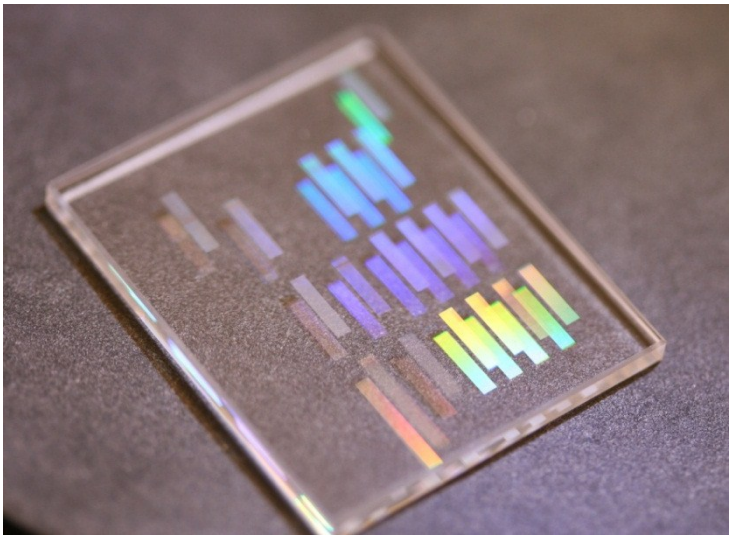

Figure 4-3 Image of a series of femtosecond written phase mask patterns.

30x25x2 mm and were chosen for the flatness and optical quality of the UV grade fused silica. The uniformity of the substrate was found to be critical in the reproducibility of the masks. This glass was known to be highly transmissive in the wavelength region from 193nm to 693nm as shown in Figure 4-4 below [**105**], which is a fundamental requirement for the use of these masks in the production of FBG as it allows for thermal stability as the absorption of the incident laser light is barely absorbed. In order to exploit the photosensitive nature of the optical fibres for Bragg grating

inscription, the fibres are illuminated typically at laser wavelengths in the UV or near UV.

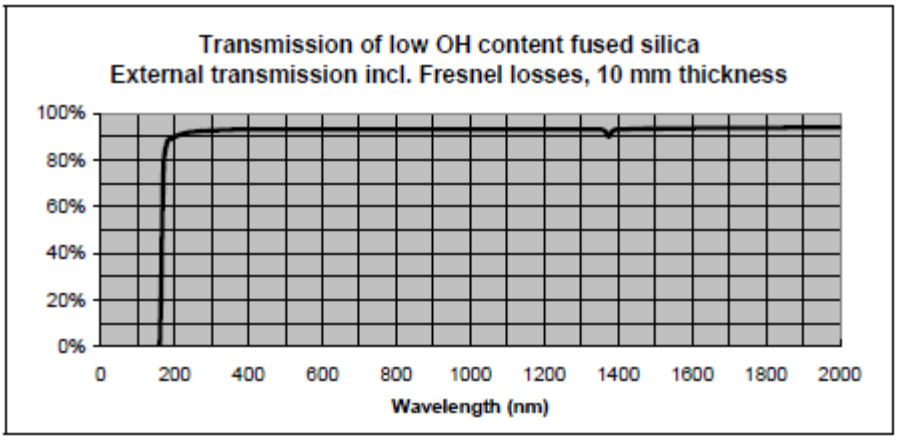

Figure 4-4 Transmission spectra of the low OH content fused silica supplied for the fabrication of phase and amplitude mask structures. Spectra from Ibsen Photonics.

The laser used to write the patterns in the silica substrates was an Amplitude Systemes s-pulse HP laser that produces sub 500fs pulses at a wavelength of 1026nm and average powers of 550mW. The laser system consists of four air bearing stages mounted on a large granite bed for stability which was crucial for the stability required to allow the stage resolution and repeatability to be fully utilised. The system incorporates on the move optical power control and a vision system for high accuracy alignment. The motion control system is based on Aerotech ABL 1000 air bearing stages. These are controlled by a dedicated A3200 Aerotech control unit, from which the stages are controlled by the G-code used for CNC programming of the motion. The repeatability and precision of these stages allows this work to be carried out with minimal stitch errors and with the

accuracy required to obtain the precise lines written in the fused silica substrates. The high precision multi-axis high resolution air bearing stages have the sub-μm alignment accuracy critical for writing these structures especially required for work with the 1st order mask inscription.

The pure fused silica samples were mounted on the multi-axis stages using a specially designed jig that securely clamps the sample on all sides both top and bottom whilst not creating significant stress or warping the substrate. The sample was also secured such that it was perpendicular to the incident femtosecond beam. Low stress mounting of the samples was critical as the inscription mechanism is based on non-linear absorption of the focused femtosecond laser light; hence it is important to avoid unwanted effects from non-linear interactions that would change the uniformity of the written structure that is dependent on the direction of the inscription. The inscription laser polarization was chosen to be circular, in this way the dependence on the relation between write direction and polarization state was thought to be largely negated. Although not truly optimized it enables the total write process to be partially optimized no matter the direction of stage travel. This also enables the total write time to be kept shorter as there is no optimization based on the direction of the sample, travel or polarization state that would otherwise take additional write time.

The inscription lens used was a Mitutoyo x100 NIR lens. This was chosen as it provides a long working distance with a high NA thus generating a

small and highly accurate focal spot that the structures written required. The accurate nature of the spot through the sample due to the large NA and working distance are critical to the direct write nature of the work. The effect or the refractive index mismatch, lens to air to substrate, on the focal position was considered to result in a minor offset in z for the material and considered to be negligible during planning.

The air bearing stage system was controlled through programming in G-code. The coding was written to enable flexible motion control producing typically mask patterns of 5x1mm at a range of depths and pitches. The depth of the written structures varied from the surface to a depth of 150 μm. This was carefully controlled using a piezo lift stage after having identified the position of the substrate top surface. The row R1 was written at the surface, R2 at a depth of 75 μm, R3 at 100 μm and R4 at 150 μm. The pitch of the masks was chosen to be 1060nm, 2120nm and 3180nm. Columns C1-C4 represents different written periods as described in the figure below. This was with the aim of the masks being used to write 1st, 2nd and 3rd order gratings at the C-band wavelength range for use with SMF-28 fibre. On the substrate described here a set of 18 mask patterns were written with the periods and energy levels as shown in the table below. The second set of mask patterns, shown below the dotted line in the figure below, were written in order to investigate the effect of energy levels on the inscription process and subsequent grating quality. The energies used range from 1 μJ to 8 μJ; the energies were measured at the objective lens

and were varied by the use of an external attenuator unit in the system. The parameter for the energy per pulse is shown as Epp in the table below.

	C1	C2	C3	C4
R1	Λ=1060nm Epp=4μJ		Λ=2120nm Epp=4μJ	Λ=3180nm Epp=4μJ
R2		Λ=1060nm Epp=4μJ	Λ=2120nm Epp=4μJ	Λ=3180nm Epp=4μJ
R3		Λ=1060nm Epp=4μJ	Λ=2120nm Epp=4μJ	Λ=3180nm Epp=4μJ
R4		Λ=1060nm Epp=4μJ	Λ=2120nm Epp=4μJ	Λ=3180nm Epp=4μJ
R5		Λ=2120nm Epp=1μJ	Λ=2120nm Epp=2μJ	Λ=2120nm Epp=4μJ
R6		Λ=2120nm Epp=6μJ	Λ=2120nm Epp=8μJ	Λ4000nm Epp=4μJ

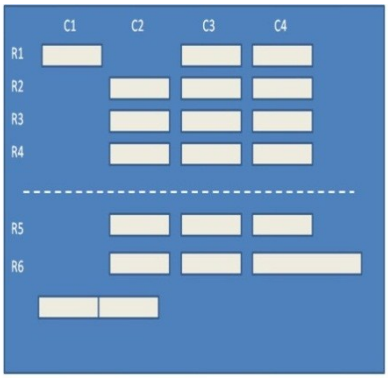

Table 4-1 (a) Table showing the inscription parameters used in production of the phase masks (b) schematic of the substrate

The laser was set to operate at 100 kHz repetition rate then optimized for beam quality, stability and pointing. This was experimentally found to be the optimum repetition rate producing the most well-defined and smooth lines whilst keeping the overall write time low. A laser energy of 4μJ was found to produce reliable and clear lines for which the inscription process was found to produce the most consistent results.

As with the power levels and repetition rate the translation speed of the stages was optimized. It was found that 1mm/s gave the best results in

terms of pattern quality. The code was adjusted such that the raster (the rectangular formation of a series of parallel scanning lines) function written allowed the stages to operate accurately with negligible error based on positional error originating from the acceleration and deceleration of the stages. This was optimized and the stages tuned to give the accuracy required for the pitch and line quality required to produce the masks. The stage speed was also adjusted as to avoid any issues with overwriting and also to adjust the overall write time.

The nature of the line by line inscription allows for the specific design parameters to be optimized quickly and adapted meeting any specific requirements. Although the majority of the masks made have been optimized for use in the telecoms C-band with silica optical fibre other masks have been produced that were optimized for use with polymer planar and fibre samples. These have been designed to work at different wavelengths, both of the laser illumination and of the grating produced, to be appropriate for the transmission spectra of polymer fibres. This is a simple example of the ease of adaptation; more complex structures can also be produced via adjusting the coding and parameter space used. This flexibility is one of the key advantages of this process and has the potential to give a broad range of masks dependent only on the optimization and parameter space of the inscription.

The nature of these masks, being written inside the substrate, also provides other advantages over the cleaning procedures of a standard commercially

available phase mask. Typically the regular cleaning of these masks involves the use of semiconductor grade acetone and clean room environments and at no point can contact with the mask be made, whilst the full cleaning process requires the use of sulphuric acid and is often carried out by sending the masks back to the supplier. In sharp contrast the cleaning of the masks produced here involves only the use of pure methanol or acetone and optical tissue to draw across the sample. This makes the running cost and handling of these masks much easier, more robust and significantly cheaper.

The total write time for producing a mask runs from between 2hrs 20 minutes, to at its maximum, a time of 3hrs. This is the time taken to produce masks of 5x1mm and the difference reflects the increased number of lines of inscription for masks of a shorter pitch length. These write times may well be shortened with some changes to the inscription procedure through further optimization of the air-bearing stage coding. The time taken to adapt the pitch, power, dimensions and other parameters is negligible as this has been built into the code so that it can easily be varied. More complex desired masks such as phase shifted and chirped both of which have been written using the same techniques. The ease of variability and speed of production exceeds that of the commercially available masks which are often multi-step process production lines that are less easily adapted.

4.2.3.2 Characterization of masks

The masks were characterized in two different ways (a) by using the diffraction of a helium neon laser and by (b) by using a transmission microscope that incorporated a QPm measurement. The reason for using both approaches is to check the measured parameters against each other and to be certain that the Talbot effect is not giving false readings (this will be discussed later in the chapter).

The light transmitted through the masks was measured using both a helium neon laser and a CW ultraviolet laser operating at 244nm. The transmission measurements with the HeNe laser showed no dependence on the mask pitch or the inscription femtosecond laser energy. However, the transmission of the UV laser through the masks changed, showing a decline in transmitted power for masks written with increasing femtosecond inscription pulse energies, varied from 2 to 4 to 8μJ.

By measuring the angle of diffraction for the different diffracted mask orders it was possible to confirm the period of the mask. Table 4-2 shows the diffraction angles of the orders measured and the phase mask periods calculated using the standard diffraction equation: $m\lambda = d\sin\theta$, where m is the diffraction order, λ is the wavelength of the incident light; d is the grating period and θ is the diffraction angle. Both patterns were fabricated using pulse energy of 4μJ. From these results it can be seen that there is good agreement with the programmed grating periods and the values calculated from the measured diffraction angle. The majority of the

diffracted energy lies in the zeroth order with the higher orders having diffraction efficiencies that vary between 1 and 5%.

Set mask period – 4μm		
Order	Diffraction angle (°)	Calculated period
+3	29.2	3.89
+2	18.35	4.02
+1	9.29	3.92
-1	9.54	3.82
-2	18.82	3.92
-3	29.61	3.93
Average period from measurements: 3.923μm		

Set mask period – 2μm		
Order	Diffraction angle (°)	Calculated period
+2	34.2	2.25
+1	18.8	1.96
-1	18.8	1.96
-2	34.3	2.25
Average period from measurements: 2.104μm		

Table 4-2 Measurements of diffraction angle

Using a transmission microscope the structure of the masks could be clearly seen and measured. Figure 4-5 shows the written mask structure as seen when viewed with a Zeiss Axiomicroscope using a x100, 1.4 NA oil immersion DIC lens. The pattern was designed to have a period of 1060nm pitch and this is shown to be approximately the case (errors in the measurement based upon judging the edge of the written structure make it difficult to get an exact measurement). This pattern was written at a depth of 75μm at 1mm/s translation velocity (in the vertical plane); with 4μJ per pulse at a repetition rate of 100 kHz. The plot next to the figure shows the measurement of relative phase change across part of the written structure. This was processed using the Quantitative Phase-amplitude Microscopy (QPm) version 2.0 IATIA LTd, Australia software [67]. This relies on phase

contrast techniques to separate and quantify the relationship of phase and intensity of the image. The algorithm used in the software allows phase maps to be calculated from images captured from standard bright field microscopy. The technique allows calculation of relative phase change (radians) which is dependent on the phase change created by the refractive index change and volume as compared to the surrounding media. Here it is used to demonstrate the clear phase contrast between the written structures and the unwritten areas. The peaks represent the inscribed structures as having a positive index change.

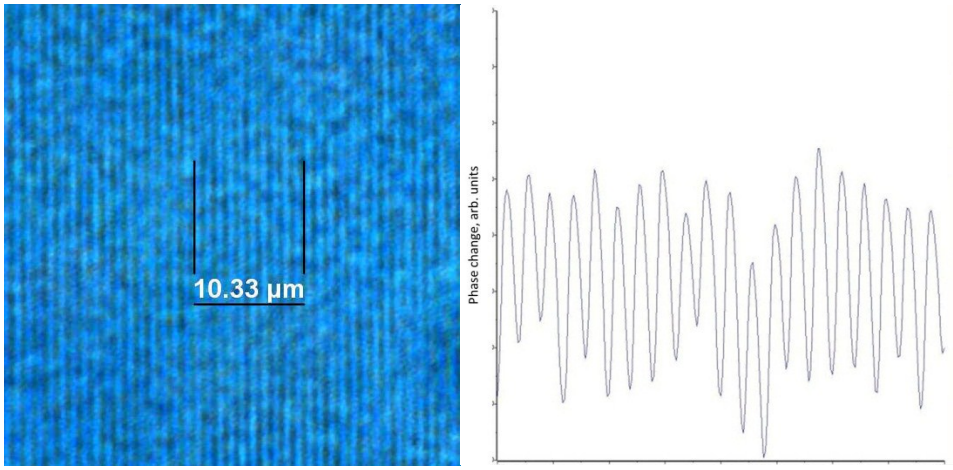

Figure 4-5 (a) Microscope image of the area C2 R2. The image shows the lines of inscription written with the laser (b) Phase map of 2nd order mask taken over a length of 20 µm.

Figure 4-6 (a) shows a phase mask written at a pitch of 2120nm at a depth of 75µm with pulse energy of 6µJ per pulse at 1mm/s translation speed and at 100 kHz repetition rate. Figure 4-6 (b) next to it shows that over the same distance measured there are half the number of written structures in the

same distance, as compared to Figure 4-5 (b), leading to the creation of a 4th order phase mask.

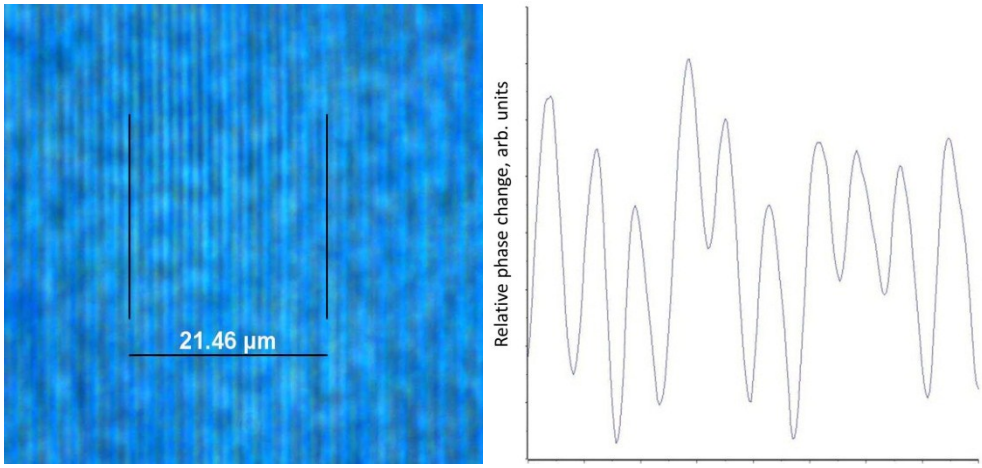

Figure 4-6 (a) Microscope image of the area C2 R6. The image shows the lines of inscription written with the laser (b) Phase map of 4th order mask taken over a length of 20 µm.

4.2.3.3 Profiling results for the phase masks

The white light profiling unit was applied to the phase mask structures and some of the results are shown below. Figure 4-7 shows a mask that was inscribed at depth. This explains the lower average height of the mask structure. The results show clear line structures with good apparent etch depth. Of course this is an inscription so the profile is being determined by the index change rather than the removal of material. It does show that there is a small amount of variation along each line. This would be due to the inscription being done with only one pass. It would be of interest to see how the increased number of passes would, as expected, improve the variation seen.

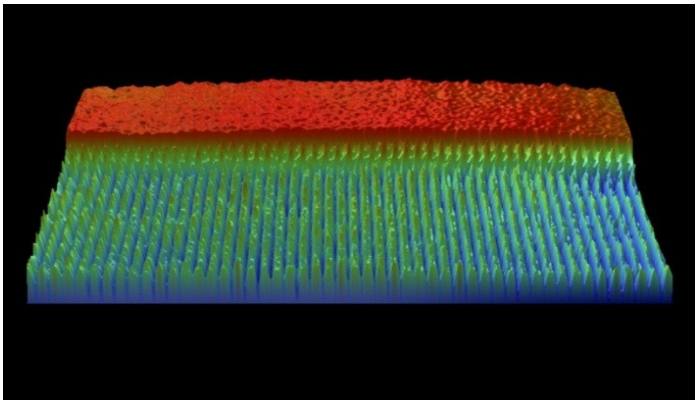

Figure 4-7 A 3D plot of phase mask C4R1 showing the variation in intensity when scanned with a profiler with 40x magnification. Profiling done by Charalambos Koutsides, processed by me.

The results of the same profiling scans profile was taken and is shown in figure 4-8. This shows the periodic variation expected from such features with apparent etch depths of approximately 12µm. The variation in height across the sample should not be over stated as it is likely a feature of the measurement, a result of angled samples at measurement due to samples having a highly reflective top surface, rather more than the sample varying in inscription height.

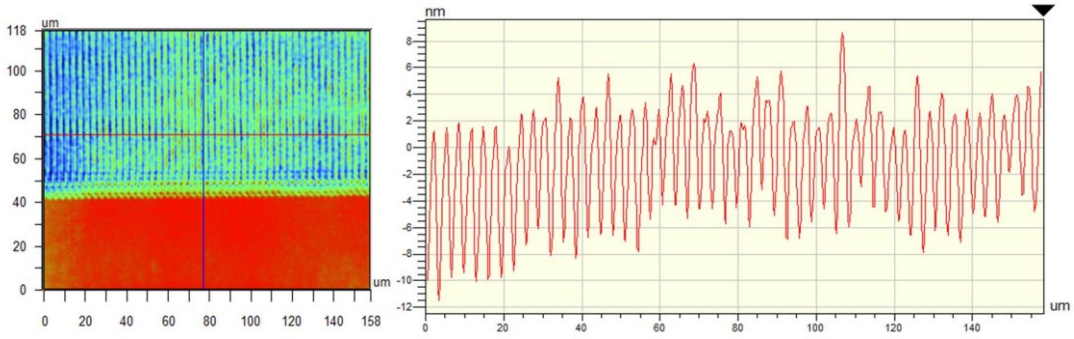

Figure 4-8 Shows the profile of the same phase mask. Profiling done by Charalambos Koutsides, processed by me.

4.2.4 Fabrication of fibre Bragg gratings

Fibre Bragg gratings were fabricated using all of the masks produced, with varying degrees of success, in hydrogen loaded photosensitive fibre. The laser used to write the FBGs was a Coherent SabreFRED laser which operates CW at a wavelength of 244nm. The system was set up in a conventional manner with the fibre located immediately behind the mask. In this case there was little concern as to whether the fibre came into contact with the mask, which would certainly not be the case with a far more delicate, conventionally produced mask. The laser power was set to 100mW which resulted in approximately 80mW being incident on the fibre. It was possible to fabricate gratings with all inscribed mask structures in the first set of patterns. However, the mask that had a period of 1060nm, inscribed using 4uJ pulses produced the highest quality gratings. Typically gratings with 30dB transmission losses were observed after six consecutive 5mm scans at a velocity of 0.1mm/s. The bandwidth of the 5mm gratings were about 0.18nm and the sidelobes were reasonable symmetrical. There was not a great deal of difference observable between the gratings made with the patterns at different depths.

Figure 4-9 (a) shows a microscope image of a grating created in photosensitive fibre from a mask of 1060 nm at a depth of 100µm depth. Also shown (Figure 4-9(b)) is the transmission profile of a 2nd order grating made with six consecutive scans of the this mask each at 0.1mm/s, the mask was written at a depth of 75 µm with a period of 1060nm at an

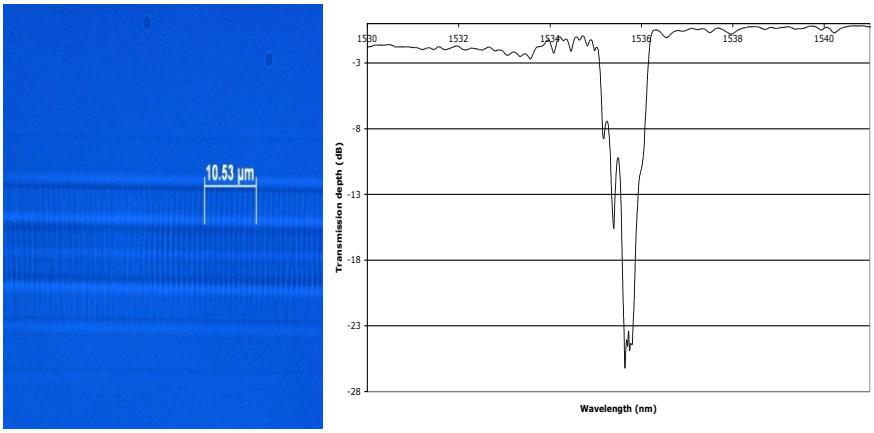

Figure 4-9 (a) Microscope image of grating written with 1060nm pitch mask (b) corresponding spectra profile of the grating. Grating spectra recorded by Dr Kate Sugden.

energy of 4 µJ per pulse. This grating reached a maximum transmission depth of 25dB. Strong sidelobes can be seen on the short wavelength side this was attributed to the grating not being apodized.

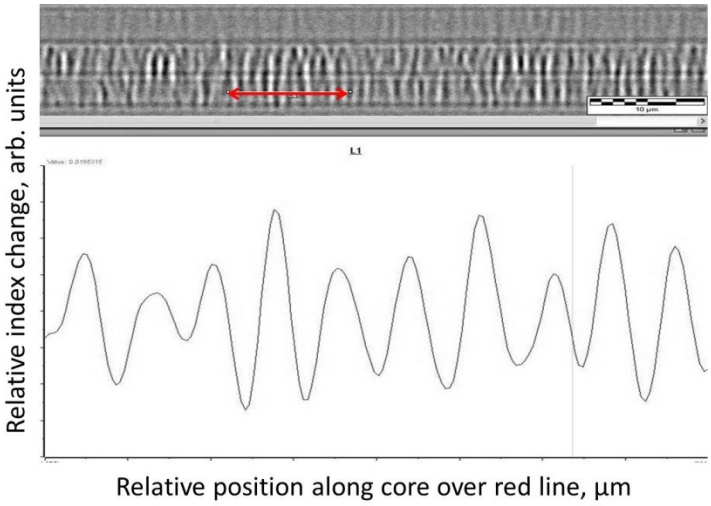

Figure 4-10 A QPm Phase contrast map along the grating structure that had been written in the photosensitive fibre.

The results demonstrate the nature of the phase contrast profile inscribed when illuminated using the inscribed mask. They show that the feature has an inscribed period of 1.06µm and is as such a 2nd order grating in the 1550nm band.

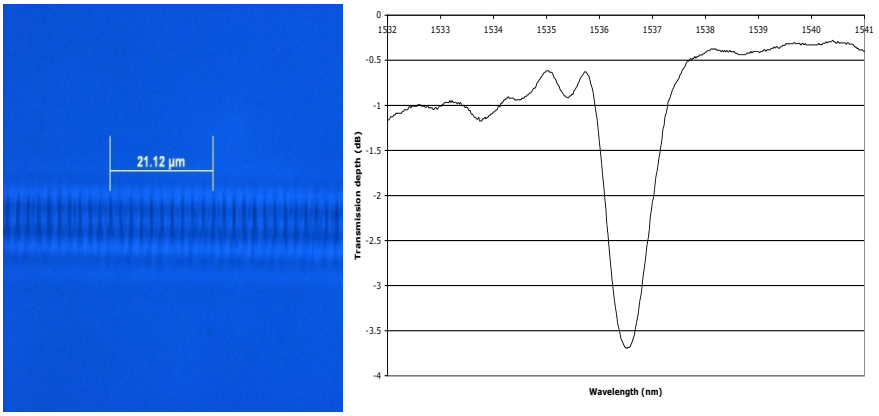

Figure 4-11 (a) Microscope image of grating written with a 2120nm pitch mask (b) corresponding spectra profile of the grating. Grating Spectra recorded by Dr Kate Sugden.

Figure 4-11 (a). Shows a microscope image of a grating in the core of some photosensitive fibre produced using a mask written at 75µm depth at 2120 nm pitch. As before the grating was made using a scanning UV beam with an incident power of 85mW at 244nm in hydrogen loaded photosensitive fibre. The 4th order grating was fabricated with seven consecutive scans of the fibre each at 0.1mm/s. Figure 4-11 (b) shows the transmission profile of the grating which reached a maximum transmission loss of 3.7dB.

4.2.5 Discussion of the Talbot Effect

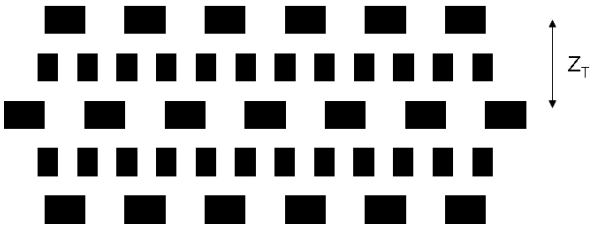

Figure 4-12 A schematic showing the definition of the Talbot length, Z_T, used. In this definition it is taken to be the distance between two planes of the same period although the phase is different.

The interpretation of the microscopic images requires a certain amount of care because of the Talbot effect, which is illustrated in Figure 4-12. This is a near field diffraction effect seen when a plane wave passes through a periodic structure. It causes the resulting wavefront to be replicated periodic at a separation Z_T given by:

$$Z_T = \frac{a^2}{\lambda} \qquad \text{Equation 4-7}$$

where a, is the period of the grating (out of phase spacing) and λ is the wavelength of incident light.

Furthermore a second pattern is generated halfway between these locations that has half the spatial period of the original structure making it appear as if you have written a structure with double the frequency. Further higher frequency patterns are also generated between these points. This is illustrated by Figure 4-13 where two different microscope images of the same 4 micron pattern are seen where the sample has been translated, in direction of focus Z, by 6 microns between the two images.

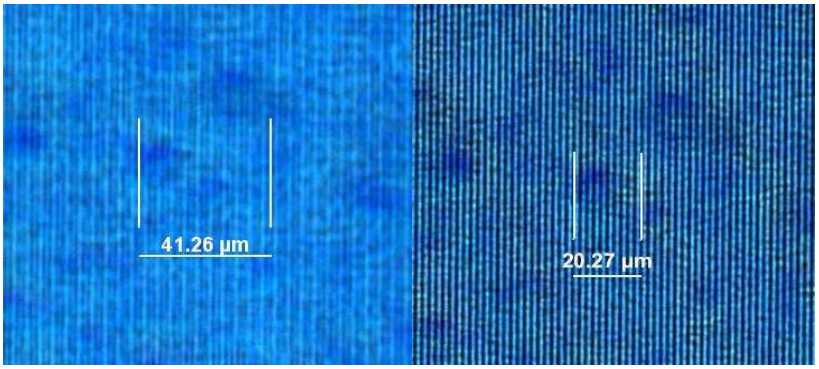

Figure 4-13 (a) A microscope image of the 4µm period mask (b) microscope image of double the frequency of the same 4µm mask

Assuming a 500nm illumination of the mask the Talbot distances for the 1.06 µm, 2.12 µm, 3.18µm are 2.25 µm, 8.99 µm and 20.2 µm respectively. For the short period structures this effect tends to add noise to the measurements however with the larger periods the higher frequency images can be clearly seen. Consequently, it is important to cross check the periods measured with the microscope with measurements of diffraction angles for an incident laser beam.

4.2.6 Zeroth order considerations

With regard to the inscription of the Bragg gratings using the femtosecond inscribed masks, one needs to consider the effect that the zeroth-order has on any interference pattern that is generated by the mask. This is essentially three-beam interference that results between the non-zero suppression of the zeroth-order with the different diffracted order pairs. Higher order contributions are ignored as they can be minimized by increasing the spacing between the fibre and the mask. The effect of a significant zeroth order contribution on FBG inscription using a phase mask has been

analysed by Dyer et al [**106**] and by Xiong et al [**107**]. Using the aforementioned mathematical descriptions an indication of the characteristics of the field distribution can be seen. Consider, for the sake of clarity, the interference effects between the ±1 orders and the zeroth order, for which the intensity distribution is given by;

$$I_{0,\pm1} = 4\left[C_1^2 cos^2\left(\frac{2\pi x}{\Lambda_{pm}}\right) + C_0^2 + 2C_0C_1\, cos\left(\frac{2\pi x}{\Lambda_{pm}}\right) * cos\left(\frac{2\pi z\left(1-\sqrt{1-(\lambda_{UV}/\Lambda_{pm})^2}\right)}{\lambda_{UV}}\right)\right] \quad \text{Equation 4-8}$$

Where C_0 is the amplitude of the electric field of the zeroth order, C_1 for the first order diffraction, and λ_{UV} the UV inscription wavelength. When there is no power in the zeroth order the intensity distribution arises from the first term, being oscillatory in the x-direction with a spatial period of half the phase mask and without variation on the z-axis. The second term is constant and associated with the non-zero contribution of the zeroth order, reducing the fringe contrast of the first term. The third term indicates the interaction between the zeroth and first orders beams that has contribution along the x- and z-axes, with a period Λ_z, given by

$$\Lambda_z = \frac{\lambda_{UV}}{1-\sqrt{1-(\lambda_{UV}/\Lambda_{pm})^2}} \quad \text{Equation 4-9}$$

This equation is equivalent to $2Z_T$, as defined above, and gives the same result for the Talbot distance, given the inscription laser wavelength and mask period. The effect of the non-zero zeroth-order on the interference fringes of the Bragg grating is shown in Figure 4-14. The figure clearly

shows how the presence of the zeroth order modifies the expected fringe pattern producing a spacing equal to the mask period, which in turn leads to the observed, strong, second-order Bragg gratings.

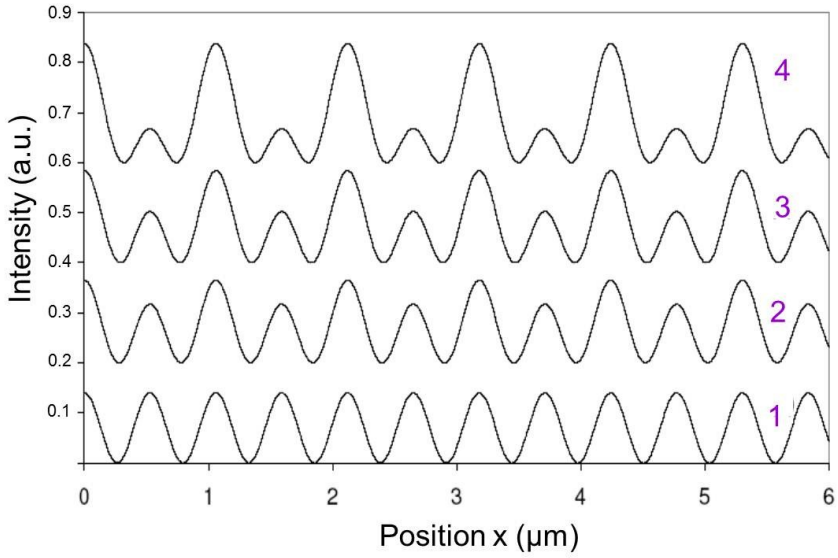

Figure 4-14 Intensity distribution along the x-axis at z = 0 for different contributions of the zeroth-order. (1) 0%, (2) 1%, (3) 3% and (4) 13%.

4.2.7 Chirped, Fan and complex phase masks

In the course of writing phase masks in different parameter spaces the decision was taken to explore the potential of the technique to provide complex and advanced phase mask structures. These were tested and had varying degrees of success but are included as proof of concept.

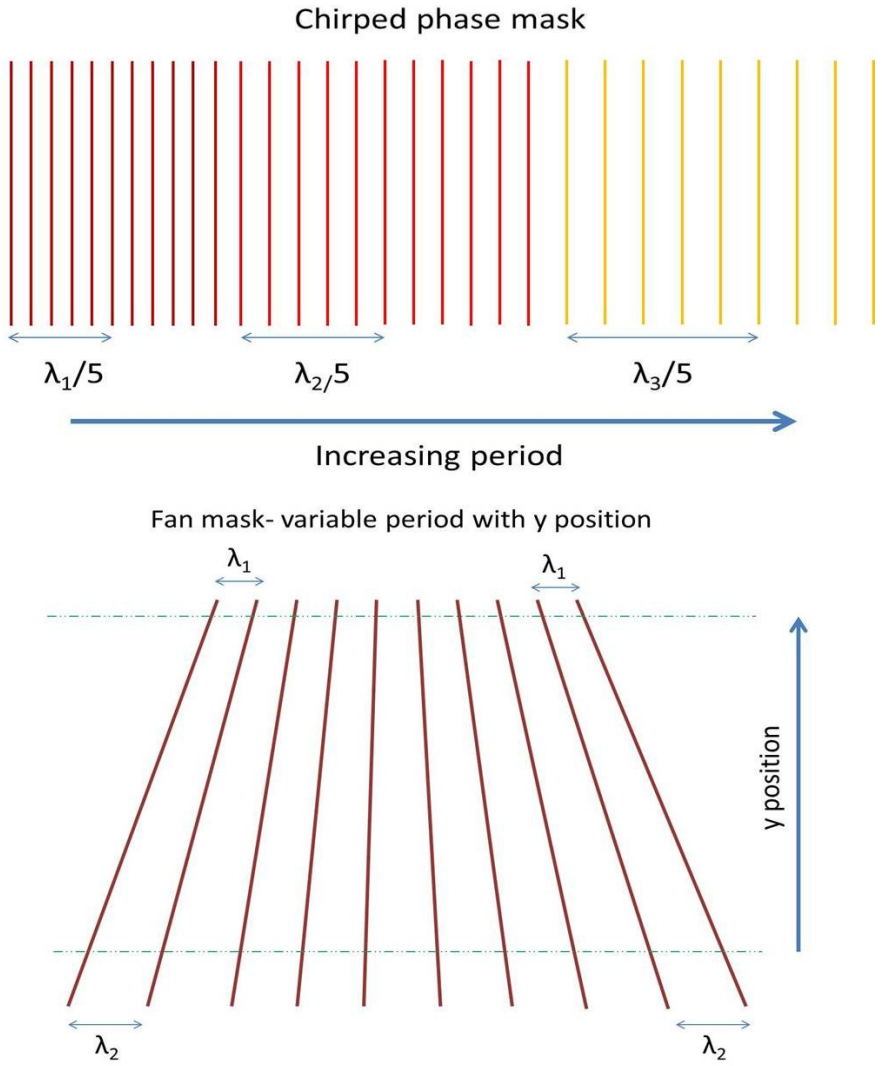

Figure 4-15 Schematics of the chirped and fan phase masks showing the change in period seen by incident UV light as a function of either parallel or perpendicular distance to the fibre axis. The fan mask uses inscription height on the mask to create the variable pitch.

4.2.7.1 Chirped phase masks

Typically to achieve a chirped grating the mask written has a period that changes across the full mask length. When a UV beam is then scanned the resultant period inscribed in the grating varies across the fibre length. To achieve this using femtosecond inscription the period of inscription was varied in sequential steps by looping the G-code used and adding an increment to the period every set length. When these masks were used to make FBG in smf28 the resultant grating showed some degree of chirp, however, the effect was not as great as it would be expected to be. This is thought to be because of some of the issues mentioned above with the lack of suppression of the zeroth order from the etch depth not having been fully optimised.

4.2.7.2 Fan phase masks

Figure 4-15 shows the shape inscribed with this mask. The thought process was that at each height the fibre was at the mask would produce a different wavelength FBG. This would allow the production of one mask to manufacture a range of gratings, which in turn would reduce the cost of buying several slightly different grating period masks to write gratings at a different wavelength. The fan mask when tested was found to have limited degree of wavelength range. This is thought to have been due to a combination of factors. Firstly the gratings inscribed are not optimised and are as such a little broader than optimal, thus the change in FBG inscribed would be less visible. Second the angular variation was not large enough as it was aimed to keep the writing time reasonable as a trial run and thus was not very high and so did not cover a large range of mask periods.

4.2.7.3 Phase shifted phase masks

The technique of adding a phase shift mid mask was attempted and was achieved in inscription. However, because of the lack of 0^{th} order suppression it is expected that the individual grating sets, and hence the phase shift, were less defined and thus the effect was washed out and the expected resultant effect was not fully observed.

The complexity available would appear to be there, but work should be carried out to refine the key parameter issues such as etch depth before too much effort is direct towards these avenues in the future work.

4.2.8 Conclusions

In summary the work presented is, to the best of my knowledge, the first example of femtosecond inscription/ablation of masks used to produce 1^{st}, 2^{nd} and 3^{rd} order and more complex grating structures fibre Bragg gratings (FBGs) in SMF-28. The work demonstrates the proof of concept and flexibility for the use of femtosecond lasers to make complex and reproducible masks. This approach to fabricating masks enables the patterns to be below the surface which is helpful in the protection of the tooling and reproducibility of gratings due to positioning variations.

One does need to account for the effect of the non-zero contribution of the strong zeroth-order component that is present in the transmission characteristics of the mask and that modifies the ideal, anticipated interference pattern typically used for Bragg grating inscription. Hence when using the femtosecond inscribed masks for Bragg grating inscription we are inscribing second order Bragg gratings instead of a conventional

first order Bragg grating. This is not in itself a major drawback, but pertains from the fact that we have yet to control the effective laser induced "etch-depth" of the mask and its relation to the UV wavelength used for the Bragg grating inscription. This is under development and we anticipate far greater diffraction efficiencies once this issue has been resolved.

Through subsequent work I believe the main improvements that would be considered are in trying to make the write process more consistent. Some of these are relatively simple in hindsight to implement for example keeping the write direction consistent. Although this would increase the time for production it would negate any possible effect of directionality from pulse phase front interaction with the material structure for instance. Another simple possibility is to over-write the structures. This has been shown to improve results in fused silica when using low repetition lasers [**108**]. To control the etch depth one would have to first achieve a highly uniform index change, then consider the potential of using beam shaping in the form of slits [**38**], spatial light modulators [**109**,**110**] and oil immersion objectives to correct for aberrations and defocusing caused by refractive index mismatch. I would also consider reducing the power and thus the translation speed and perhaps frequency conversion to the UV to attempt to gain a more even index profile. I expect this would all contribute to give improved higher diffraction efficiencies and help to suppress the 0^{th} order.

It should be noted that although this study has focused on the 1D phase mask production work has been done to produce 2D masks that have

applications in a range of fields including the creation of photonic bandgap structures and structures for surface plasmon resonance devices.

4.3 Femtosecond laser micro-inscription of Optical Coherence Tomography phantom resolution test artefacts

The work in this section was carried out in collaboration with Dr Peter Wooliams and Dr Peter Tomlins who were at the National Physical Laboratories and Jana Rasakanthan and Dr Kate Sugden of Aston University. The inscription and coding was carried out by myself, the device was designed and characterisation with Peter and Peter with Jana contributing to the characterisation.

4.3.1 Introduction to OCT

Optical Coherence Tomography (OCT) is a method of optical signal acquisition and processing based upon interferometric techniques. This relies upon scattering within the media of interest to produce micrometer resolution 3D images. Typical systems work in the NIR to allow for greater sample penetration depths within the scattering media and are increasingly being applied to conservation, diagnostic and interventional medicine facilitating detailed imaging at depths of several mm without sample preparation or the use of ionizing radiation, required in ultrasound and MRI scans. It has gained acceptance as a non-invasive method for characterizing soft tissue and other turbid media [**111**] demonstrating morphological tissue imaging at depths that confocal microscopy cannot

achieve due to the decreased penetration depth of the technique. It has widely been explored for use as a diagnostic tool in clinical medicine, with commercial devices now available in ophthalmology [**112**], dermatology and interventional cardiology [**113**].

As a consequence of the OCT systems becoming more commonly used in worldwide biomedical imaging a reliable method of characterizing their performance and validating their operation is required to enable non-expert end-users to robustly test and characterize commercial and laboratory instruments in the field. Moreover, European regulations for medical devices are quality system based [**114**]. Hence, established calibration methods for key instrument parameters can ease the regulatory process [**115**]. This approach has previously been observed in now established fields of medical imaging [**116**] and is expected to be an important for the widespread adoption of OCT for routine procedures.

This section of the chapter describes the use of femtosecond laser subsurface micro-inscription techniques to fabricate an OCT phantom test artefact for validating the resolution performance of a commercial OCT system. The key advantage of this approach is that by utilizing the nonlinear absorption a three dimensional grid of highly localized point and line defects can be written in clear fused silica substrates.

4.3.2 An overview of how OCT works

OCT is based on low coherence interferometry. The interference length achieved in OCT is much shorter than in standard uses of a Michelson

interferometer. This is attained by the use of broadband light sources resulting in interference lengths of the order of microns. As in standard interferometry light is split into two arms, a reference and sample arm, with the sample of interest placed in the latter. When the reflections of the two paths are recombined they generate interference patterns. This only occurs if the difference in path length is less than the coherence length. By scanning the reference arm mirror back and forth, i.e. longitudinally in time (in the Z axis as shown in Figure 4-16 as done in time domain OCT, an area of interest may be scanned. The cross-correlation of the level of interference relates to the amount of back scatter from a sample, typically due to changes of refractive index, and with the short coherence length this combines to give localised information about the amount of scatter from a sample of interest. Thus by monitoring the signal a vertical scan may be performed. This is known as an A-scan. By adding a galvo-mirror one can then scan in perpendicular directions. If scanning is implemented in one orthogonal (X or Y in Figure 4-16 below) direction the recorded information produces a plane of information, and when combined with a second scanning motion a 3D block of information can be achieved. These are known as B-Scans and C-Scans respectively. There are a range of other different techniques including frequency domain, Fourier domain and time encoded frequency domain OCT. They all have different advantages and drawbacks but the fundamental principle of examining the cross-correlation from the interferometric arrangement to gain spatial insight of a sample is common to all. The focus of this work is to begin to standardise and consistently quantify an OCT systems ability to resolve spatial

information about scattering points within a media of interest by creating a repeatable test artefact at the limits of standard commercial OCT capabilities.

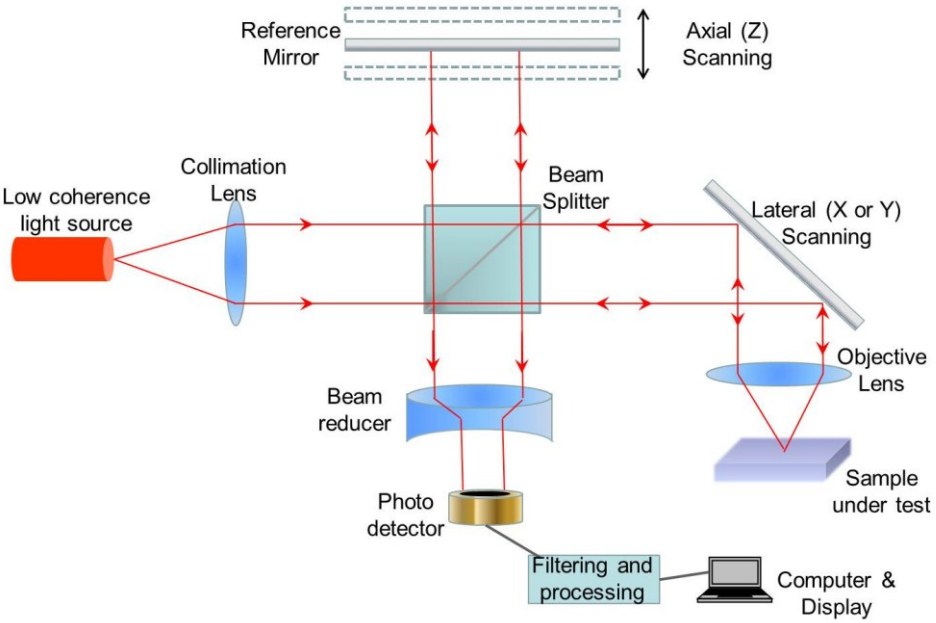

Figure 4-16 A schematic of an OCT system showing the basic layout commonly used.

4.3.3 How femtosecond improves the artefacts

A review of the types of artefacts used to date for characterizing and standardizing optical imaging instruments is given by Pogue et al [**117**]. A conventional metric for OCT characterization is the resolution, often defined as the full-width at half-maximum (FWHM) of the system point-spread function (PSF) in axial and lateral dimensions [**118**]. Murali et al. [**119**] have disputed this definition, showing that it is insensitive to optical

aberrations incurred in high numerical aperture OCT. Detailed measurements of OCT PSFs have previously been obtained by imaging scattering medium [11], nano-shells suspended in an aqua solution [**116**,**118**] and particles dispersed within a transparent matrix [**111**,**118**]. This last method has been demonstrated in both Fourier [**120**] and time domain [**116**] OCT. Both Ralston [**121**] and Woolliams et al. [**122**] have then used these measurements to remove the influence of the instrument function from OCT B-scan images.

The formation of PSF artefacts or phantoms by mixing sub-micrometer particles into a matrix material presents a number of challenges. Firstly, small particles have a low back-scattering cross-section and consequently can manifest as a barely detectable signal in the OCT image. Furthermore, prevention of particle clumping is essential for valid PSF measurements. Processing of the data is complicated by random particle placement associated with the mixing process. Whilst these particle based phantoms have proved to be a useful tool for OCT characterization a new approach is required for them to be more amenable to users and suppliers of OCT equipment. An optimal design would precisely position PSF targets in predetermined locations within the artefacts.

Here the nature of femtosecond direct-write allows production of a point spread function phantom artefact introducing micron scale defects within a polished fused silica substrate. This manufacturing process provides the necessary control to accurately position the defect position. Furthermore, this method may be fully automated to produce highly repeatable artefacts.

The primary advantage of using femtosecond lasers in this work is the ability to interact with materials only at the focal point of the laser beam due to the non-linear interaction mechanisms. Thus the potential to write devices with a range of complexities in 3D within a substrate has great potential for the manufacture of OCT phantoms. Hence, the purpose of this study was to evaluate femtosecond inscription as a candidate technology for producing OCT resolution artefacts.

4.3.4 Materials and Methods for initial samples

The samples worked with are pure fused silica substrates from Ibsen Photonics, Denmark. They were 30x25x2 mm in size and were written on the Aston micromachining system @ 1026nm and pulse duration of 450fs. The inscription lens was a Mitutoyo M Plan Apo NIR x100 lens having a numerical aperture of 0.50 and focal length f = 2 mm yielding a Rayleigh criterion focused spot size of ~2.5 μm.

The PSF artefact structure comprised a series of lines, written at different pulse energies as shown in Figure 4-17 in effect creating a parameter space scan. Individual lines of continuous refractive index change were written by translating the sample at a constant speed of 1mm/s under a fixed focus with a pulse repetition rate of 100 kHz. Under these conditions, individually inscribed point defects overlap to form a continuous line. The line pitch was set to 75 μm for both perpendicular axes, with the first line written at a depth of 75 μm from silica surface. The maximum laser power at the objective lens was 4.1 W (i.e. 41μJ per pulse and a peak pulse power of ~0.1GW). The inscription energy was set as a percentage of the

maximum. The percentages chosen were 100, 80, 60, 40, 20, 10, 5, 2.5, 1, 0.5 and 0.25% of the maximum laser energy giving a range of energies from 41-0.1025 μJ. Lines were written in pairs at each energy level, with 100% lines written to facilitate location in microscope and OCT images.

The initial samples written consist of a regular series of line defects written by translating the sample through the focus of the laser beam. The individual defects overlap to produce a long line defect. At a constant repetition rate of 100 kHz, different pulse energies and depths were used to see the effect on the defects and their visibility to the OCT. A grid of lines was written where the vertical rows of the sample had varying pulse energies, this allowed the variation of energy and depth to be examined. At one end of the lines the finish points were staggered to allow the lower levels to be imaged with the OCT and microscope without optical aberrations from other levels being introduced when viewed from above. The deepest lines were written first so that during the inscription the laser pulses were not affected by passing through previously written structures.

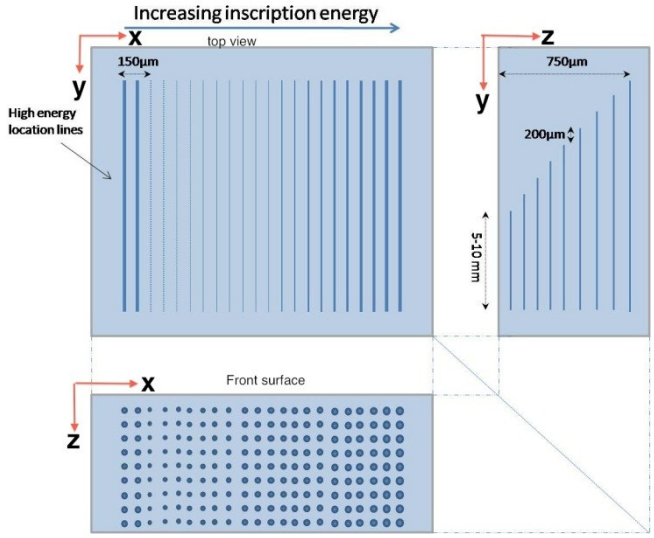

Figure 4-17 A schematic of the femtosecond inscribed OCT calibration artefact showing the paired lines of varying power increasing from left to right after initial location lines.

The artefact was first evaluated using an optical microscope (Axioskop 2, Carl Zeiss, Germany) and the size of the defects estimated for each of the power settings and the different depths by measuring the inscribed line widths. A 20x magnification imaging lens (Plan Neofluar 20x/0.50) was used to acquire microscope images of the sample. The artefact was also imaged using an OCT instrument (EX1301, Michelson Diagnostics, UK). This swept-source OCT system operates at a central wavelength of 1305 nm and has previously been measured to have a lateral resolution (FWHM) of 8.4 µm and axial resolution (FWHM) of 10.9 µm [**123**]. This instrument comprises four interferometric channels focused at different depths to obtain an extended depth of field. However, in the present analysis only results from a single channel are presented. To obtain an oversampled estimate of the average OCT response to each detected point, 40 B-scans

were combined. This averaging also smoothes out any granularity in the inscribed line. Corresponding points in each B-scan were aligned from the peak location of a two-dimension Gaussian fit to the raw linear intensity data. The oversampled data was interpolated onto a regular grid for visualization. Specular back-reflection from the artefact surface was avoided by mounting the sample with a 3.0 degree tilt relative to the incident OCT beam.

Following OCT analysis, the artefact was cleaved along the OCT B-scan plane and etched in hydrofluoric acid (40% initial concentration diluted 20:1 with distilled water) for 20 minutes. One half of the etched artefact was imaged with a confocal microscope (LEXT, Olympus). This was done to image the refractive index change profile to better understand the effect of shape on the reflection signal imaged with the use of OCT.

4.3.5 Initial results

The effect of varying the laser power on the width of the target line can be clearly seen in Figure 4-18a. Three pairs of lines are shown, in which the feature width broadens with increasing inscription power. The degree of broadening was determined using quantitative phase microscopy (QPm), from which the inscription was identified as a distinct phase modulation, demonstrated in Figure 4-18b.

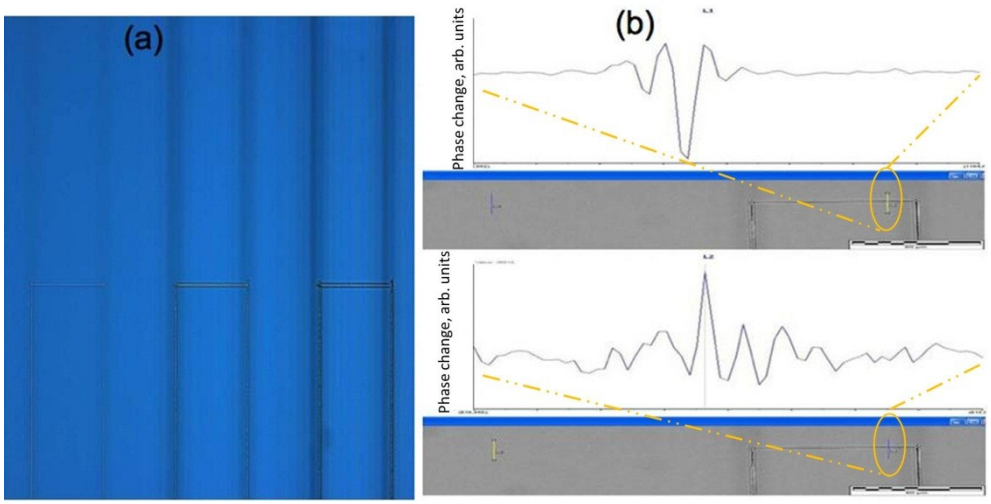

Figure 4-18 a) Microscope image of three pairs of lines showing a variation in the feature width with varying inscription power b) QPm measurements of two lines showing the contrast between above material threshold void creation (above) and below material threshold index change. The yellow line in the grey image marks the measurement area for relative phase plot.

Figure 4-19 shows the average widths of the lines in the upper layer at 75 µm from the surface as a function of laser power. Along any given line 6 measurements were taken and then averaged. The measured defects range from 0.5–7.6 µm in cross section, corresponding with power levels of 5–100%. The lines written at a power of <5% were found to be too close to the resolution of the microscope for accurate assessment of their size.

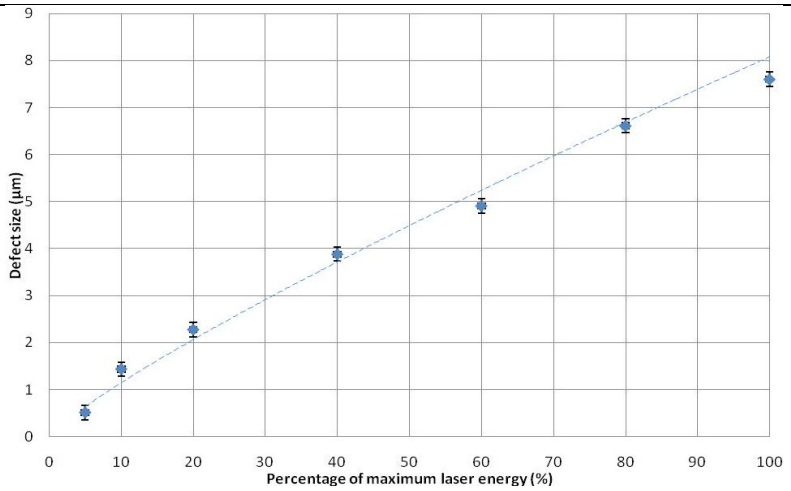

Figure 4-19 Variation of measured apparent defect size with laser power setting used taken at a depth 75 µm from the surface, as measured using an optical microscope. Measurements recorded by Jana Rasakanthan.

Figure 4-20 shows the OCT cross-section of the sample on a linear intensity scale. The strongest lines are at the far edges with the inscription power decreasing from the left hand side (columns 1–20). Columns 21 and 22 (far right) represent lines written at 100% power for identification. The focus of the OCT instrument corresponds approximately with lines written in row 2, where point visibility just extends to column 16, or 2.5% power.

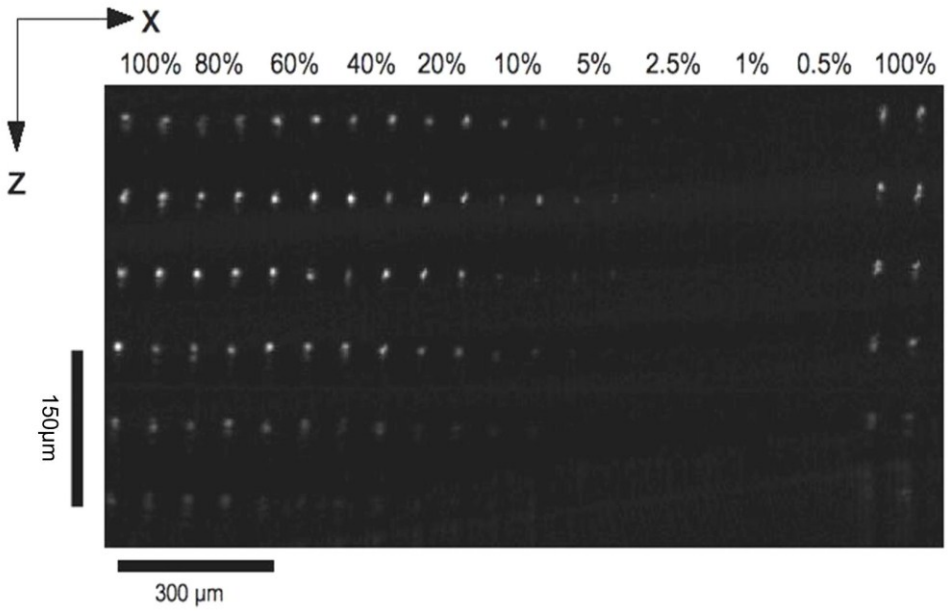

Figure 4-20 OCT cross-section of engraved sample, scaled in logarithmic intensity. Lateral and axial dimensions are denoted x and z respectively. Femtosecond inscription is denoted by the bright points. Rows and columns were written at 75µm intervals. At each depth, pairs of lines were written at laser powers varying from 0.5-100%. The OCT image has not been corrected for the silica substrate refractive index. Image captured and processed by Dr Wooliams, Dr Tomlins and Jana Rasakanthan.

The axial and lateral resolution was estimated from the FWHM of a two-dimensional Gaussian function fitted to each detected point in the OCT data. The results of these, averaged over 40 sequential B-scan slices, are shown in Figure 4-21 at depth of 75 µm. The measured axial FWHM is plotted as a function of inscription power and for different line depths of 75 corresponding with rows 1-6 respectively. At different depths similar trends were observed.

Figure 4-21 also shows axial and lateral measurements taken using a confocal microscope of the lines from the end face (etched surface) of the sample. The confocal lateral diameters here are smaller than shown in Figure 4-19; this is probably due to the higher contrast ratio of the etched sample making it easier to focus on the defect.

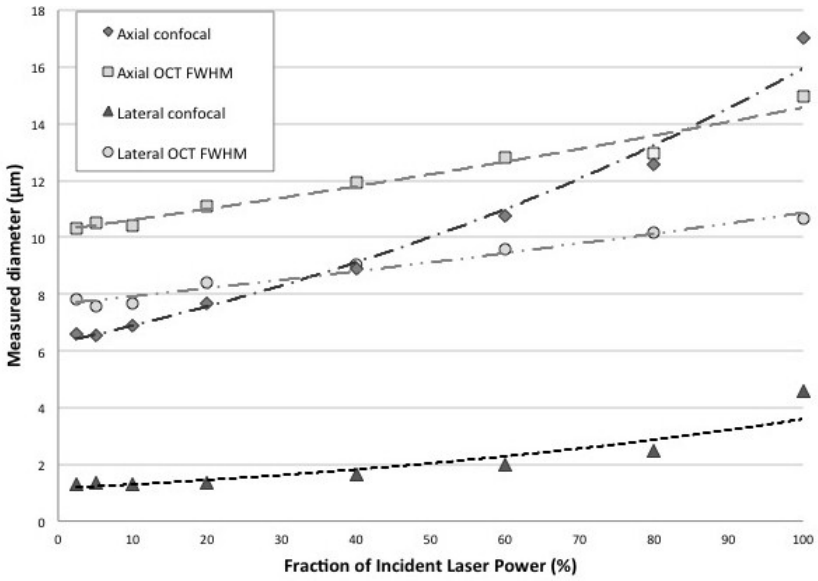

Figure 4-21 Plot of FWHM of axial PSF measured from laser inscribed artefact written at powers of 2.5, 5, 10, 20, 40, 60,80 and 100% of the maximum laser power and at a depth of 75 µm. Data processed by Dr Wooliams, Dr Tomlins and Jana Rasakanthan.

Oversampled plots of the PSF at different positions in the B-scan plane are shown in colour in Figure 4-22, showing the clear trend in the shape as the inscription pulse energy is reduced. There is also a notable change in the OCT measurement for points at different depths. The 10% laser power gives noticeable smaller features than the 100% laser power.

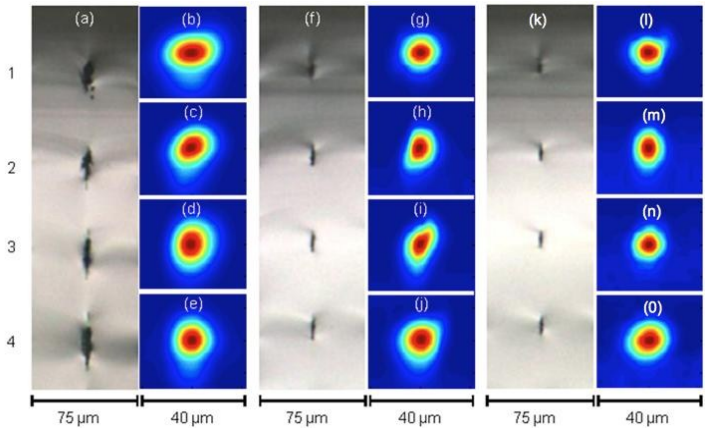

Figure 4-22 Confocal microscope images (a, f and k) of the cleaved, etched artefact with corresponding OCT PSFs (b-e, g-j and l-o) shown on an intensity linear scale. Images a-e corresponds to 100% power, f-j to 20% power and k-o 10% power. Rows 1-4 correspond to depths of 75, 150, 225 and 300 µm from the artefact surface. It should be noted that the full scale for the confocal microscope images is 75 µm but only 40 µm for the OCT measurements. Images captured by Dr Peter Wooliams under guidance for the etching conditions. Data Processed by Dr Peter Tomlins.

For 2.5% laser power it was not possible to measure the feature with the OCT system. However, the images in Figure 4-23 shows the presence of an inscribed feature at the 2.5% power level for depths between 75–300 µm.

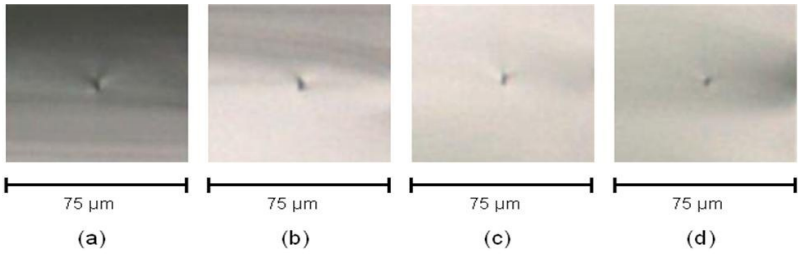

Figure 4-23 Confocal microscope images of the cleaved and etched cross-section of lines written at 2.5% power. Images a-d corresponds with depths from the artefact surface of 75, 150, 225 and 300 µm respectively. Images captured by Dr Peter Wooliams.

4.3.6 Analysis of initial trials

The femtosecond inscription mechanism results in highly spatially localized index changes relative to the substrate material. In fused silica this is due to a resultant material density or chemical change leading to a change in the refractive index. The nature of the pulse-material interaction leads to a resultant variation in the dimensions and appearance of the spot as the thresholds for inscription and ablation with the resultant void creation are exceeded. The elongated elliptical shape shown in the higher intensity artefact lines is characteristic of a focused beams' incident intensity profile where the minimum threshold value is taken to be that of the material threshold. This is accentuated by the use of an air objective and the subsequent refractive index mismatch leading to defocusing effects. This becomes more obvious an issue as the energy incident increases leading to a larger focal spot being above threshold energy leading to elongated focal zones. Above this threshold the material in plasma state undergoes rarefaction and subsequent densification during thermal cooling leading to the index change or void creation. The apparent increase in complexity of the structure is a feature of the spatial intensity variation and subsequent nonlinear absorption at and around the focus at higher incident intensities. At lower incident intensities the profile of the energy distribution above threshold is more localized and results in a more spherical cross-section of index change profile. For this work small voids, with cross section dimensions at or below the resolution of the system, were required. This led to the determination of the inscription threshold for the laser system and glass being a prime requirement.

The use of femtosecond inscription theoretically allows a calibration artefact to be designed to test the resolution of OCT systems from a single B-scan. This can be achieved by inscribing lines perpendicular to the scan planes, creating point like refractive index variations in each 2D B-scan. However, the nature of the femtosecond writing process results in a slight granularity of the lines in terms of the refractive index change in this study. The use of different parameter spaces and glasses would probably assist in greatly reducing the granularity issue. When examined using the OCT this results in a variation in the brightness of response from each line in subsequent B-scan resulting in a 'flicker' when consecutive slices are observed. For the lowest energy inscriptions, the fine intensity threshold dependence for significant index change means that some lines are only visible in a fraction of the B-scans. Hence there is a need to acquire several dozen B-scans to enable accurate results. Although this refractive index variation currently means that a single B-scan may not yield a complete picture of the OCT resolution it indicates the potential for the use of the inscription technique and ability through multiple scans for it to acquire the information required. In addition, the controllable relative positioning of the refractive index features, and subsequent scattering features, also may be used to help calibrate the axial scaling of the resulting OCT images and B-scan field of view distortion. This is important when OCT images are going to be used for the measurement and subsequent monitoring of say possible disease processes.

The OCT instrument pixel size used for this study corresponded to 4.15 μm laterally and 3.92 μm axially (assuming a silica medium at 1300 nm or 5.6

μm axially in air). In prior studies the theoretical axial resolution (FWHM of the intensity) of this instrument (processed with a Hann window) was found to be 10.9 μm and the lateral was 8.2 μm [9]. Figure 4-21 shows the dimensions of the smallest lines to be 1.28 μm (lateral) and 6.6 μm (axial). Since this is below the resolution of the OCT system the points appear to be spherical in Figure 4-22. A key challenge is to reliably reduce the feature size in the axial direction so that it is closer to those shown in Figure 4-23. This will allow artefacts to be made that can be used to calibrate systems on the 1-2 μm scale. I believe this is possible with the assistance of the slit method, spatial light modulation, oil objective, multiple scans and uni-directional writing or a combination of all as mentioned in section 4.2.10.

The axial sizes of the points were found to vary significantly with the power setting as would be expected from the microscope images. There was also considerable spread in size, due to the variability in the appearance of defects. Estimating the PSF of larger defects, written with higher power, was unreliable due to the speckle (the secondary features that can be seen on the high power points shown in Figure 4-20. This speckle make the PSF fitting unreliable and can be explained by the formation of micro-cracks, voids or additional stress in the material caused by the higher power exposure and subsequent filamentation.

In order to estimate the instrument PSF from the data a subsection of the data containing only the weakest points was taken. For each B-scan the points were located in the image using a threshold filter then a Gaussian fit was applied through the middle of each point in the axial and lateral

directions. The goodness-of-fit was calculated, and if found to be less than 0.95 (normalized to 1) then the point was rejected, this helped reject false points caused by image artefacts and gave more robust results.

No defects were reliably visible using the OCT system for powers <5%, suggesting that the resultant refractive index induced by inscription is smaller than the OCT can observe and / or that the energy threshold for index has not been met for the smallest intensity levels. The small size of the inscribed feature leads to an extremely small fraction of the light being backscattered into the OCT instrument requiring the use of highly sensitive instrumentation. The size of the artefacts, measured using a microscope, compare well to the theoretical ideal for the creation of a direct OCT PSF measurement. This is because it is significantly smaller than the resolution of the instrumentation and thus approximates to a delta function in the convolution of the object and instrument PSF that forms the final image [20]. The nature of the inscription approximating to a cylindrical line at these low inscription energies means that this can yield a measure of OCT point spread function in two orthogonal directions.

The weakest points, corresponding to the top 4 layers and the power settings 5% and 10% were looked at in detail. At power levels of 20% and above, axial bifurcation of the points was observed in individual OCT B-scans. However, when multiple OCT images of a single point were combined, the bifurcation ceased and its place and axial tail was evident, as shown clear seen in Figure 4-22 b-e and g-j. The effect of averaging indicates that the bifurcation effect is possibly due to interference between light

reflected from the top and bottom of the defects that exhibit a noticeable depth elongation (Figure 4-22 a, f and k). Chemical (HCl) etching followed by confocal microscope characterization reveals for 100% inscription power, the voids dimensions are up to 17 μm (lateral) (Figure 4-22a). The elongation effect is still visible for 10% power settings (Figure 4-22c). However, the effect is negligible in the OCT PSF measurement (Figure 4-21) and therefore suggest a maximum inscription power levels of 10% for the present setup. Lines written at 2.5% power settings showed less elongation (Figure 4-23). It was not possible to measure these lines reliably using OCT but the confocal microscope images imply that more work could be done around this power level to optimize the line shape should beam shaping etc. not yield the expected results.

The lateral resolution varies with depth as the beam is focused into the sample. By tilting the sample the lateral resolution for the different layers allows the beam waist to be seen. Further samples with writing power optimized to give small defects are being planned.

It is worth noting that the visibility of the lines for any given power decreases with depth in the sample. This phenomenon could be due to the fact that the OCT system was focused close to the surface of the sample and away from this point the probe beam diverges. However, it is also likely that with increased depth the effect of refractive index mismatch is increased elongating the focal area and leading to a less cylindrical index change. Further investigation is required to understand this issue.

The resultant effect of the focused femtosecond pulses depends on the relative intensity of the focused spot in the sample to the material energy threshold. Low intensity pulses change the refractive index, and can be used for producing waveguide-like structures, with typical refractive index variations of around $1x10^{-3}$ in fused silica. As the pulse energy is increased a damage threshold is reached, above which small voids can be formed at the beam focus [18]. Due to the non-linear nature of the interaction, the size of the resultant defect can be on the micron scale ideally suited to the resolution requirements. However, the exact nature of the damage depends on the laser parameters, focusing optics and host material. Increasing pulse energy can result in large voids with filamentation and subsequent micro-cracks forming around the written structures. The uniformity of the substrate was found to be critical in the reproducibility of the point defects. The excellent surface flatness, finish and ease of anti-reflection coating, as compared to the use of the previously used epoxy resins, were also key features of the chosen substrate. Since the completion of this trial knowledge of other glasses that are likely to be more suited have come to light and will be investigated going forward.

For the successful and repeatable production of OCT artefacts both the size of the defects and the repeatability of the writing procedure needed to be investigated. Subsurface defects are very hard to accurately measure, with cleaving being the only one to give accurate results [12].

4.3.7 Conclusions on initial trials

The applicability of subsurface femtosecond machining techniques to the production of test artefacts for the validation of commercial OCT microscope systems has been demonstrated. The artefacts produced consisted of arrays of line defects whose size was shown to be around 1 μm. This is similar in size to the particles used in the previous OCT resolution work and is suitable for the validation of most commercial OCT systems. The advantage of the femtosecond technology is the ability to accurately place the defects at arbitrary locations in a material substrate that has well known optical properties that can be easily polished and anti-reflection coated. The results obtained are in agreement with those in the previous work.

Another advantage of this technology is that the accurate positioning of the defects and the variable size that can be achieved allows the artefact to also be used to test the instrument scaling and sensitivity.

Current work is on-going to optimize the laser settings and pursue improved designs which will be more sensitive tests of OCT systems than this initial trial.

4.4 Future work/Ideas

As has already been mentioned in both the phase mask and OCT phantom work the future progression of this work relies on the incorporation of compensation mechanisms for unwanted focal spot effects that can be compensated for by the use of a range of adaptive optics and an oil

immersion lens. The work should also focus on using oil immersion lenses, although not practical on the system initially used for this work, to reduce some of the RI mismatch issues. A reduction in the translation speed, repeated passes and more unidirectional write combined with a change of substrate should yield better results. The optimisation of writing polarisation and phase front of the laser are also expected to improve the clarity and consistency of the writing process enabling the etch depth to be looked at more readily and the effects of flicker to be reduced for the OCT samples potentially yielding point scanning phantom devices.

5 Optical fibre micromachining & inscription

Having shown development of both inscription and ablation techniques used in femtosecond direct write and devices born of the ability to create complex structure both on the surface and inside the bulk of transparent media it was thought that the techniques should be applied to work in fibre optic cables. The added complexity of the geometry and fine structural properties was found to be a challenge and the methods for overcoming this and creating devices that combine the ability to micro machine and inscribe to create practical sensing devices has been demonstrated in this chapter.

There are many benefits to sensors and communications devices being made in optical fibre. The connectivity, increasing number of fibre based laser sources and reproducibility and quality of commercial fibre has led to most communication systems and a large number of sensing devices being based upon optical fibre technology. The ability to measure or modulate

remotely and over great distances is critical to a number of applications and optical fibres are able to do this at low cost and reliably. Most optical sensors and communication devices are based around periodic modulations of refractive index either within the core or in the cladding region in close proximity to it. These modulations have typically been created by the use of photosensitivity and UV exposure, mechanical deformation and stress, electrical discharge and CO_2 laser treatment. The ability of femtosecond direct write inscription techniques to create index changes at highly localised points within the fibre has been used to write fibre Bragg and long period gratings. In this work the aim has been to use these techniques, with additional ones in terms of alignment and defect creation to create highly tailored index changes to both examine the fundamental inscription techniques and to make practical devices.

5.1 Fibre Bragg grating inscription & point by point grating theory

Fibre Bragg gratings (FBGs) may be inscribed using the point-by-point (PbP) method. The technique was first demonstrated using an excimer laser in 1993 [**124**]; however, it is only since the technique was taken up using femtosecond lasers that it has received more interest for use in fibre lasers and in sensing applications [**125**,**126**,**127**,**128**]. Through the use of femtosecond pulses highly localized micro void modifications are periodical inscribed into the fibre optic core. These structures act to form index variation without the need for photosensitivity of the inscribed media which form low loss, high quality reflection spectra [**129**,**130**]. Through the careful manipulation of the inscription powers they also have

been demonstrated to have high temperature stability due to the fundamental structural modification of the glass through inscription [**131**].

To create the modification an objective lens is placed in the beam path, the optical fibre is then moved through the beam using air bearing computer numerically controlled stages. To create individual modifications of the type of Bragg gratings the stages are moved at a speed such that the repetition rate of the laser creates modification points separated by a controlled distance. Through controlling the repetition rate, pulse picking or the translation speed of the stages the grating period can be carefully set to 10-20 nm precision. This is able to be achieved because of the precision of the pulse delivery and the stage movement being the less accurate of the two. Figure 5-1 below shows the basic set up used for inscription.

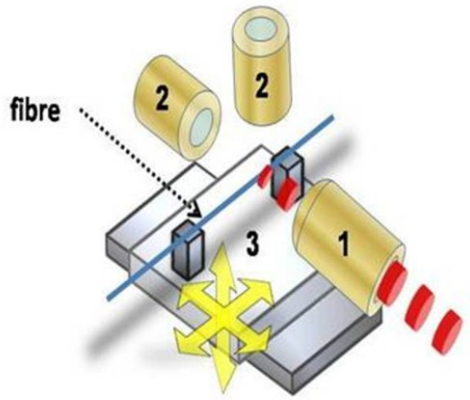

Figure 5-1 A schematic showing the practical inscription layout used with 1 being the objective lens, 2 being the cameras used for alignment and 3 being the Aerotech stages used to create movement relative to a fixed objective lens.

As shown in equation 1.9 the coupling strength κ is highly dependent on the overlap integral. This creates a critical inscription characteristic in the point by point gratings as the coupling strength, for a fixed grating length, is determined by how central the feature is. This is in stark contrast to the plane features that are inscribed by using photosensitivity and UV inscription. This means that extreme care over the modification location has to be taken not only for grating strength, but also for the effect on the side lobes should the structure be tilted. This has been utilised to create apodized gratings [**132**], however, this was not required for this work so the focus was to develop techniques to create reliable positioning of gratings within the centre of a fibre optic core.

The nature of standard optical fibres being cylindrical adds complications to the precise focussing in the centre of the fibre core. The geometry serves to deform the pulses and act as an unwanted lens. The compensation for this effect is, however, more complex than an axial offset being applied as with a minimal tangential (to both fibre and beam axes) offset the position of the focal spot can change significantly even if in the correct beam height plane. This means that without any aids such as oil or ferrules the positioning of the fibre relative to the objective lens requires sub-micron levels of both accuracy and repeatability. This is commonly found to be too challenging as mechanical distances during fibre suspension often create vibrations and the use of v-grooves significantly impairs the use of vision systems. The techniques to overcome the level of precision required were through the use of microscope cover slides and index matching gel (Figure

5-2), the use of a green fibre coupled laser during the alignment stages and the use of a spectrometer to identify when the plasma generation was coupled into core guided modes. Through the use of these additions to standard microscope objectives and cameras the alignment was precisely achieved.

5.2 LPG inscription

The technique for inscribing the LPGs using femtosecond lasers is very similar to that used for the creation of FBG. However, the speed of translation is reduced to create continuous lines of index change and the shutter is programmed to gate at longer periods. Through the majority of this work the periods were between 200 and 300 μm as for most fibres this produced attenuation bands centred on 1550nm which was where most of the sources and analysis equipment available operates.

The long period grating works by promoting coupling between the propagating core mode and co-propagating cladding modes. It is through the high attenuation of the cladding modes that the transmission spectra attains its characteristic series of attenuation bands centred at discreet wavelengths, each of which represent a different coupling to cladding mode. Outside of environmental conditions (temperature, bend radius, strain and local refractive index) the form and central wavelength of the attenuation bands are determined by the period of LPG modulation and overall length. The modulation of the environmental factors serves to alter the differential refractive index profile and subsequently the phase matching conditions for the coupling to the cladding modes which in turn

results in a change in the central wavelength and shape of the attenuation bands as viewed in transmission. The sensitivity to the environmental conditions depends acutely on the absorption band order and specific spatial index profile. This is deliberately manipulated to create sensor devices in this chapter.

In most optical fibres the fibre consists of two bodies that can act as waveguides. One is the high index core with lower index cladding; the second is the cladding with air acting as the cladding. The phase matching condition for the mode to propagate in both is achieved when the wavelength, λ, is given by,

$$\lambda = \left[n_{eff}(\lambda) - n^{i}_{clad}(\lambda)\right]\Lambda \qquad \text{Equation 5-1}$$

Where $n_{eff}(\lambda)$ is the effective refractive index of the core mode propagating at the given wavelength, $n^{i}_{clad}(\lambda)$ is the refractive index of the ith cladding mode and Λ is the physical period of the LPG.

The minimum transmission of the attenuation bands is given by the expression,

$$T_i = 1 - \ sin^2(\kappa_i L) \qquad \text{Equation 5-2}$$

Where L is the length of the LPG and κ_i is the coupling coefficient for the ith cladding mode. This is determined by the overlap integral of the core and cladding mode and by the amplitude of periodic modulation of the mode propagation constants.

The relatively large dimensions of typical fibre cladding, allows a number of modes to be supported. The modes that are most commonly found are those that have efficient coupling between the core and cladding modes. This is caused by large overlap integrals i.e. they have similar electric fields. This results in coupling between core and circularly symmetric cladding modes being dominant, where the odd mode orders (as the even modes have low field amplitude in the core) where the electric field profiles peak within the core propagate.

5.3 Gratings

Work in this area was largely carried out as a means of testing the alignment and inscription parameters used when working in optical fibre. Initial work was carried out in reproducing work done with Dr Yicheng Lai during my initial training in the creation of 1st order gratings at 1550nm point by point inscription. The work carried out with Yicheng involved the use of a glass slide with oil to negate the effect of the fibre curvature; however, the significant development carried out in part with Dr Kyriacos Kalli did not use oil to create grating structures as are shown in the Figure 5-2 below.

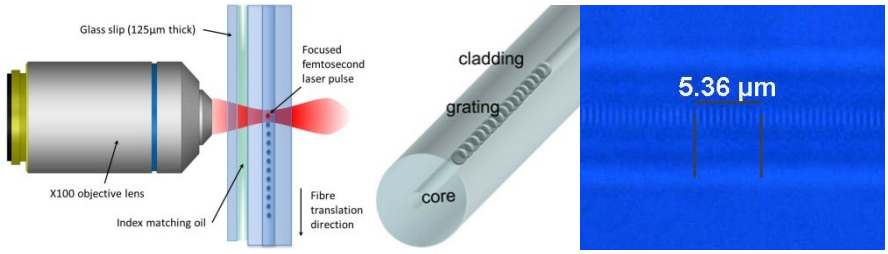

Figure 5-2 Shows the inscription technique using oil, a schematic of the result and the resultant index modulation created.

One of the key advantages of using femtosecond point by point inscription for creating grating structures is the ability to position them carefully within the core, and control that positioning. This has been used to good effect in creating apodized structures by other groups, but in our case was used as a means to characterise the ability to inscribe structures at specific locations within the core or cladding. Some test grating structures are shown below. These are written as 2nd order gratings for 1550nm, so spaced at 1.07 μm, written at 1 kHz with 100x Mitutoyo lens.

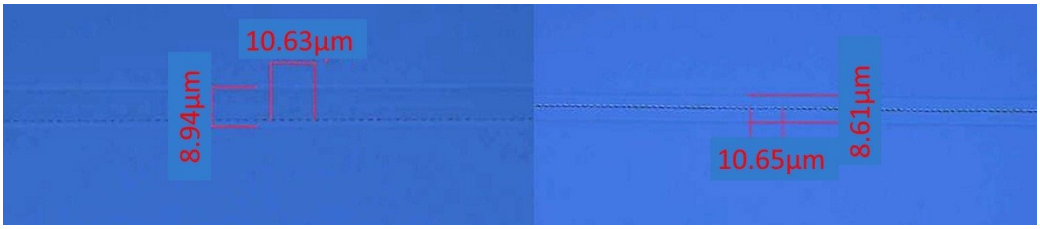

Figure 5-3 Shows two microscope images of two separate fibre Bragg gratings with the positioning to one side of the fibre core centre and centred in the core demonstrating control in alignment and inscription.

The grating work was developed further and is discussed in more detail in section 5.7 where it was used as part of a combined device. The ability to controllably write structures in the fibre core led to the inscription of long period gratings written in PCF. This extension is discussed in the next section.

5.4 LPGs inscribed for fundamental characterisation and sensing

The work on creating LPGs in standard and photonic crystal fibres (PCF) was largely focused on characterising their behaviour and only touched on some of their sensing capabilities. My role was primarily in the

femtosecond inscription with Dr Kaiming Zhou and analysis of the data while my various collaborators from Aston University and the Cyprus University of Technology worked on the characterisation and data processing. The creation, through inscription, of LPG in standard fibre initially enabled the techniques to be optimised from the initial work in FBGs as detailed in 5.3. The only real differences being the inscription translation speed and the application of different shutter timings based upon the desired duty cycle. This then led to working in PCF, see Figure 5-4 for PCF structure, for the creation of a series of LPG of different periods, inscription powers and overall lengths. These were then either used in annealing experiments or tested for their sensing properties.

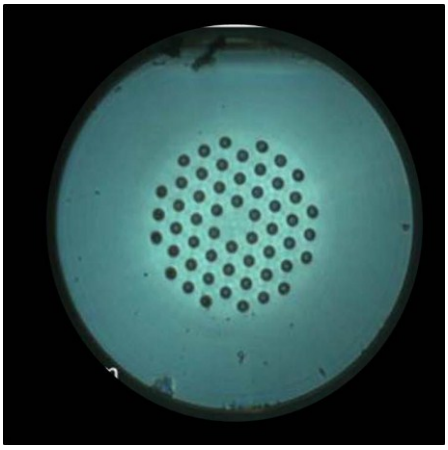

Figure 5-4 A micrograph showing the structure of the photonic core fibre used to inscribe long period gratings into. The solid core is approximately 9 microns in diameter and the total fibre diameter is 125microns.

The use of the femtosecond inscription means that the use of photosensitive fibre is not required, combined with the sensing potential of PCF fibres they serve to make femtosecond inscribed LPG of interest to researchers.

The interest in PCF is as a result of fibre being able to be tapered and have the hole sizes varied and spatially varied. These geometrically based changes can be utilized to create fibres designed for a range of sensing applications. The other benefit is the ability to use a range of materials to create the PCF fibre. They have the ability to be designed to be single moded in transmission over hundreds of nanometres. It was found that the inscription of well-defined gratings structures was impossible without filling the PCF holes with refractive index matching holes. This created asymmetry in the inscribed features which in turn fabricated birefringent gratings that can be used for bend sensing but can also be used in other sensing applications. The fundamental understanding of the effect of the PCF lattice geometry on the inscription was little understood, and the focus of some of the work presented here, as too is the question of some of the mechanisms that lead to index change within the fibre. The effect of both also then affects the spectral stability of the gratings which was also studied, through post-fabrication analysis, in the work produced with these LPGs.

The inscription of the LPGs produced here was carried out at Aston University with the Low repetition rate laser system as described in section 2.2.2. This system was specifically set up for fibre inscription work and was as such the ideal choice for the complicated effects of the geometry. The work was carried out without using oil to compensate for the geometry of the fibre. This was done because it was decided that there was no way of removing the index fluid after inscription before characterisation. The

single processing step of the point-by-point inscription technique enabled the characterisation to be compared to well understood modelling of LPG structures, whereas the addition of oil would have altered the spectral characteristics in a way that would complicate this. The LPGs were also compared to arc induced gratings produced in some of the collaborators prior work. This was another factor in writing them without the aid of index matching fluids as it allowed direct comparisons to be made.

A series of LPGs were fabricated with an 800nm femtosecond in Endlessly Single Mode ESM-1550-01 PCF supplied by Crystal Fibre A/S. Gratings with periods ranging from 300μm to 520μm were inscribed. This yielded the result that as the grating period increased the resonant wavelength decreased which was found to be in agreement with previous studies of endlessly single mode PCF [**133**,**134**].

The spectral response with annealing temperatures does not depend on the grating period so one period was selected and used for this work. This also fixed the cladding mode order being investigated which may have affected the spectral sensitivity. The prime focus became to vary the inscription energies used to write the LPGs at 400μm periods between 410-650nJ. The inscribed grating lengths were varied to achieve maximum attenuation band strength. The spectra-physics spitfire evolution Ti: Sapphire laser was used at 800nm, 1 kHz repetition rate, a pulse duration of 150fs and with a x100 (NA=0.55) objective lens with a translation speed of 10μms^{-1} with a

50:50 duty cycle. This results in approximately 25 pulses forming any given inscribed area.

A camera system was used to monitor both changes in the fibre geometry to ensure that the fibre was not twisted and for the initial fibre-laser alignment. The alignment procedure used to inscribe the LPG into the central region of the PCF relied on visual inspection of the fibre with a camera system see Figure 5-1 in section 5.1. Prior to the inscription of the LPG, several laser shots are targeted into the fibre core on either side of the region where the LPG will be written, and the camera system is used to image light scattering from these alignment points. The scattering is weak and so the light is launched into the fibre using a frequency doubled Nd:YAG laser, if the "shots" are in the core region then the green light is strongly scattered and viewed using the CCD of the imaging system, thereby confirming that the fs pulse has been focused into the fibre core. This is done because use of an imaging alone is not sufficient as the microstructures of the PCF serve to obscure accurate identification of single shots within or near a fibre core.

Previous investigations into the spectral characteristics of fs-laser inscribed LPGs [**135**] have shown that it is necessary to constantly optimize the polarization of the illuminating light in order to correctly monitor grating growth during fabrication. This was realized using the configuration shown in Figure 5-5 below.

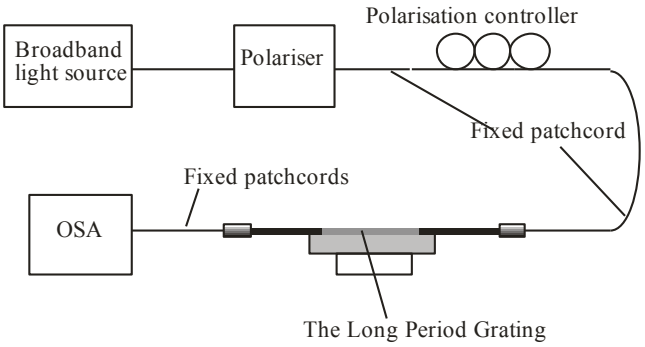

Figure 5-5 A schematic of the apparatus used to investigate the transmission spectra of the LPGs during fabrication.

The femtosecond gratings and the arc induced gratings were annealed in a Carbolite 1200°C horizontal tube furnace (MTF model 3) by Dr Tom Allsop and Dr Kyriacos Kalli doing the characterisation testing.

5.4.1.1 Grating birefringence

When the data from the characterisation was analysed the position and strength of the laser-inscribed LPG transmission resonances was found to be polarization dependent this is shown in Figure 5-6a and Figure 5-6b. The observed birefringence is a consequence of the asymmetry induced during inscription; this increased for inscription energies up to 550nJ and subsequently decreased for higher inscription energies. This was found to lead to a maximum change in resonant wavelength of 10nm and an observable maximum change in optical strength of 18dB. The observed birefringence is smaller than that produced in SMF using the same laser parameters [**136**]. This is considered to be a consequence of the incident laser light being scattered by the holey lattice PCF structure.

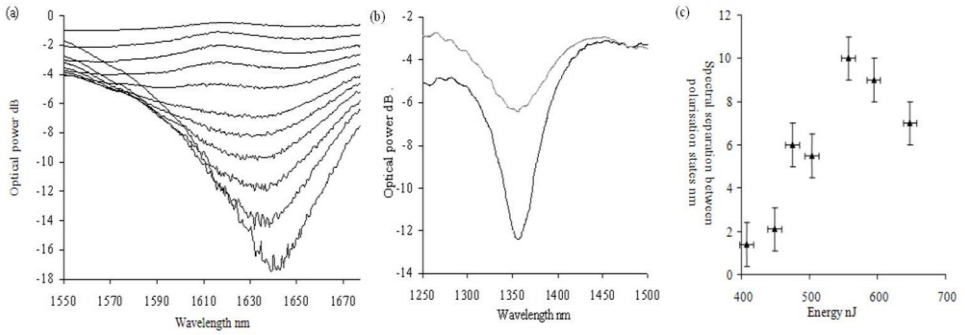

Figure 5-6 (a) Polarisation dependence of the transmission spectra of the fs-laser inscribed LPG in PCF (ESM) with a period of 400µm, inscription energy of 650nJ and length of 10.0mm Polarisation changes from 0° to 180°. (b) Maximum variation of the polarisation dependent transmission spectra of an LPG in PCF (ESM) with a period of 400µm, inscription energy of 510nJ and length of 7.2mm. (c) Maximum variation of birefringence versus inscription energy. Data collected and analysed with Dr Tom Allsop and Dr Kyriacos Kalli.

The femtosecond laser written structures written are shown in Figure 5-7 below. From the images in this figure it can be seen that the resultant femtosecond laser inscription is asymmetric. At lower pulse energies of 410nJ per pulse discolouration occurs and a clear cracking of one of the microstructured holes (circled in the figure). These observations are enhanced at the higher pulse energies of 590 nJ=pulse and 650 nJ=pulse, where additional discoloration and significant internal fracturing of the fibre was observed.

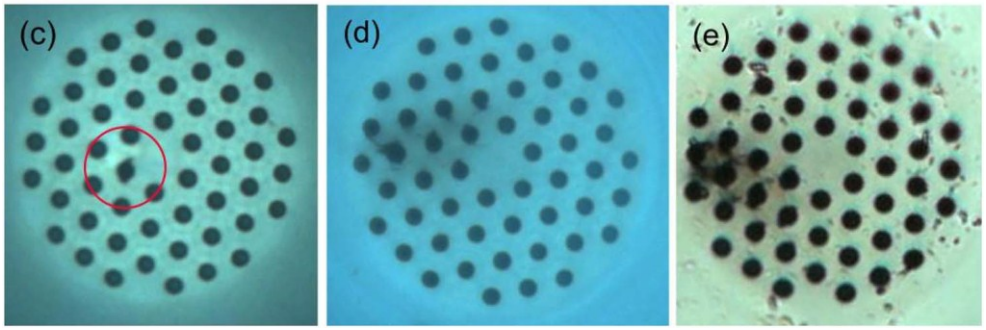

Figure 5-7 Fs inscription at 590 nJ = pulse (discoloration and fracture), and fs inscription at 650 nJ=pulse (discoloration and greater fracture). Images captured by Dr Kyriacos Kalli.

5.4.1.2 Grating stability

Following the fabrication, LPGs were left to anneal at room temperature over several hundred hours. During this time the grating spectra were recorded at regular time intervals and the evolution of the grating resonant wavelength and its optical strength were recorded. An example of the data collected is shown in Figure 5-8, it shows shifts to both longer and shorter wavelengths. The birefringence reduction of the LPGs during this time was also observed and this can be seen in Figure 5-10. The maximum wavelength shift was observed to occur within the first 120 hours post fabrication and was measured to have shifted +27.3 nm, this occurred for LPGs inscribed with the lowest laser energies (410nJ). Conversely, the smallest wavelength shift of 2nm occurred for the gratings written at the higher laser energy of 650nJ.

All LPGs displayed the characteristic red followed by the blue wavelength shift, with a resultant overall wavelength shift of less than 2nm. For inscription energies below 550nJ a net blue wavelength shift was measured, above this energy the net wavelength shift was red. The minimum time required before the gratings had reached a stable wavelength was found to be related to the inscription energy with the highest taking the longest time. It was observed that the time for all gratings to have stabilized was 600 hours. The strength of the gratings was generally found to decrease, however, the 650nJ pulse energy LPG strength actually increased see Figure 5-11.

The evolution of these gratings post fabrication is shown to be correlated to the relaxation of thermally induced stresses. To validate the hypothesis the annealing was accelerated by monitoring the gratings in temperatures of 100^{o}C. This showed the 650nJ inscribed grating stabilized in 1/3 of the time as compared to at room temperature. The 410nJ grating did not stabilize within 250 hours. This indicates competition between the mechanisms at different inscription energies.

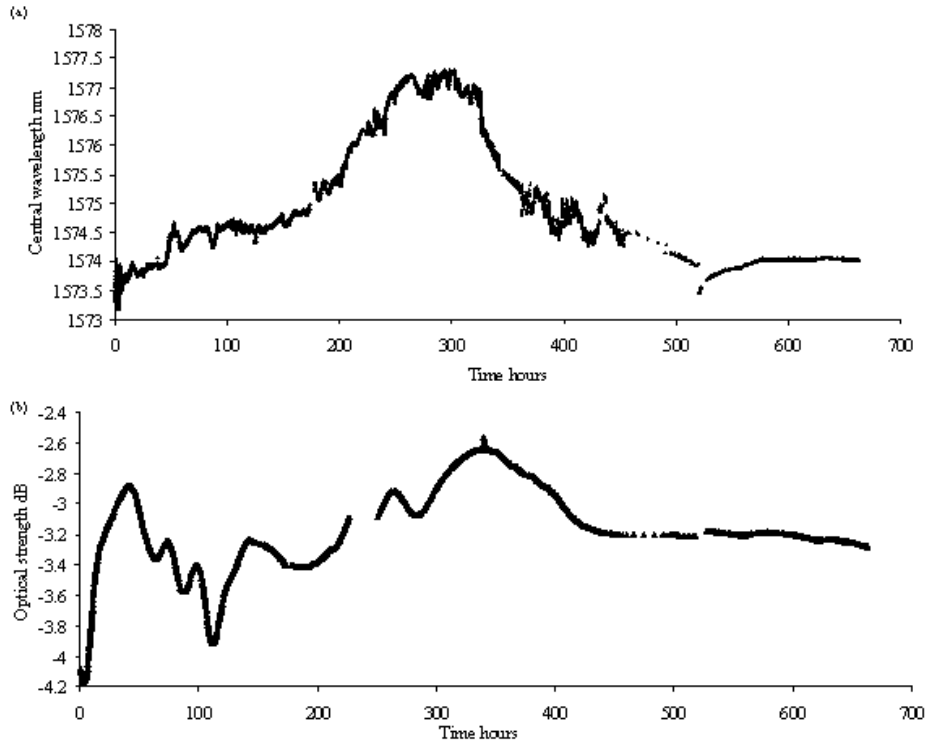

Figure 5-8 An example of the post-fabrication spectral evolution of the a) peak wavelength and b) coupling strength of a fs-laser-inscribed LPG in PCF with period 400µm, laser pulse energy 580 nJ, and length 7mm. Data collected and analysed with Dr Tom Allsop and Dr Kyriacos Kalli.

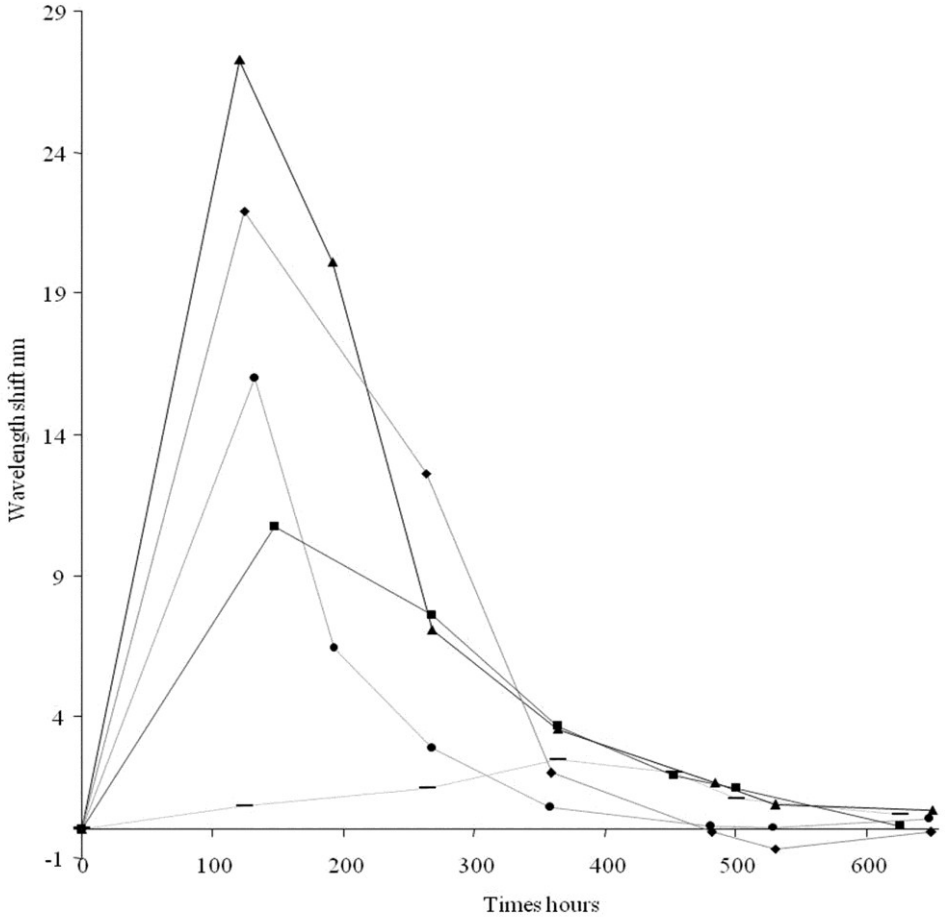

Figure 5-9 Wavelength shifts of fs-laser-inscribed LPGs in PCFs at room temperature. Pulse energies used to inscribe the LPG were (▲) 410 nJ, (×) 450nJ, (♦) 510nJ, (•) 550nJ, (■) 560nJ, (▬) 650nJ. Data collected and analysed with Dr Tom Allsop and Dr Kyriacos Kalli.

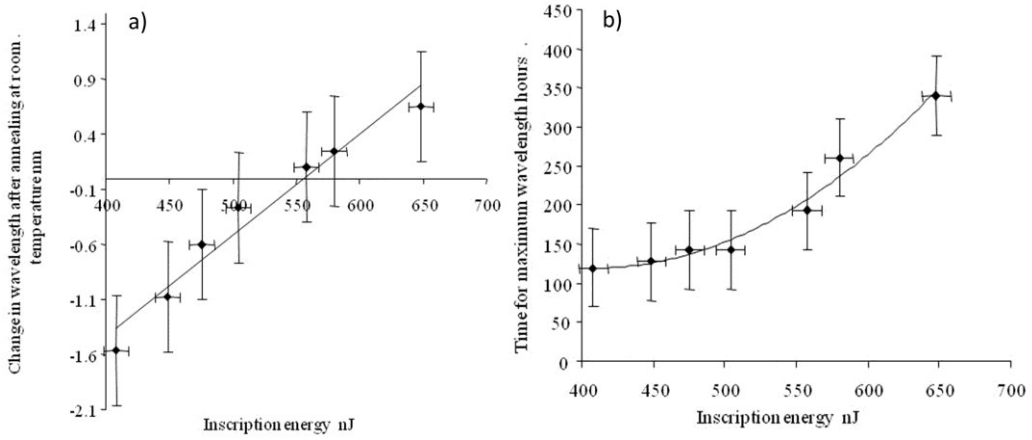

Figure 5-10 a) Total wavelength shifts of fs-laser-inscribed LPGs in PCFs as they are annealed at room temperature as a function of inscription energy, b) Time for maximum wavelength shift to occur as a function of inscription energy. Data collected and analysed with Dr Tom Allsop and Dr Kyriacos Kalli.

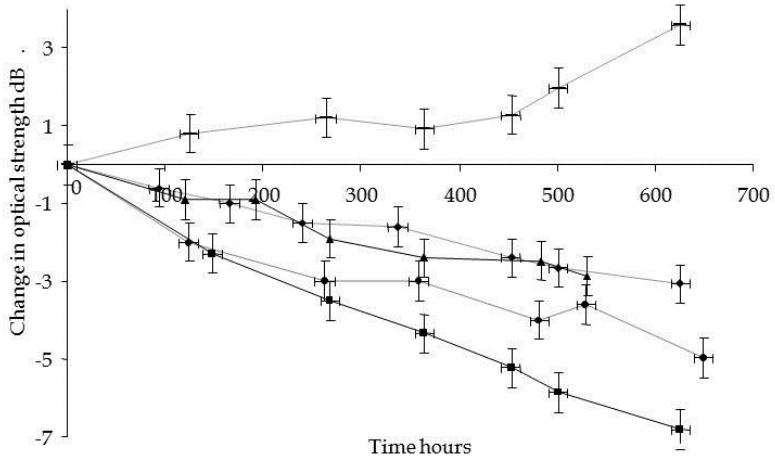

Figure 5-11 Change in coupling strength of fs-laser inscribed LPGs in PCFs at room temperature. Pulse energies used to inscribe the LPG were (▲) 410 nJ, (♦) 510 nJ, (•) 550 nJ, (■) 560 nJ, (▬) 650 nJ. Data collected and analysed with Dr Tom Allsop and Dr Kyriacos Kalli.

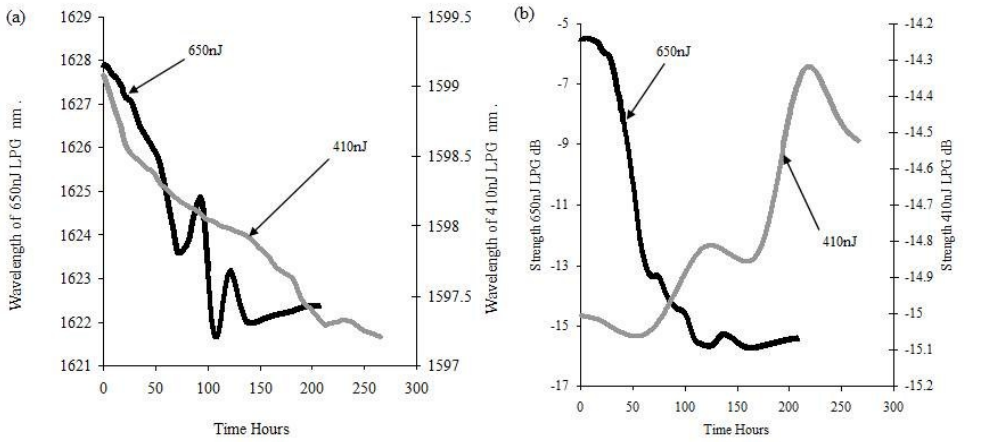

Figure 5-12 Examples of the spectral variation of (a) the central wavelength of an attenuation band and (b) optical strength of fs-laser-fabricated LPGs in PCF as a function of time at 100oC: ▲ - period 400µm, length 9.6mm, inscription energy 410nJ, ▲ - period 400µm, length 10.0mm, inscription energy 650nJ. Data collected and analysed with Dr Tom Allsop and Dr Kyriacos Kalli.

As discussed in earlier sections the material absorption (multi-photon) and damage thresholds are critical to the final form of material modification. These result in quite different results from the formation of colour centres and change in fictive temperature to the formation of voids and densification. The results of the annealing work presented here show both reversible and irreversible index changes occurring in the instability of wavelength and strength to the long term durability of the gratings respectively. These variations are dependent on the inscription pulse energies used. At high inscription energies the grating strength increased during annealing whereas the opposite was found with the low inscription energies. This change appears to occur either side of 600nJ showing a

change in fundamental modification mechanism difference either side of this energy.

When analysing the effect of the modification it should be remembered that the grating spectra is formed by the difference in the index between the modified and unmodified regions. Since the unmodified fibre is affected very little by the annealing the dominant change is caused by changes to the inscribed region. At lower energies the grating strength decreases and the rate of decrease is higher with increased temperature. This is likely to be relaxation of elastic strain, reducing the index. The strain increases with the pulse energy which causes the larger decrease in grating strength at higher energies. Through analysis carried out by Dr Kyriacos Kalli, Dr Tom Allsop, Dr Jovana Petrovic and I using LPG theory it was shown that the thermal strain contribution to the initial index modification varied with inscription energy at a given annealing temperature. For low inscription energies with increased annealing temperature an increased index modification as a result of increased induced strain is shown. The results of higher inscription energies show a decreased modulation from a reduction in the strain with increased annealing temperatures. This can only be achieved with LPGs and not FBG because of the fundamental difference in the inscription, where FBG are useful for the measurement of differences between reversible and irreversible changes where LPG measure the total refractive index change. This is because the LPG grating period is not defined by a single or few laser pulses where both reversible and irreversible processes occur around each modification as is the case for

FBG.

Dr Jovana Petrovic used Finite element analysis in COMSOL to analyse the writing asymmetry found as the hole to inscription angle was varied. Figure 5-13 shows the propagation of the light as it is scattered by the lattice hole structure. It shows how the hole alignment can make a hugely significant difference to the propagation and focusing.

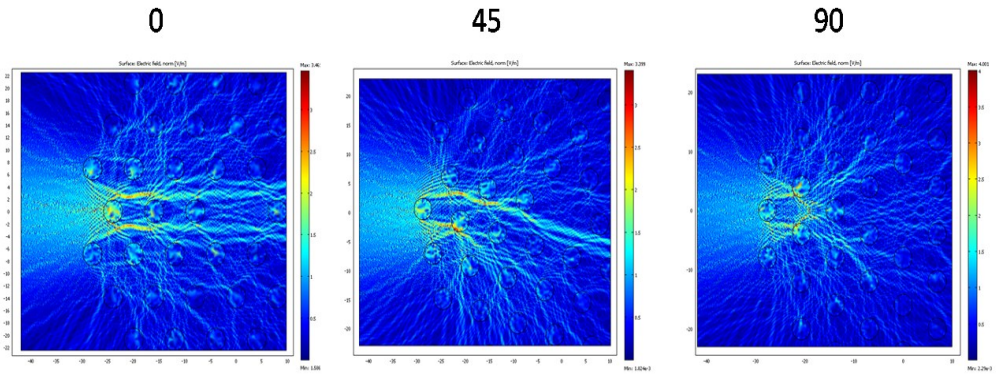

Figure 5-13 Simulated incident inscription of a PCF from different relative angles leads to different intensity distribution within the fibre, as shown for three relative fibre rotations of 0°, 45° and 90°. The field is normalized to 1 at z = –70µm. The geometry of the PCF was reduced in order to achieve the best possible mesh in the simulation. Simulation and images carried out by Dr Jovana Petrovic.

By applying a threshold of 10^{12} W/cm^2 [**137**] these same models (see Figure 5-14) can be shown as a feature of only where the energy is sufficient to cause modification. This shows how for different fibre orientations the position of effective focus can vary significantly due to scattering. The result supports the high birefringence and large inscription energies seen in

the practical work through the scattering causing modification in the cladding requiring larger energies than in bulk material [**137**].

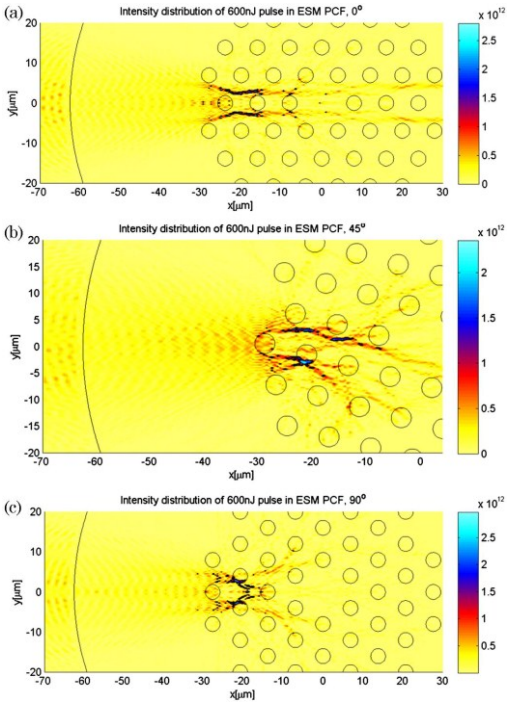

Figure 5-14 Simulated incident inscription of a PCF from different relative angles of 0°, 45° and 90° showing the intensity distribution above the absorption threshold chosen to demonstrate where the inscription occurs. Simulation and images carried out by Dr Jovana Petrovic.

The nature of femtosecond direct write inscription in fibres is typically results in asymmetry; however, this is exacerbated in the inscription of PCF as the scattering causes non uniform index change. The work yielded some interesting results, but should be taken with some caution as the relative rotation bears such a large influence on the focusing and is so challenging to make consistent during a single fibre inscription let alone between fibres no matter how thoroughly one tries.

5.5 FIMA slots and other work from FIMA

Initial work on fibre micromachining began by using inscribe and etch technique to machine slots into the cladding and core of the fibre. This was carried out mostly by Dr Yicheng Lai and Dr Kaiming Zhou at Aston University and involved working post alignment from the far side of the fibre to the near (in the reference frame of the objective lens). The rastering along the fibre axis with progressive steps of the fibre away from the objective lens at inscription powers at the level of index change left thin modified regions. These fibres were then dipped in HF in foam baths placed in extraction hoods. Extreme care had to be taken when dealing with HF, however, it has been shown to have a preferential etch rate preferring the modified regions to un-modified at a ratio of 100:1. This whole process created smooth and thin channels with many uses in microfluidics and refractive index changes. The process had extremely long processing times of many hours for the femtosecond write process, several more for the set up and processing using hazardous chemical etching and cleaning. This would result in devices taking several days to produce. This also fell short of the need to tap light from the core of an optical fibre. This had been the focus of a project combining collaborators from Oxford Lasers, Fiberlogix and Aston University.

The goal of the project had been to create a usable sensor for the detection of power in high powered fibre lasers, fibre polarisers and other devices with the potential to provide sensing capabilities through coupling to the evanescent field of the core mode. One of the partners, Fiberlogix, used the

technique of polishing the fibres using a wheel polisher and spindle arrangement. They would monitor the fibre losses and use this as a way of calibrating their resultant devices. The resultant device had a curved taper and a microscope image with periodic distance measurements is shown below in Figure 5-15.

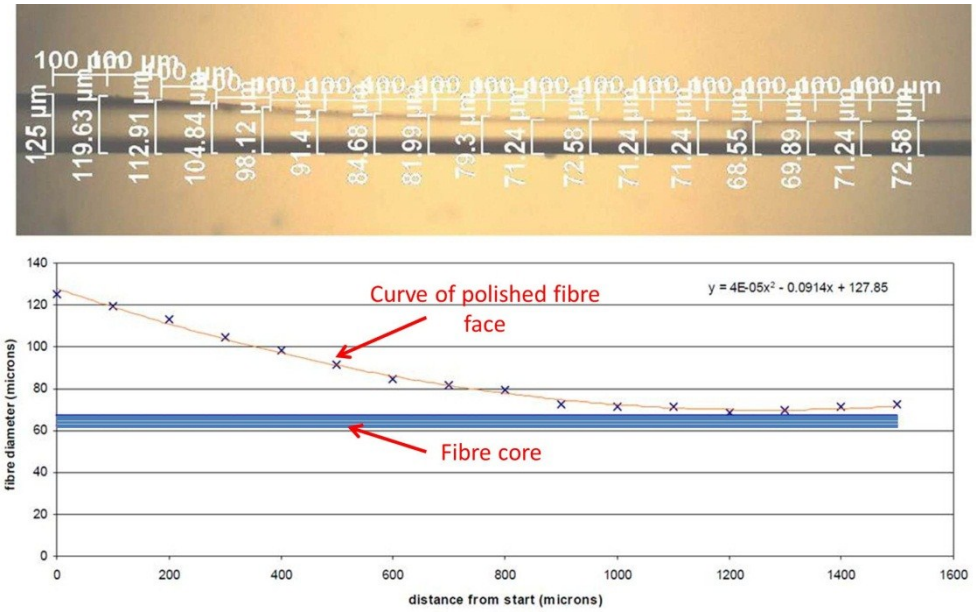

Figure 5-15 A microscope image taken of a side polished fibre from Fiberlogix, the measurements made are then plotted to more clearly define the shape of the curvature.

This was done initially to characterise the curvature in order to understand the nature of the taper as the collaborators had not characterised their device in terms of the taper. It was decided that after review of this shape we would initially try to make a slot in one axis of the fibre, preferably without the use of chemicals and with ablation techniques alone. The dimensions of these slots were defined by the collaborators with the critical

distance being the distance between the core cladding interface and the bottom of the slot being 15µm in separation. This offered the right degree of out-coupling and provides a good replication of the existing devices. Although initial trials with inscribe and etch techniques in fibres were undertaken with Dr Yicheng Lai and Dr Kaiming Zhou it soon became clear that even when angled channels were fabricated the main mechanism became scattering at the angled interface. The channels were written in oil, from far side to near relative to the objective lens, to avoid fluting found to be caused by writing through previously inscribed areas. The insertion loss of the devices were found to be low, however, there were issues with the oil immersion, as the small dimensions did not allow for easy flow through the channel. An example of the channels written and etched is shown in Figure 5-16 below.

Figure 5-16 show microscope images of inscribe and etch channels inscribed using an 800nm, 120fs pulse laser and etched using HF acid. Work carried out with Dr Yicheng Lai and Dr Kaiming Zhou.

The combination of difficulties with this technique caused a change in project direction towards using "cold" ablation techniques. Initial work on

the ablation section of this project started with Dr Kyriacos Kalli working at the Cyprus University of Technology. The work started with channels in microscope slides to attain the parameters that would form the basis to start machining the fibre. The tests included work on the translation speeds, powers, rastering techniques and removal rates and subsequently the vertical steps taken to ablate the next layer of material. These initial tests resulted in the development of code that would raster rectangles after initially aligning to the fibre centre. The dominant motion would be along the fibre axis, then a step would be introduced perpendicular to the fibre and beam axis, this would be repeated until the desired slot width had been achieved. The fibre would then be moved towards the fixed objective lens. The rectangle would be repeated and another layer of fibre removed. This would be repeated a number of times until the desired slot depth had been achieved.

The key parameters, ascribed by the commercial partners, were initially set to be as follows for the two types of device.

Power monitors.

- Fibre pigtail lengths at each side of machined structure: >0.75m
- Fibre strip length: 8mm (Fibre strip length should be no shorter than 6mm or longer than 12mm)
- Dimensions of ablated structure:
    - Length: 1-2mm
    - Width: 50μm
    - Depth: 54.4μm (i.e. 4μm cladding remaining above core)
- The above structure should (hopefully) give the following optical characteristics to the fibre:
    - Loss in air: <0.1dB
    - Loss in 1.50 refractive index oil: 0.2-0.5dB

Fibre polarisers

- Fibre pigtail lengths at each side of machined structure: >0.75m
- Fibre strip length: 15mm
- Dimensions of ablated structure:
    - Length: 10mm
    - Width: 50µm
    - Depth: 56.9µm (i.e. 1.5µm cladding remaining above core)
- The above structure should (hopefully) give the following optical characteristics to the fibre:
    - Loss in air: <0.2dB
    - Loss in 1.50 refractive index oil: 30-50dB

In terms of the micromachining the lengths of fibre and strip length were largely insignificant as through the use of Nitromors paint stripper the fibres could be stripped repeatedly without structural damage and the length outside of the clamped region did not affect the processing. The two most challenging things were the control of the depth, with subsequent effect to the coupling and integrity, and the surface roughness of the bottom of the groove. The initial work found that often the depth would be underestimated and as such the grooves would penetrate the core. This led to a reduction in the number of overpasses or depth steps taken. It was found that the best results happened when, through the use of a larger plasma, fewer step overs were required. This is considered to be due to the nature of the writing process generating a less fine focus, thus needing fewer passes with larger pitch. The result tended to be a less furrowed bottom surface with a higher aspect ratio side wall. Although the side walls aspect ratio was not of key importance the ability to process these structures with reasonably straight edges for potential insertion of detector devices was viewed as a secondary requirement. After several sets of

iteration the final device results were characterised using microscopes to find the relative translation distance between top and bottom of the micromachined surface. The fibre shown in Figure 5-17 below was written with pulse energy of 10μJ, at a speed of 5mms^{-1} along the fibre axis (with shutter control), with a translation total perpendicular to the beam of 46μm to compensate for the focal width and effect of the fibre curvature. It resulted in a groove that was 5mm x 46μm x 49.4 μm in length, width and depth respectively. The images below show a fibre that has not been cleaned or treated in any way. The image on the right shows the dappled surface relief created. This was found to be a challenge that although it could be reduced to levels far better than delivered with nanosecond machining was never fully diminished to optical quality finishes.

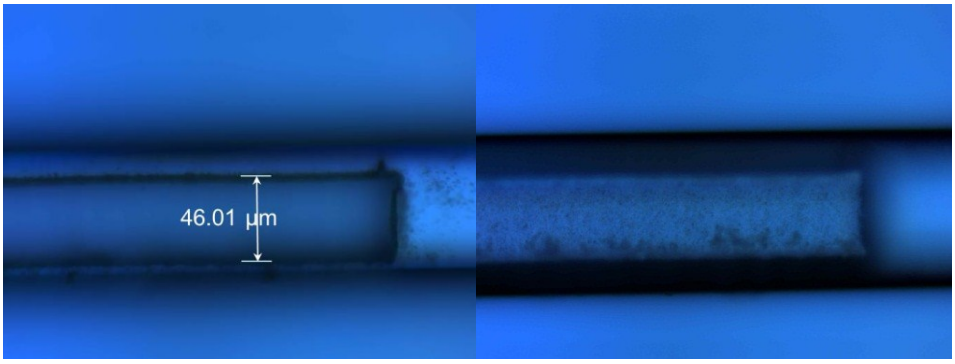

Figure 5-17 microscope images of the top and bottom surface of a micromachined slot in smf-28 fibre. This work was carried out with Dr Kyriacos Kalli.

Although subsequent fibre trials achieved the required depths to within a micron the surface roughness proved to be too great for the industrial partners at the time of this work. The results showed sufficient out coupling to make the device specifications; however, because of the

roughness resulting in scattering at the air-cladding interface (as with index matching oil the surface roughness was tolerable) leading to scattering and a loss of directionality. There was also partially increased fragility, although reduced through use of tapered corners creating fewer stress points, compared to traditional polishing methods so the work although showing promise was redirected towards other techniques to achieve the goals set. At this point I explored the use of inscription alone to create guiding structures within the fibre and this forms the basis of section 5.6.

5.6 Light Pipe

During the course of work carried out on machining the optical fibre as described in section 5.5 it was conceived that there were other ways to tap a small fraction of the light guided in the optical core to the cladding air interface without compromising the structural integrity of the fibre even to the small degree that a well machined channel did. The idea of creating a waveguide or light pipe, coupling light from the core-cladding interface to the cladding-air interface was thus attempted on the Aston micromachining set up. Initial trials consisted of diagonal lines inscribed from the core to the cladding whilst the stages translated along the fibre core and away from the objective lens. This was found to give large scattering when illuminated with a fault finding HeNe laser. This led to attempting to couple sufficient light from the evanescent field surrounding the core mode of the fibre. To do this the inscription would have to start close enough to the core to couple, without causing either direct or indirect damage to the core creating a scattering centre. This was found to be particularly difficult with the fibre geometry causing a variable offset in the

vertical position of focus and if not precisely aligned in the perpendicular plane to the fibre axis. With significant iterations it was found to be possible and several devices were created for testing using this technique.

In an attempt to optimise the process two fibres were written with a total of 5 guides at varying inscription energies. The energies used were 10, 9, 8 (x2), 7 μJ. Each of the two fibres were aligned using guiding spots and detecting the plasma guidance using an ocean optics spectrometer to find the core and align the fibre accordingly. Once inscribed the fibres were characterised, by Dr Thomas Butler of Fiberlogix, for their Insertion (IL) and Polarisation Dependent (PDL) losses. The effect of immersing them in high refractive index oil was also carried out on the fibre containing the two highest inscription energy guides.

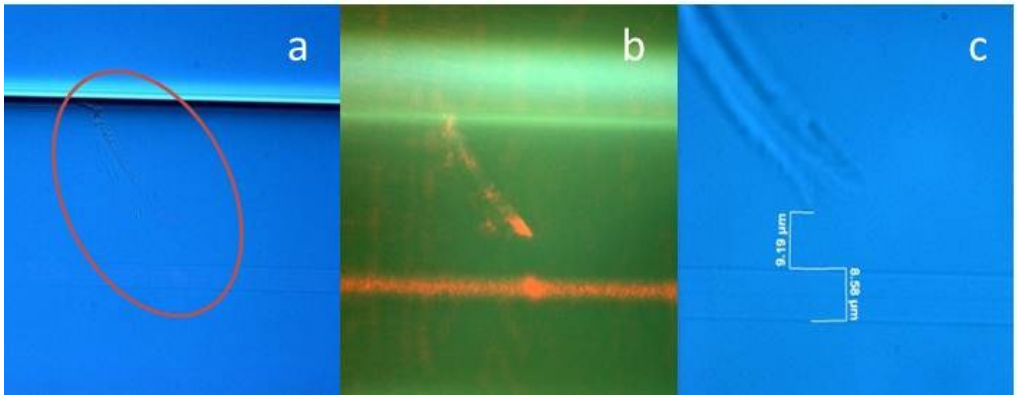

Figure 5-18 Microscope images showing the light pipe a) from air-cladding to fibre core (inscribed structure encircled) b) dark field microscope image with red light guiding in the core showing out coupling at the interface of the guide and core c) fibre core and guide structure, showing a separation of 9.19μm.

Table 5-1 summarises the IL and PDL at a wavelength of 1550nm for the 2 fibre devices. Device F2 with the 3 lower inscription energy waveguiding lines showed the higher IL. The table shows there was only a nominal change in IL when device F1 was immersed in oil. This would suggest that, unlike side-polished fibres that were the focus of a partner in the project, there is no evanescent wave coupling dependence. It should be noted that there was no way to characterise the losses due to the alignment spots and what was due to the devices themselves. The alignment process was subsequently improved but after the initial trial work presented here had finished and so an expected decrease in the losses would be expected due to reduced dependence on alignment spots in the fabrication.

Fibre Number	F1	F2
IL in air(dB)	0.83	1.47
PDL in air(dB)	0.20	0.14
IL in oil(dB)	0.84	Not tested

Table 5-1 IL and PDL for fibres with waveguiding lines

Using the two fibre devices studies were carried out to investigate the angular distribution of light coupled out of the waveguiding lines in the fibre. Using the information on where the waveguiding lines were in relation to alignment spots on the fibre and the scattering the alignment spots created with the red fault finder the positions of the waveguiding lines were aligned over an InGaAs photodiode. Through first finding the alignment spot and then translating the fibre a known distance, the

waveguiding line was positioned directly over the detector as shown in Figure 5-19 below. The light source launched into the fibre was then changed for a 1550nm laser source. The photocurrent from the photodiode was monitored while the fibre was rotated above it. In the ideal case of a directional coupler the maxima were expected to be found when the rotational position of the out coupling of the waveguide line was over the detector.

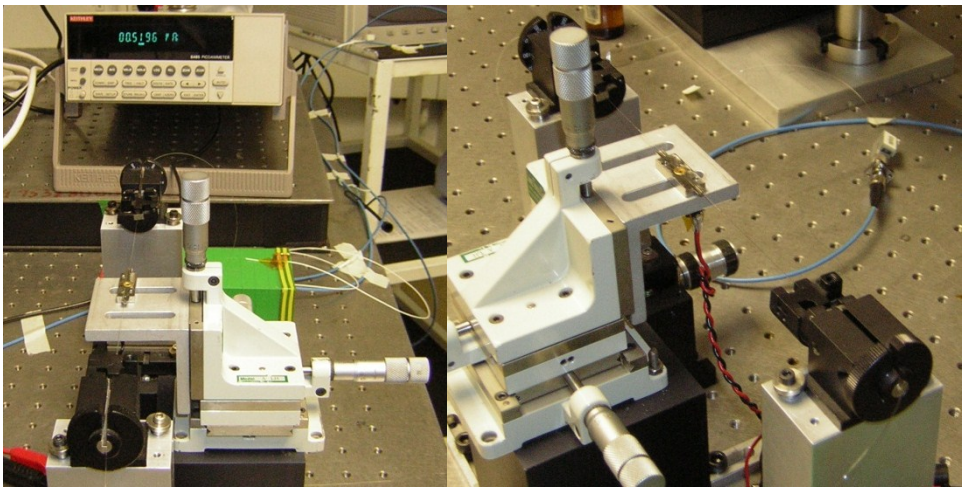

Figure 5-19 showing the detection method using an INGaAs detector, two fibre rotational mounts and a translation stage. Set up arranged by Dr Thomas Butler.

The out coupling signal, as a function of angular rotation, for the two highest inscription energy devices was measured and is displayed in Figure 5-20. A distinct out coupling peak was observed for 10μJ guide, however, no significant out coupling was found for position 9μJ guide.

When the lower inscription energy guides were examined only weak out coupling features were observed for the 3 devices in the fibre. This is partially due to the modification of the cladding not being of sufficient

index change to encourage significant out coupling at the distance from the core that the devices were inscribed at. This could be improved either by increasing the interaction length or decreasing the separation, both of which are the target of future work on devices of this nature.

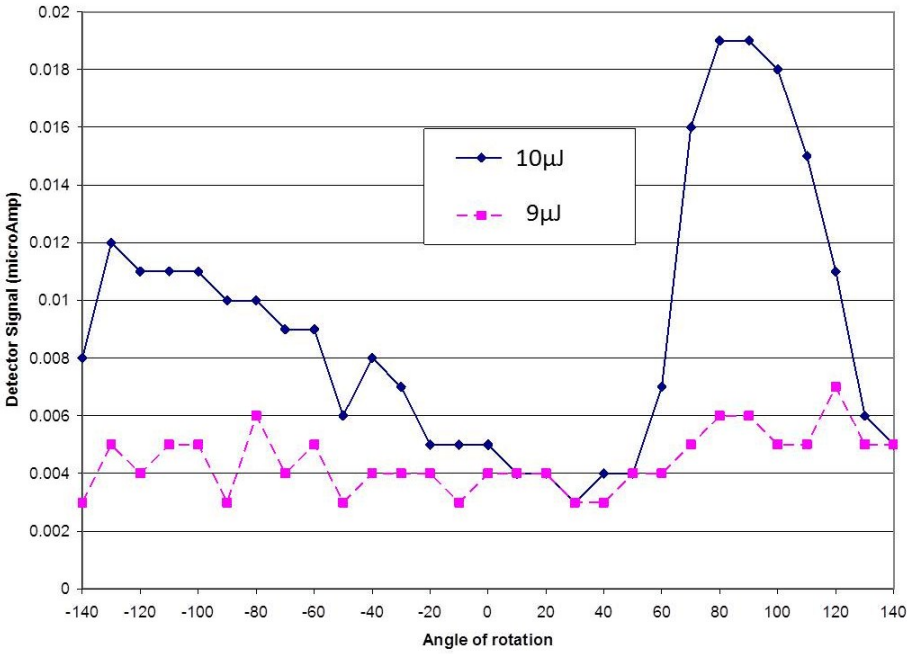

Figure 5-20 Angular distribution of light coupled from two highest inscription energy guides. Data processed with Dr Thomas Butler.

Additional measurements were carried out on the 10µJ guide. The fibre was aligned on the measurement setup as before and the out coupled light measured when the fibre was in air and when immersed in 1.51 refractive index oil. A clear peak was found in the air case, while no coupling was found for the same position in oil. Figure 5-23 shows the out coupling in

air and oil for the device. This is because the index gel creates a loss of guidance from the guides at the cladding-RI gel interface.

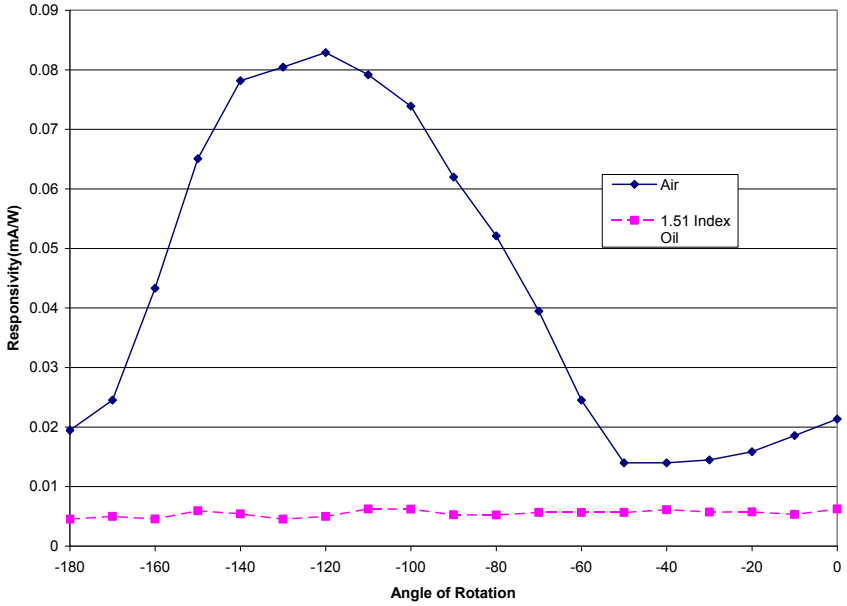

Figure 5-21 Angular distribution of light coupled from position F1-1. Data processed with Dr Thomas Butler.

For comparison purposes the distribution of light from a side-polished fibre designed for power monitoring applications was also measured. The side-polished fibre was aligned over the InGaAs detector and then immersed in 1.51 refractive index oil. The position of the polished region, relative to the active-area of the detector, was optimised for maximum signal. The fibre was then rotated as in the previous case. The output of one of this side-polished device is shown in Figure 5-24 below.

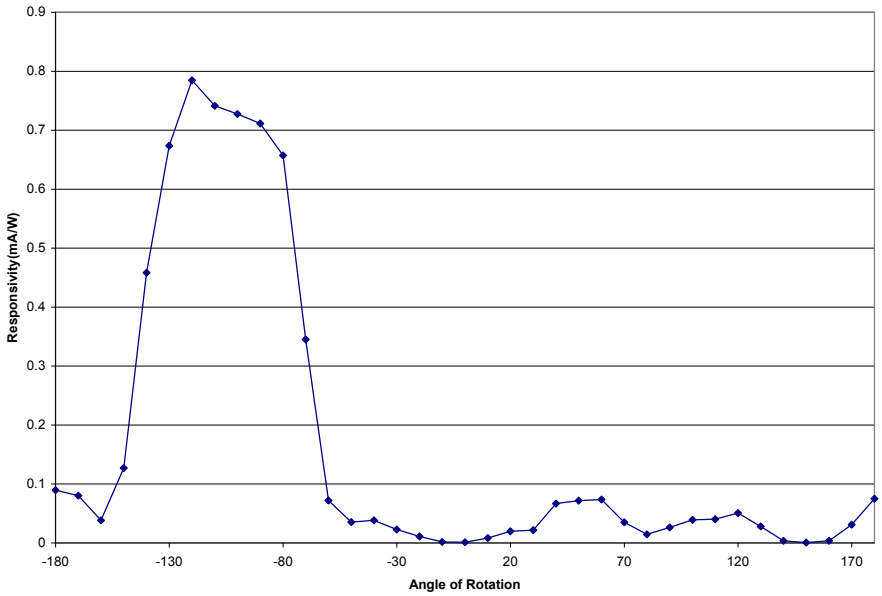

Figure 5-22 Angular distribution of light coupled from side-polished fibre. Data processed with Dr Thomas Butler.

A clear peak was observed which corresponds to the face of the side-polished region being parallel to the face of the detector. The side-polished device has a very similar peak form to the guiding structures inscribed, the advantage being that the general level of scattered radiation is lower. Through further work it is thought that the undesired light escaping from the other rotational position in a femtosecond inscribed device will be reduced. As mentioned earlier this should be possible through creating an increased refractive index profile and through increasing the coupling interaction length. These would serve, when combined with making a smooth slope and guide, to decrease the scattering, bend and other losses believed to be the cause of the higher noise. This technique certainly shows

some promise however and could be improved to enable guides and other photonic devices to be inscribed in fibre.

At this point it a sufficient amount of knowledge, technique and practical experience had been acquired in the inscription and ablation techniques required to work in optical fibres. The decision to combine the two in a single device for the detection of magnetic fields was undertaken and the results of this work are presented in section 5.7 below.

5.7 Magnetic field sensor in an optical fibre using femtosecond ablation and inscription and Terfenol-D

In the work presented here the combination of femtosecond inscription and ablation was combined in a single device in the complex fibre geometry to demonstrate the potential of having both efforts combined to create complex devices. First collaborators at the Cyprus University of Technology inscribed a fibre Bragg grating using inscription techniques discussed earlier, subsequently (but in a single process) the device has a slot removed using femtosecond ablation techniques developed by my previous work in both Cyprus and at Aston University. This is done so that the two overlap one another i.e. the slot exists in the cladding region above the grating in the fibre core. The slot and fibre are back filled and coated with Terfenol-D by collaborators at the University of Plymouth. At this stage the devices were characterised at Aston University by myself and Dr Tom Allsop and the data analysed. The details of this work are discussed more thoroughly here.

The motivation for magnetic sensors are wide ranging from the control and analysis of natural and manmade processes such as current sensing, the measurement of geophysical anomalies and the position sensing of linear and rotary motion. The optically based ones use a range of detection methods including interferometry, Faraday rotation and cantilever arrangements. These cover magnetic fields of 1nT-1T. As mentioned above the device created in this work uses Terfenol-D, as part of a fibre Bragg grating sensor, to form the magnetic field sensor. The wavelength shift is created because of the presence of Terfenol-D, a giant magnetorestrictive alloy, which in the presence of small magnetic fields changes dimensions. Terfenol-D is created through the alloying of Dysprosium, Dy, and Terbium Tb; $DyFe_2$, and $TbFe_2$ has the form $Tb_xDy_{1-x}Fe_2$ (where typically x=0.3) gives the highest known magnetostrictive compound exhibiting approximately 2,000 microstrains in a field of 2 kOe (160 kA/m) at room temperature [**138**]. When operating below the Curie temperature, as in this experiment, the relationship remains linearly proportional between the strain and magnetic field strength.

The concept of integrating magnetostriction and fibre strain sensors was first proposed for the detection of small magnetic fields in 1980 [**139**] and was first achieved in 1983 [**140**]. However, the sensitivity of these sensors improved with the use of FBGs adding to the other advantages of multiplexing, cost, immunity to EM interference and compact spatial requirements, and ability to remotely work in hostile conditions

[**141**,**142**,**143**]. Prior work has concentrated on three techniques for combining the magnetostrictive material and the fibre sensor; bonding, coating and doping [**144**,**145**,**146**]. The mechanisms for detection have been largely focused on interferometer set-ups [**145**,**146**,**147**] although other techniques such as using Faraday rotation and cantilevers have been reported [**144**,**148**,**149**]. Most reported studies were conducted using high frequency magnetic fields or by using mumetal shields leading to practical application issues for detecting either slowly varying or static magnetic fields.

The sensitivity of magnetostrictive fibre sensors has been shown to increase through the removal of the cladding through processes involving chemical etching. This works by reducing the thickness ratio between the fibre and Terfenol-D coating [**150**]. However, the use of chemical processing using HF is often slow and has numerous related health and safety issues. Instead we used the single femtosecond laser processing step to both inscribe a grating and micro-machine a slot. The slot was purposely designed to both increase sensitivity, through a relative increase in the thickness ratio of Terfenol-D to fibre cladding, and through breaking the radial symmetry leading to the sensors vectoral capability. Through choosing Terfenol-D, the most magnetically sensitive material currently available, the device was designed to avoid a number of flaws with the other techniques, i.e. low sensitivity with the Faraday effect and the inefficiency of bonding the fibre to a strip [**151**]. The sputtering carried out by Mr Ronald Neal at Plymouth

allowed the creation of a robust monolithic structure that negates some of the issues regarding bonding.

5.7.1 Fabrication and characterisation

The complete sensor was fabricated using a three step process. Initially a low insertion loss fibre Bragg grating was inscribed by collaborators in Cyprus using the point by point technique, discussed earlier, in Corning single mode fibre-28 using a HighQ femtoRegen laser operating at 1035nm, with pulse duration of 300fs, 1kHz pulse repetition rate focused using a Mitutoyo x50 NIR lens. The lens choice combined the long working distance with a moderate NA creating the small defect sizes required for the inscription of the grating structure. The fibre was suspended between two high precision fibre mounts on an Aerotech air bearing 2D (XY) stage. Once aligned to the centre of the fibre core the stages were translated at a velocity of 1.07mms^{-1} creating 2nd order gratings of 1.07µm pitch over 30mm, which formed a resonant response at close to 1550nm. Figure 5-23 below shows a schematic of the set up used for this write process.

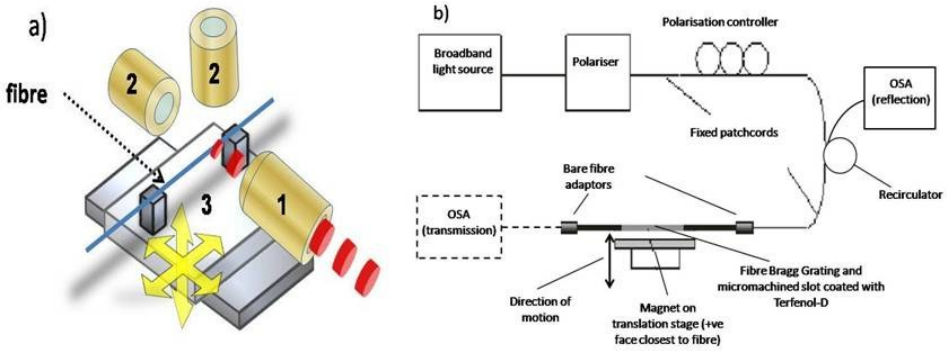

Figure 5-23 a) Schematic of the inscription technique, 1 indicates the position of the 50x objective lens, 2 the vision optics for alignment and 3 the stages used for motion, b) Schematic of the characterisation apparatus for transmission and reflection for one of the vectors' characterisation (the mount being altered for the perpendicular vectors).

The second step was micromachining a slot, using the same set up as above, into the cladding of the fibre in line with the grating region. The plasma focus was brought to the cladding air boundary and through rastering over a set of heights the slot was created using ablation. The energy used was 10μJ and was rastered with the dominant axis along the fibre axis with sequential depth increases towards the fibre core. The grating spectra were monitored actively as the fibre was micromachined. This was done to achieve a repeatable slot depth in controlled manner. The slots machined were up to 30mm long and were fabricated to overlap the region of the FBG.

The third step was the uniform coating of the fibre, which in turn back filled the groove, with Terfenol-D. This was done using a sputter machine and mask. The final device is shown in the schematic in Figure 5-25.

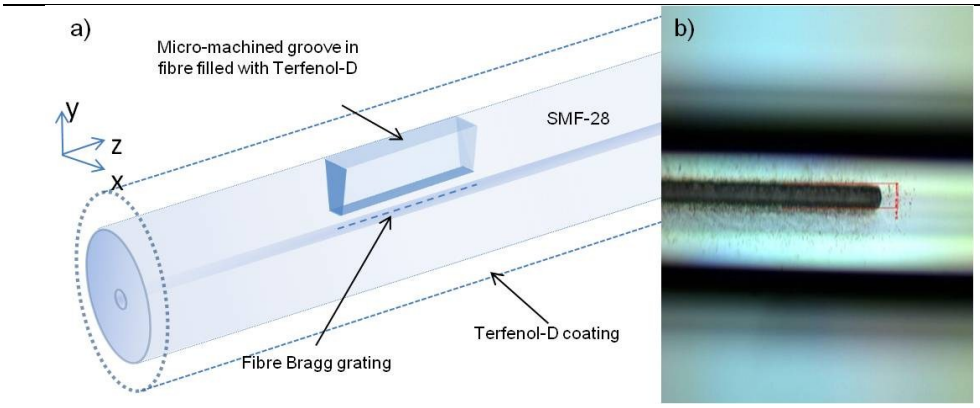

Figure 5-24 a) Schematic of the geometry of the magnetic optical fibre sensor device with smf28 with femtosecond inscribed FBG in the core and micromachined slot which is then back filled and coated with Terfenol-D, b) Microscope image of the slot in the smf28 prior to being filled and coated. Microscope image taken by Dr Kyriacos Kalli.

The interrogation of the sensor went through several iterations including the use of Helmholtz coils and fixed magnets to create the static magnetic field. The final arrangement used strong rare earth fixed magnets as they did not create heat which the DC currents passing through the Helmholtz coils did. This caused variation in the fibre sensor, through cross sensitivity, that was not desired and so the rare earth magnets were chosen. The sensor spectra was characterised in both transmission and reflection under varying magnetic field strengths. The characterisation arrangements are shown in Figure 5-23 above. The thermal sensitivity of the device was characterised using a peltier. This was known to be important from the initial Helmholtz tests. The device was characterised using a broadband light source (ELED) which then passed through a PAT8000B polariser and a polarisation controller and coupler before passing through the device.

The transmission and reflection spectra were monitored using an optical spectrum analyser of resolution 0.005nm.

As mentioned above static magnetic fields were created by fixed magnets mounted on a 3D translation stage which was then translated in micron increments towards and away from the fibre in the 3 directions (x, y, and z) as shown in Figure 5-24 above. At each position the spectra were captured and recorded. The spectra were subsequently analysed using centroid techniques to measure the resonance of each capture. The magnets were calibrated with a Phillips and Harris magnetic flux density meter that has calibration accuracy to within ±0.1 mT. This was used to calibrate the magnets magnetic flux as a function of distance and the results were used to infer the field strength at any given separation, between sensor and magnet, distance.

5.7.2 Experimental Results

The devices were found to have polarisation dependence which was part of the sensor design being geometrically asymmetric. This resulted in a small variation observed in both transmission and reflection spectra. This is demonstrated in Figure 5-25 below. It is important to remember that the polarisation response is relative as the devices were written in standard fibre and not polarisation maintaining ones. Figure 5-25 below shows a typical set of reflection spectra of the complete sensor as a function of varying the polarisation. The figure shows two clear states A and C and a range of intermediate states with B being a good example.

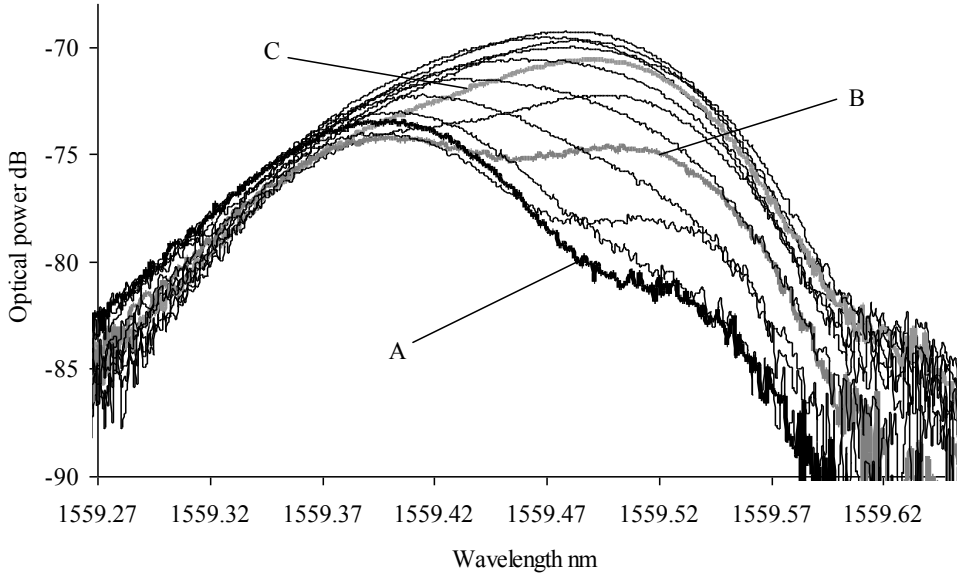

Figure 5-25 Polarisation variation in the reflective spectral response of the sensor (coating thickness 1µm, length of groove and Bragg grating 2cm). Data collected and analysed with Dr Tom Allsop.

Polarisation state A showed little sensitivity and is taken to be the state perpendicular to that of the monolith. State C showed the greatest sensitivity and is considered to be orthogonal to A and thus in line with the monolith structure. State B is believed to be the resultant of states A and C. The dB drop shows that it is likely to be at slightly less or greater than 45° from state C, however, this is expected as the slot and subsequent monolith has physical volume.

The calculated centroid wavelength and optical strength of the device measured in reflection are shown in Figure 5-26 below as the input polarisation is varied. This shows the degree of polarisation dependence on

the devices response, showing a 90° variation between the maximum and minimum. This was anticipated because of the structure of the device with a slot in only a single fibre axis.

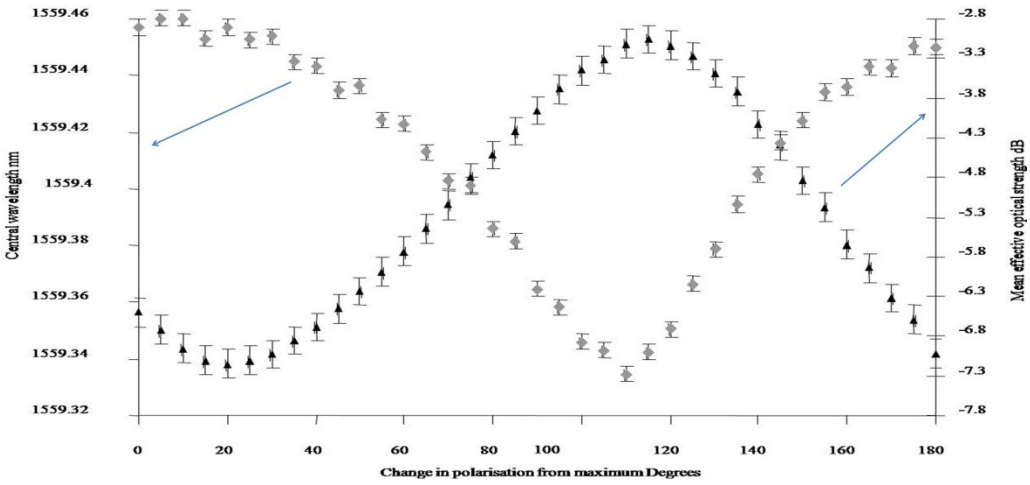

Figure 5-26 The variation in the centroid wavelength and effective optical strength of the reflective spectra as a function of changing polarisation. Data collected and analysed with Dr Tom Allsop.

Having found the polarisation dependence the magnetic field strength effect was investigated in reflection. The device had a coating thickness of 1μm, and a groove and FBG length of 2cm. The two states, B and C, showed magnetic field sensitivity and the other, state A, showed very little response.

The polarisation states B and C yielded sensitivities of 0.1 pm mT^{-1} and 0.2 pm mT^{-1} respectively with obvious strength change, Figure 5-27 below. This was also shown to have a minimum detectable field of around 110mT where below this level the device was not able to clearly measure the field.

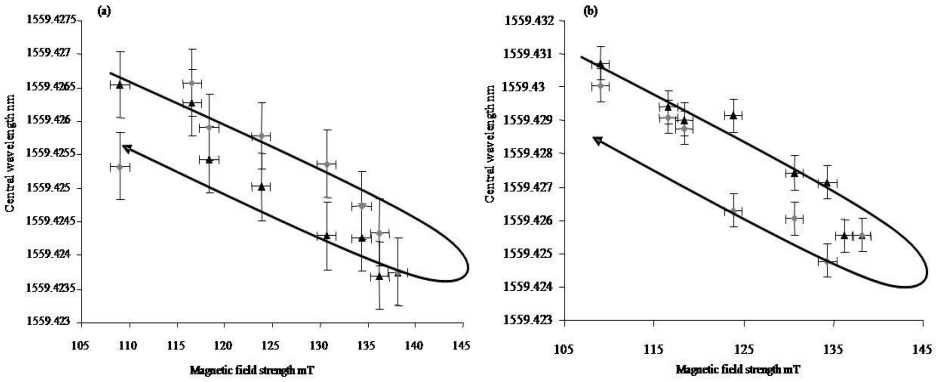

Figure 5-27 The spectral response in reflection of the polarisation states of the optical sensor as a function of magnetic field strength, (a) for polarisation state B, (b) for polarisation state C for increasing field strength (▲) and decreasing field strength (♦).Data collected and analysed with Dr Tom Allsop.

The measurements shown in Figure 5-28 below show results taken in transmission using a device which had a total groove length of 3cm and a Bragg grating of the same length. The sensitivities were measured as being 0.5pm mT^{-1} and 0.3pm mT^{-1}, using a magnet in the orientation shown in Figure 5-24. The increase in sensitivity of this device, measured in transmission, is predicted to be because the increase in device length. This device is actually the same as measured above, however, unfortunately a breakage unrelated to the device fabrication had left almost, but not quite, the complete device length intact. The sensitivity recorded was $\Delta\lambda/\Delta H \sim$ 0.3 pm mT^{-1} with limited hysteresis in a range between 22-32 mT.

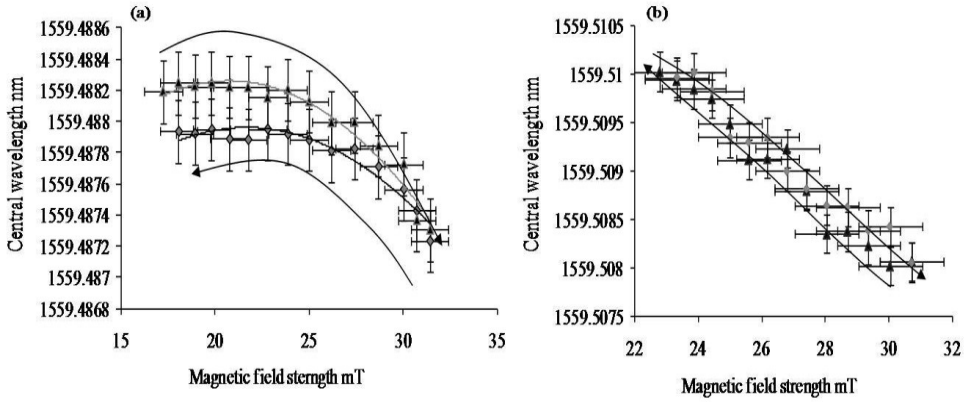

Figure 5-28 The spectral response in reflection of the polarisation states of the optical sensor (coating thickness 1µm, length of groove and Bragg grating 3cm) as a function of magnetic field strength, (a) for polarisation state A, (b) for polarisation state C for increasing field strength (▲) and decreasing field strength (♦).Data collected and analysed with Dr Tom Allsop.

As touched upon before the thermal sensitivity of the device was quite important to be characterised. Taking great care we laid the fibre as straight as possible to avoid polarisation effects in a peltier device. The reflected spectra were recorded at each temperature after stabilisation in 10°C increments between 20-80°C. Through doing this the thermal response was found to be 11.4pm°C^{-1}. The results and processed data are shown in Figure 5-29 below.

Although the sensitivity found is significant this is within the common range for the thermal sensitivity of an FBG in smf28 and was able to be negated in the magnetic sensitivity experiments by maintaining a constant room temperature. There is clear potential for developing a temperature compensated version of the device. This would likely take the form of a

second grating in the fibre without coating or slot at a slightly different wavelength. This could be used as the reference for the temperature dependence and would not be magnetically sensitive.

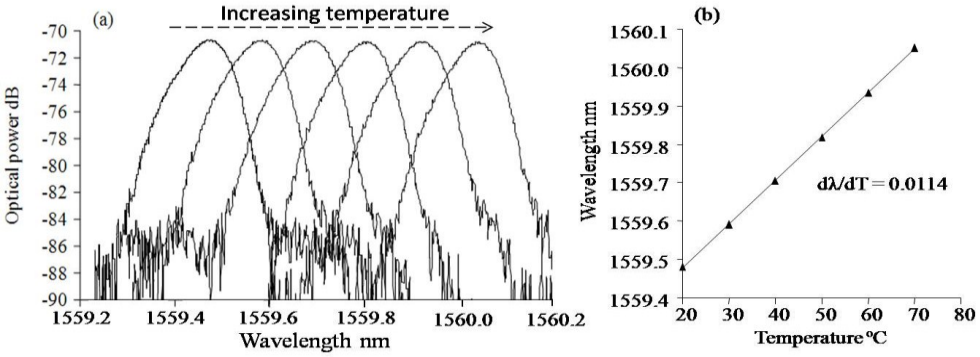

Figure 5-29 The spectral response of the optical sensor as a function of temperature (a) the reflective spectra, (b) spectral sensitivity. Data collected and analysed with Dr Tom Allsop.

5.7.3 Analysis of experimental results

The practicality of the device was critical to its usefulness. The ability to repeatedly measure magnetic field strength with accuracy and precision is vital to this end. The device's spectral characteristics were measured in an insulated and temperature controlled environment, and the stability and resolution were measured. Dr Tom Allsop and I looked specifically at the standard deviation in the wavelength in the device. When this was done a variation of ±0.014pm was seen over a period of 5 minutes. This was considered a result of temperature cycling and thus variation within the peltier device. Through taking the standard FBG thermal response of 1pm per 0.1 ^{o}C change in temperature as a working approximation this would yield the minimum sensitivity threshold for the temperature stabilised 3cm

transmission sensor device with 0.3 pm mT^{-1}, was found to be 0.047 mT. This is greater than the cross-sensitivity between the magnetic and thermal response of the sensor device, which when calculated using the experimental data and material constants from references [100, 116-118] was estimated to be ~3×10^{-3} pm$°C^{-1}T^{-1}$.

When we fitted a linear response to the data of the 3 cm long fibre sensor a residual average error of ±0.12 pm was found. This leads to a resolution limit of ±0.3mT in a magnetic field strength of ~20mT. For the 2cm fibre sensor, working in reflection, a resolution limit of ±0.7mT in magnetic field strengths of ~110mT was observed.

Although the sensor device characteristic exhibits hysteresis it has been shown in other research that this may be accounted for by using algorithms which compensate for the rate independent memory effects. This has been demonstrated to be effective for FBG magnetic strain sensors in improving the accuracy and linearity range of their devices[119]. This type of algorithm could potentially be applied to track the global performance of the device making it more accurate and reliable as a device.

The data presented demonstrates that the response of the sensor is very much dependent upon its separation distance, i.e. field strength, and orientation relative to the magnetic field. This accounts for the differences in sensitivities between the various experiments and shows the expected behaviours of the designed asymmetric sensor geometry.

Whilst this is not as sensitive as some reported results elsewhere, where minimum detectable magnetic fields of 0.10nT $Hz^{-1/2}$ (a measure of the magnetic field bandwidth dependent noise level of the device) and sensitivities of up to 1.08pm mT^{-1} [109, 112] were presented, the asymmetry of the device enables it to be sensitive to the direction of the magnetic field which is highly novel in the case of fibre sensors. The device also does not rely on high frequency AC magnetic fields, multilayer coatings, mumetals or expensive Fabry-Perot filters to be operational. The laser fabrication process and subsequent filling of the machined slot means it is also mechanically stronger than the chemically etched fibres and the devices could be easily multiplexed, which with other interrogation systems can prove problematic, with gratings at different wavelengths for distributed monitoring. The results are more sensitive than the Faraday rotation devices which have similar levels of simplicity in their optical configuration which have been shown to measure fields from 0.02-3.2T[106].

5.7.4 Conclusion

The work presented here represents a magnetic field sensor based on a single layer magnetostrictive film of Terfenol-D. This was sputtered onto a single mode fibre that had been processed using femtosecond inscription and ablation techniques developed in earlier work in collaboration with Dr Kyriacos Kalli in Cyprus. The device had a minimum detection limit of 0.047mT and a sensitivity of 0.3pm mT^{-1} when measured in transmission, with a resolution limit of ±0.3mT in a magnetic field strength of ~20mT. The sensor was also able to demonstrate the potential for vectoral field

sensing capability which no other fibre device has shown. The simplicity of the optical configuration and preliminary results show the vast potential for the technique to be adapted and used in a range of fields with the small sensor size and potential for remote interrogation. There is also room for the vectoral magnetic field sensing with the levels of sensitivity achieved to be varied in a fairly flexible way to develop further the device.

The device was shown to have sensitivity to magnetic field of 0.3 pm mT^{-1} in transmission and 0.2 pm mT^{-1} and 0.1 pm mT^{-1} for different polarisation states in reflection and a thermal sensitivity of 11.4pm$^{o}C^{-1}$. These results show the device has the potential for use as a vectoral sensor for the detection of magnetic fields as low as 0.046 mT with a resolution of ±0.3mT in transmission and ±0.7mT in reflection.

An important feature of this work is that it significantly simplifies the fabrication of the sensing devices by using one laser to create the FBG and micromachined slot. This combines a great deal of the techniques built up through the course of the research and forms a device showing some of the potential that the unique capabilities of femtosecond inscription and ablation offer to form an otherwise multi instrument fabrication process device.

5.8 Conclusions on work in optical fibre

The work in this chapter has demonstrated technical advances in femtosecond inscription and ablation techniques that have enabled the physical interactions between pulse and material to be examined in the

LPG annealing experiments, the ability to create directional couplers and power detectors without using side polishing techniques through both ablation and inscription, and finally combining them to create a practical device for remotely measuring the static magnetic field strength. This work has demonstrated the potential for a range of sensing, telecoms and other devices to be created using femtosecond lasers to process optical fibres. With the further development of inscription techniques and the refinement of the surface smoothing the potential for complicated yet elegant devices is clear to see.

6 Conclusion

The initial motivation of the work was broadly to examine femtosecond micromachining and inscription and develop techniques to further them both. Whilst this covered a broad spectrum it soon became apparent that the work should commence with micromachining of planar samples. The progression to the investigation of inscription originated from the desire to be able to combine both inscription and ablation in the one device. Although this did not occur in planar, this eventually came to being in the domain of the optical fibre. Through work in developing techniques in micromachining, inscription and to overcome the challenges of the fibre geometry led to their combination in a single device fabricated to detect the magnetic field strength using a detectable shift in wavelength from a PbP femtosecond FBG with micromachined slot.

The work demonstrated in this thesis has shown a number of key achievements in a range of areas including: the production of the first OCT phantom calibration artefact using femtosecond lasers; the first demonstration of the creation of femtosecond written phase masks which

enabled both surface and sub-surface masks to be fabricated; the development of chemical sensing preforms which allowed for rapid development of ideas and artefacts of high quality; the production of the first transparent centrifugal blood pump for the study of the Couette flow of blood in ventricle assist devices; the development of several fibre optic devices including a vectorally sensitive magnetic field sensor; the development of micro-structured machining techniques which hold the potential to create a range of desired shapes.

The work has progressed from initial trials with planar substrates in a range of materials to focus on transparent materials. It has shown development of machine control techniques to fabricate complex structures both in micromachining and inscription leading to several novel artefacts and beginning to find the solutions to some key issues in photonics, Biology and Chemistry through facilitating other research with the artefacts that have been produced.

There are, however, a number of challenges in advancing the many projects presented here before they can truly become taken on board. The most obvious of these is the issue of surface roughness. Whilst I have tried, through refinement of fabrication and preparation techniques to reduce the surface roughness at the bottom surface, the issue still remains even if reduced. It would appear that it is not, at least as yet, physically possible to micromachine with a largely athermal mechanism and leave smooth surfaces. The techniques employed by high powered laser specialists of soft

focusing simply do not work as the non-linear absorption requires focusing of the pulses, resulting in fine modification areas. I fully believe that the re-flowing results that are coming from initial trials being conducted in current work are likely to solve this issue enabling the liquid surface to form optically smooth surfaces with the shape of the machining defined by the work of the femtosecond laser system.

The next biggest challenge is the uniformity and reliability of the inscription process. The variations along a given line will need to be made more reproducible if the work on OCT and sub-surface phase masks will really endure as a meaningful contribution. I consider this may be addressed in a few ways. The first is to explore the fictive temperature models using links with glass manufacturers and use these to increase the uniformity and amount of index change seen during femtosecond inscription. The next is to use repeated overpasses until saturation of index change has been achieved. It has been suggested that 8 passes should result in a larger index change in fused silica for example. The next is to slow the stages down and fine tune them to deal with this. In doing this I would expect the pulse to pulse variations seen to become negligible.

There are several other areas of improvement that would be required such as sample surface location relative to any given objective, adaptive aberration control to correct for the effects of RI mismatch with non-oil – immersion objective lenses and several more.

Through the improvement of some or all of these I would hope that the results demonstrated here showing proof of principle over a range of topics may be finessed and improved upon to be of full use within the photonics community.

References

[1] M. Terazima, Y. Shimotsuma, K. Miura, and K. Hirao. M. Sakakura, "Observation of pressure wave generated by focusing a femtosecond laser pulse inside glass," *Optics Express, vol 15*, p. 5674, 2007.

[2] K. Saito, and A. J. Ikushima. H. Kakiuchida, "Refractive Index, Density and polarizability of Silica Glass with Various Fictive Temperatures," vol. 43, pg 743, 2004.

[3] A. Politi, J. C. F. Matthews, P. Dekker, M. Ams, M. J. Withford, J.L. O'Brien G. D. Marshall, "Laer written waveguide photonic quantum circuits," vol. 17, 12546, 2009.

[4] J. F. Schroeder, and A. M. Streltsov C.W. Ponader, "Origin of the refractive-index increase in laser-written waveguides in glasses," vol. 103, 2008.

[5] A Brodeur, E Mazur C B Schaffer, "Laser-induced breakdown and damage in bulk transparent materials induced by tightly focused femtosecond laser pulses," vol. 12, no. 11, 2001.

[6] K. Sokolowski-Tinten, P. Zhou, A. El-Khamhawy, D. von der Linde V. V. Temnov, "Multiphoton Ionization in Dielectrics: Comparison of Circular and Linear Polarizations," vol. 97, 2006.

[7] C. DeMichelis, "Laser Induced Gas Breakdown: A Bibliographical Review," vol. QE-5, no. 188, 1969.

[8] B. Rethfeld, M. Vicanek, and G. Simon, A. Kaiser, "Microscopic processes in dielectrics under irradiation by subpicosecond laser pulses," *Physical Review B*, vol. 61 (17), no. 11, pp. 437-11, 450, 2000.

[9] J. Kruger, S. Sartania, Z. Cheng, C. Spielmann, G. Mourou, W. Kautek, and F. Krausz M. Lenzner, "Femtosecond optical breakdown in dielectrics," *Physical Review Letters*, vol. 80, no. 18, pp. 4076-4079, 1998.

[10] M. D. Feit, S. Herman, A. M. Rubenchik, B. W. Shore, and M. D. Perry B. C. Stuart, "Optical ablation by high-power short-pulse lasers," *Journal of the Optical Society of America B-Optical Physics*, vol. 13, no. 2, pp. 459-468, 1996.

[11] M. D. Feit, S. Herman, A. M. Rubenchik, B.W. Shore, M. D. Perry B. C. Stuart, "Nanosecond-to-femtosecond laser-induced breakdown in dielectrics," vol. 53, no. 4, 1996.

[12] T. R. Huser, S. H. Risbud, J. S. Hayden, and D. M. Krol J. W. Chan, "Waveguide fabrication in phosphate glasses using femtosecond laser pulses," vol. 82, no. 15, 2003.

[13] T. Huser, S. Risbud, and D. M. Krol, J. W. Chan, "Structural changes in fused silica after exposure to focused femtosecond laser pulses,"

vol. 26, no. 2, 2001.

[14] T. R. Huser, S. H. Risbud, and D. M. Krol J. W. Chan, "Modification of the fused silica glass network associated with waveguide fabrication using femtosecond laser pulses," vol. 76, no. 3, 2003.

[15] R. Bruckner, "Properties and structure of vitreous silica. I," vol. 5, no. 2, 1970.

[16] R. Bruckner, "Properties and structure of vitreous silica. II," vol. 5, no. 3, 1971.

[17] O. Humbach, S. Ortner, and H. Fabian U. Haken, "Refractive index of silica glass: influence of fictive temperature," vol. 265, no. 1-2, 2000.

[18] S.Wielandy, A. L. Gaeta, N. F. Borrelli, and C. Smith, D. Homoelle, "Infrared photosensitivity in silica glasses exposed to femtosecond laser pulses," vol. 24, no. 18, 1999.

[19] S. Nolte, B. N. Chichkov, and A. Tunnermann, M. Will, "Optical properties of waveguides fabricated in fused silica by femtosecond laser pulses," vol. 41, no. 21, 2002.

[20] A. M. Streltsov and N. F. Borrelli, "Study of femtosecond-laser-written waveguides in glasses," vol. 19, no. 10, 2002.

[21] K. Miura, N. Sugimoto, and K. Hirao, K. M. Davis, "Writing waveguides in glass with a femtosecond laser," vol. 21, no. 21, 1996.

[22] T. R. Huser, S. H. Risbud, J. S. Hayden, and D. M. Krol J. W. Chan, "Waveguide fabrication in phosphate glasses using femtosecond laser pulses," vol. 82, no. 15, 2003.

[23] A. M. Streltsov and N. F. Borrelli, "Study of femtosecond laser written waveguides in glasses," vol. 19, no. 10, 2002.

[24] K. Hirao and K. Miura, "Writing waveguides in silica-related glasses with femtosecond laser," vol. 37, 1998.

[25] L. B. Glebov, K. A. Richardson, E. Van Stryland, T. Cardinal, S. H. Park, M. Couzi, and J. L. Bruneel, O. M. Efimov, "Waveguide writing in chalcogenide glasses by a train of femtosecond laser pulses," vol. 17, no. 3, 2001.

[26] A. M. Streltsov and N. F. Borrelli, "Study of femtosecond-laser written waveguides in glasses," vol. 19, no. 10, 2002.

[27] B. Poumellec and M. Lancry, "Damage thresholds in femtosecond laser processing of silica based materials," 2006.

[28] A. Pasquarello and R. Car, "Identification of Raman defect lines as signatures of ring structures in vitreous silica," vol. 80, no. 23, 1998.

[29] M. J. Caturla, J. S. Stolken, and M. D. Feit A. Kubota, "Densification of fused silica due to shock waves and its implications for 351nm laser induced damage," vol. 8, no. 11, 2001.

[30] F. L. Galeener, "Planar rings in glasses," vol. 44, no. 7, 1982.

[31] F. L. Galeener, "Planar rings in vitreous silica," vol. 49, no. 1-3, 1982.

[32] R. A. Barrio, E. Martinez, and R. J. Elliott, F. L. Galeener, "Vibrational Decoupling of Rings in Amorphous Solids," vol. 53, no. 25, 1984.

[33] M. Milosavljevic, L. Huang, R. J. Finlay, T. H. Her, J. P. Callan, E.

Mazur E. N. Glezer, "Three-dimensional optical storage inside transparent materials," vol. 21, no. 24, 1996.

[34] E. N. Glezer and E. Mazur, "Ultrafast-laser driven micro-explosions in transparent materials," vol. 71, no. 7, 1997.

[35] A. O. Jamison, and E. Mazur, C. B. Schaffer, "Morphology of femtosecond laser-induced structural changes in bulk transparent materials," vol. 8, no. 9, 2004.

[36] M. Will, S. Nolte, A. Tuennermann, and U. Glatzel T. Gorelik, "Transmission electron microscopy studies of femtosecond laser induced modifications in quartz," vol. 76, no. 4, 2003.

[37] W. H. Zachariasen., "The atomic arrangement in glass," vol. 5, no. 23, 1932.

[38] G. D. Marshall, D. J. Spence, and M. J. Withford. M. Ams, "Slit beam-shaping method for femtosecond laser direct-write fabrication of symmetric waveguides in bulk glasses," vol. 13, 2005.

[39] R. M. Kogan, and E. J. Robinson. R. A. Fox, "Laser Triple-quantum photoionization of Cesium," vol. 26, 1971.

[40] P. Lambropoulos., "Effect of Light Polarization on Multiphoton Ionization of Atoms," vol. 28, 1972.

[41] S. Klarsfield and A. Maquet, "Circular versus Linear Polarization in Multiphoton Ionization," vol. 29, 1972.

[42] H. R. Reiss., "Polarization effects in High-Order Multiphoton Ionization," vol. 29, 1972.

[43] D. D. Venable and R. B. Kay., "Polarization effects in four-photon conductivity in quartz," vol. 27, 1975.

[44] H. S. Carman and R. N. Compton., "High-Order Multiphoton Ionization Photoelectron-Spectroscopy of Nitric-Oxide," vol. 90, 1989.

[45] G. D.Marshall, and M. J.Withford. M. Ams, "Study of the influence of femtosecond laser polarisation on direct writing of waveguides," vol. 14, 2006.

[46] E. Gaizauskas, and V. Sirutkaitis V. Kudriasov, "Beam transformation and permanent modification in fused silica induce by femtosecond filaments," vol. 22, no. 12, 2005.

[47] H. B. Jiang, L. Luo, H. C. Guo, H. Yang, and Q. H. Gong Z. X.Wu, "Multiple foci and a long filament observed with focused femtosecond pulse propogation in fused silica," vol. 27, no. 6, 2002.

[48] A. Couairon, M. Franco, B. Lamouroux, B. Prade, S. Tzortzakis, and A. Mysyrowicz L. Sudrie, "Femtosecond laser-induced damage and filamentary propogation in fused silica," vol. 89, no. 18, 2002.

[49] A. Brodeur, S. Petit, O. G. Kosareva, and V. P. Kandidov S. L. Chin, "Filamentation and supercontinuum generation during the propagation of powerful ultrashort laser pulses in optical media (white light laser)," vol. 8, no. 1, 1999.

[50] H. B. Jiang, H. Yang, and Q. H. Gong Z. X. Wu, "The refocusing behaviour of a focused femtosecond laser pulse in fused silica," vol. 5, no. 2, 2008.

[51] A. Brodeur and S. L. Chin, "Band-gap dependence of the ultrafast white-light continuum," vol. 80, no. 20, 1998.

[52] A. Brodeur and S. L. Chin, "Ultrafast white-light continuum generation and self-focusing in transparent condensed media," vol. 16, no. 4, 1999.

[53] A. Couairon, "Dynamics of femtosecond filamentation from saturation of selffocusing laser pulses," vol. 68, no. 1, 2003.

[54] L. Sudrie, M. Franco, B. Prade, and A. Mysyrowicz, A. Couairon, "Filamentation and damage in fused silica induced by tightly focused femtosecond laser pulses," vol. 71, no. 12, 2005.

[55] O. Kosareva, I. S. Golubtsov, A. Iwasaki, A. Becker, V. P. Kandidov, and S. L. Chin W. Liu, "Random deflection of the white light beam during self-focusing and filamentation of a femtosecond laser pulse in water," vol. 75, no. 4-5, 2002.

[56] M. D. Feit, A. M. Rubenchik, B. W. Shore, and M. D. Perry B. C. Stuart, "Laser-induced damage in dielectrics with nanosecond to subpicosecond pulses," vol. 74, no. 12, 1995.

[57] S. K. Sundaram and E. Mazur, "Inducing and probing non-thermal transitions in semiconductors using femtosecond laser pulses," vol. 1, 2002.

[58] P. Mannion, J. Magee, E. Coyne, and G.M O'Connor, "Ablation thresholds and feature quality in ultrafast laser micro-machining of common metals in air," 2002.

[59] K. Nagashima, M. Hashida, M. Katto, M. Tsukamoto, and M. &

Izawa, Y. Fujita, "Femtosecond laser ablation of Al2O3 ceramics," vol. 124, 2004.

[60] T.V. Kononenko et al., "Microstructuring of diamond bulk by IR femtosecond laser pulses," vol. 90, 2008.

[61] S. Baudach, J. Bonse, and W. Krüger J. & Kautek, "Baudach, S.; Bonse, J.; Krüger J. & Kautek, Ultrashort pulse laser ablation of polycarbonate and polymethylmethacrylate," vol. 555, 2000.

[62] G. Olivié et al., "Wavelength dependence of femtosecond laser ablation threshold of corneal stroma," vol. 16, 2008.

[63] J. & Na, S. Kim, "Metal thin film ablation with femtosecond pulsed laser," vol. 39, no. 7, 2007.

[64] A. Baum et al., "NUV and NIR Femtosecond Laser Modification of PMMA," 2007.

[65] J. Kruger, D. Dufft, and R. & Hertwig, A. Koter, "Femtosecond laser-induced damage of gold films," 2007.

[66] J.S. Yahng and J.R. & Jeoung, S.C. Nam, "The influence of substrate temperature on femtosecond laser micro-processing of silicon, stainless steel and glass," vol. 47, no. 7-8, 2009.

[67] N. Sanner et al., "Measurement of femtosecond laser-induced damage and ablation thresholds in dielectrics," vol. 94, no. 4, 2009.

[68] H. Zhang, P. Herman, F. Yoshino, L. Shah, J. Bovatsek, and A. Arai S. Eaton, ""Heat accumulation effects in femtosecond laser-written waveguides with variable repetition rate," vol. 13, 2005.

[69] J. F. García, and E. Mazur C. B. Schaffer, "Bulk heating of transparent materials using a high-repetition-rate femtosecond lase," vol. 76, 2003.

[70] N. H. Mack, S. K. Doorn, and E. Mazur E. D. Diebold, "Femtosecond Laser-Nanostructured Substrates for Surface-Enhanced Raman Scattering," vol. 25, 2009.

[71] R. Le Harzic, N. Huot, E. Audouard, and R. Fortunier S. Valette, "2D calculations of the thermal effects due to femtosecond laser-metal interaction," vol. 247, 2005.

[72] V. Mezentsev, H. Schmitz, and I. Bennion J. Petrovic, "Model of the femtosecond laser inscription by a single pulse," vol. 39, 2007.

[73] H. Jiang, Y. Liu, Z. Wu, H. Yang, and Q. Gong Q. Sun, "Measurement of the collision time of dense electronic plasma inducedby a femtosecond laser in fused silica," vol. 30, 2005.

[74] M. Dubov, I. Khrushchev, and I. Bennion A. Martinez, "Structure of Fiber Gratings Directly Written by Infrared Femtosecond Laser," 2006.

[75] A. Saliminia, S. L. Chin, and R. Vallée N. T. Nguyen, "Control of femtosecond laser written waveguides in silica glass," vol. 85, 2006.

[76] E. N. Glezer & E. Mazur, "Ultrafast-laser driven micro-explosions in transparent materials," vol. 71, 1997.

[77] L. V. Keldysh, , vol. 20, no. 1307.

[78] D. P. Hand and P. St. J. Russell, , vol. 15, no. 202, 1990.

[79] M. Harurnoto et al, "Gain-flattening filter using long-period fiber gratings," vol. 20, no. 6, 2002.

[80] A. M. Vengsarkar et al, "Long-period fiber Bragg gratings as band-rejection filters," vol. 14, no. 1, 1996.

[81] ""ISO Standard 11146," in Lasers and laser-related equipment – Test methods for laser beam widths, divergence angles and beam propagation ratios," 2005.

[82] S. V. Marchese, S. Hashimoto, C. R. E. Baer, G. Gingras, B. Witzel, and U. Keller, T. Sudmeyer, "Femtosecond laser oscillators for high-field science," vol. 2, 2008.

[83] C. G. Durfee Iii, M. M. Murnane, and H. C. Kapteyn, S. Backus, "High power ultrafast lasers," vol. 69, 1998.

[84] D. N. Payne, and M. E. Fermann S. B. Poole, "Fabrication of low-loss optical fibres containing rare-earth ions," vol. 21, 1985.

[85] ed. P. Smid, *CNC Programming Techniques: An Insider's Guide to Effective Methods and Applications*.: Industrial Press Inc, USA, 2006, 2006.

[86] Z. Haibin, M. E. Shane, and R. H. Peter, L. Jianzhao, "5-D Spectroscopic Microscopy for Intelligent Femtosecond Laser Writing of Optical Waveguides," 2008.

[87] Y. Hanada, and K. Midorikawa K. Sugioka, "3D integration of microcomponents in a single glass chip by femtosecond laser direct writing for biochemical analysis," vol. 253, 2007.

[88] K. Zhou, L. Zhang, and I. Bennion Y. Lai, "Microchannels in

conventional single-mode fibers," vol. 31, no. 17, 2006.

[89] K. Yamasaki, V. Mizeikis, S. Matsuo, and H. Misawa, S. Juodkazis, "Formation of embedded patterns in glasses using femtosecond irradiation," vol. 79, 2004.

[90] D.Day and M.Gu, "Microchannel fabrication in PMMA based on localized heating by nanojoule high repetition rate femtosecond pulses," vol. 13, no. 16, 2005.

[91] Y.Hanada, K.Midorikawa K.Sugioka, "3D integration of microcomponents in a single glass chip by femtosecond laser direct writing for biochemical analysis," vol. 253, 2007.

[92] R.S.Taylor, R.Bhardwaj, E.Simova, D.M.Rayner and P.B.Corkum, C.Hnatovsky, "3D Fabrication of Microfluidic Channels in Fused Silica Using Focused Femtosecond Laser Beams and Selective Chemical Etching," 2005.

[93] K.Seong, A.Schülzgen, P.Khulbe, N.Peyghambarian and M.Mansuripur M.S.Giridhar, "Femtosecond pulsed laser micromachining of glass substrates with application to microfluidic devices," vol. 43, no. 23, 2004.

[94] F.He, Z.Zhou, Y.Cheng, Z.Xu, K.Sugioka, K.Midorikawa, H.Sun, "Fabrication of microfluidic optical waveguides on glass with femtosecond laser pulses," vol. 32, no. 11, 2007.

[95] C.L.Callender, C.J.Ledderhof and J.P.Noad P.Dumais, "Monolighic integration of microfluidic channels, liquid-core waveguides, and silica waveguides on silicon," vol. 45, no. 36, 2006.

[96] M.Dugan, P.Bado, Y.Bellouard, A.Scott and J.R.Mabesa, Jr. A.A.Said, "Manufacturing by laser direct-write of three dimensional devices containing optical and microfluidic networks," 2004.

[97] M.Gu, D.Day, "Femtosecond fabricated photomasks for fabrication of microfluidic devices," vol. 14, no. 22, 2006.

[98] L. Su and S. R. Elliott, , vol. 35, no. 1212, 2010.

[99] M.K., Zhang, N., Tansley, G.D. & Woodard, J.C. Chung, "Impeller Behaviour and Displacement of the VentrAssist Implantable Rotary Blood Pump," vol. 28, no. 3, 2004.

[100] D. C. J. Reid, C. J. Rowe, and W. J. Stewart, I. Bennion, "High-reflectivity monomode-fibre grating filters," vol. 22, 1986.

[101] W. W. Morey, and W. H. Glenn G. Meltz, "Formation of Bragg gratings in optical fibers by a transverse holographic method," vol. 14, 1989.

[102] B. Malo, F. Bilodeau, D. C. Johnson, and J. Albert K. O. Hill, "Bragg gratings fabricated in monomode photosensitive optical fiber by UV exposure through a phase mask," vol. 62, 1993.

[103] S. Theriault, F. Bilodeau, D. C. Johnson, K. O. Hill, P. Sixt, and M. J. Rooks J. Albert, "Minimization of phase errors in long fiber Bragg grating phase masks made using electron beam lithography," vol. 8, 1996.

[104] S. J. Mihailov and M. C. Gower, "Recording of efficient high-order Bragg reflectors in optical fibres by mask image projection and single pulse exposure with an excimer laser," vol. 30, 1994.

[105] "Data Sheet from Ibsen Photonics,".

[106] R. J. Farley, and R. Giedl, P. E. Dyer, "Analysis of grating formation with excimer laser irradiated phase masks," vol. 115, 1995.

[107] G. D. Peng, B. Wu, and P. L. Chu Z. Xiong, "Effects of the Zeroth-Order Diffraction of a Phase Mask on Bragg Gratings," vol. 17, 1999.

[108] M. Ams, "Fabrication of Optical Waveguide Devices in Bulk Materials using Femtosecond Laser Pulses, PhD Thesis, Macquarie University," 2008.

[109] Rimas Juškaitis, Martin J. Booth, Tony Wilson, Tomokazu Tanaka, and Satoshi Kawata Mark A. A. Neil, "Active aberation correction for the writing of three-dimensional optical memory devices," vol. 41, no. 7, 2002.

[110] M Booth, T Tanaka, T Wilson, S Kawata M Schwertner, "Spherical aberration correction system using an adative optics deformable mirror," vol. 263, no. 2, 2006.

[111] P. H. Tomlins and R. K. Wang, "Theory, developments and applications of optical coherence tomography," vol. 38, 2005.

[112] J. A. Izatt, E. A. Swanson, D. Huang, J. S. Schuman, C. P. Lin, C. A. Puliafito, and J. G. Fujimoto M. R. Hee, "Optical coherence tomography of the human retina," 1995.

[113] H. C. Lee, C. W. Lu, Y. M. Wang, C. K. Lee, C. C. Yang, and C. P. Chiang M. T. Tsai, "Delineation of an oral cancer lesion with swept-source optical coherence tomography," vol. 13, no. 4, 2008.

[114] ""COUNCIL DIRECTIVE 93/42/EEC of 14 June 1993 concerning

medical devices," http://eur-lex.europa.eu/LexUriServ/LexUriServ.do?uri=CELEX:31993L0042:en:HTML.,".

[115] M. Cheng, "Medical Device Regulations: Global overview and guiding principles," 2003.

[116] S. Huang, A. W. H. Lin, M. H. Lee, J. K. Barton, R. A. Drezek, and T. J. Pfefer A. Agrawal, "Quantitative evaluation of optical coherence tomography signal enhancement with gold nanoshells," 2006.

[117] and M. S. Patterson, B. W. Pogue, "Review of tissue simulating phantoms for optical spectroscopy, imaging and dosimetry," vol. 11, 2006.

[118] J. M. Schmitt and A. Knu, "Model of optical coherence tomography of heterogeneous tissue," vol. 14, 1997.

[119] P. Meemon, K. S. Lee, W. P. Kuhn, K. P. Thompson, and J. P. Rolland S. Murali, "Assessment of a liquid lens enabled in vivo opitcal coherence microscope," 2010.

[120] R. A. Ferguson, C. Hart, and P. D. Woolliams P. H. Tomlins, "Point-Spread Function Phantoms for Optical Coherence Tomography," 2009.

[121] D. L. Marks, F. Kamalabadi, and S. A. Boppart T. S. Ralston, "Deconvolutoins methods for mitigation of transversal blurring in optical coherence tomography," vol. 14, 2006.

[122] R. A. Ferguson, C. Hart, A. Grimwood, and P. H. Tomlins P. D. Woolliams, "Spatially deconvolved optical coherence tomography,"

vol. 49, no. 11, 2010.

[123] J. M. Schmitt and A. Knu, "Model of optical coherence tomography of heterogeneous tissue," 14, 1997.

[124] K. O. Hill, F. Bilodeau, D. C. Johnson, and J. Albert, B. Malo, , vol. 29, no. 1668, 1993.

[125] Y. Lai, M. Dubov, I. Y. Khrushchev, and I. Bennion A. Martinez, , vol. 41, no. 472, 2005.

[126] M. Åslund, A. Fuerbach, S. D. Jackson, G. D. Marshall, M. J. Withford N. Jovanovic, , vol. 32, no. 2804, 2007.

[127] N. Jovanovic, G. D. Marshall, and M. J. Withford R. J. Williams, , vol. 18, 2010.

[128] Graham N., Allsop, Thomas D.P., Kalli, Kyriacos, Koutsides, C., Neal, Ron, Sugden, Kate, Culverhouse, P. and Bennion, Ian Smith, "Characterisation and performance of a Terfenol-D coated femtosecond laser inscribed optical fibre Bragg sensor with a laser ablated microslot for the detection of static magnetic fields," vol. 19, no. 1, 2011.

[129] M. Dubov, I. Khrushchev, and I. Bennion, A. Martinez, , vol. 40, no. 1170.

[130] R. J. Williams, N. Jovanovic, M. J. Steel, and M. J. Withford G. D. Marshall, , vol. 18, no. 19844, 2010.

[131] I. Y. Khrushchev, and I. Bennion, A. Martinez, , vol. 41, no. 176.

[132] 1, Christian Voigtländer, Graham D. Marshall, Andreas

Tünnermann, Stefan Nolte, M. J. Steel and Michael J. Withford Robert J. Williams, "Point-by-point inscription of apodized fiber Bragg gratings," vol. 36, no. 15, 2011.

[133] K. Morishita and Y. Miyake, "Fabrication and Resonance Wavelengths of Long-Period Gratings Written in a Pure-Silica Photonic Crystal Fiber by the Glass Structure Change," vol. 22, 2004.

[134] H. Dobb, V. K. Mezentsev, K. Kalli, D. J. Webb, and I. Bennion J. S. Petrovic, "Sensitivity of LPGs in PCFs Fabricated by an Electric Arc to Temperature, Strain, and External Refractive Index," vol. 25, 2007.

[135] K. Kalli, K. Zhou, M. Dubov, Y. Lai, D. J. Webb, and I. Bennion T. Allsop, "Annealing and spectral characteristics of femtosecond laser inscribed long period gratings written into a photonic crystal fibre," 2008.

[136] M. Dubov, H. Dobb, A. Main, A. Martinez, K. Kalli, D. J. Webb, and I. Bennion T. Allsop, "A comparison of the spectral properties of high temperature annealed long-period gratings inscribed by fs laser, UV, and fusion-arc," 2006.

[137] K. Kalli, and K. Sugden G. N. Smith, "Advances in femtosecond micromaching and inscription of micro and nano photonic devices," in *Frontiers in Guided Wave Optics and Optoelectronics*.: InTech, 2010.

[138] A. E. Clark, *Ferromagnetic Materials, Vol. 1.*: North Holland, 1986.

[139] A. Yariv and H. V. Winsor, "Proposal for detection of magnetic fields through magnetostrictive perturbation of optical fibers," vol.

5, 1980.

[140] J. P. Willson and R. E. Jones, "Magnetostrictive fiber-optic sensor system for detecting dc magnetic fields," vol. 8, 1983.

[141] M. Suesser, K. G. Narayankhedkar, G. Krieg, and M. D. Atrey R. Rajini-Kumar, "Performance evaluation of metal-coated fiber Bragg grating sensors for sensing cryogenic temperature," vol. 48.

[142] C. A. Villarruel, C. K. Kirkendall, D. M. Dagenais, J. A. McVicker, A. R. Davis, S. S. Patrick, K. P. Koo, and A. Dandridge F. Bucholtz, "8 element array of 3-axis fiber optic magnetometers for undersea applications," 1994.

[143] S. T. Vohra, and F. Bucholtz, L. Fabiny, "Multiplexed Low-Frequency Electric and Magnetic Field Fiber Optic Sensors," vol. 2, 1996.

[144] S. Jiang, and J. R. Marciante L. Sun, "All-fiber optical magnetic-field sensor based on Faraday rotation in highly terbium-doped fiber," vol. 18, 2010.

[145] K. S. Lee, and S. H. Lim M. H. Kim, "Magnetostriction measurements of metallic glass ribbon by fiber-optic Mach-Zehnder interferometry," vol. 191, 1999.

[146] V. Matejec, and I. Paulicka M. Sedlar, "Optical fibre magnetic field sensors using ceramic magnetostrictive jackets," vol. 84, 2000.

[147] C. Shuying, D. Zhigang, W. Xiaoyang, S. Changhai, and C. Jianping W. Xin, "Experimental Study of Some Key Issues on Fiber-Optic Interferometric Sensors Detecting Weak Magnetic Field," vol. 8,

2008.

[148] P. D. Dinev, "A two-dimensional remote fibre-optic magnetic field and current sensor," vol. 7, 1996.

[149] H. Sohlstrom, and T. Brogardh) U. Holm, "Measurement system for magneto-optic sensor materials," vol. 17, 1984.

[150] J. X. Dai, C. M. Zhou, and D. S. Jiang M. H. Yang, "Optical fiber magnetic field sensors with TbDyFe magnetostrictive thin films as sensing materials," vol. 17, 2009.

[151] A. Gasparics, and Z. Vértesy G. Vértesy, "Improving the sensitivity of Fluxset magnetometer by processing of the sensor core," 1999.

[152] M. Scalora, C. M. Bowden, and S. L. Chin N. Akozbek, "White-light continuum generation and filamentation during the propagation of ultra-short laser pulses in air," vol. 191, no. 3-6, 2001.

8.1 Laser suppliers

For details of the laser specifications go to the links below;

Amplitude systemes: http://www.amplitude-systemes.com/

Coherent: http://www.coherent.com/Lasers/

High Q: http://www.highqlaser.at/en/products/

IMRA: http://www.imra.com/

Kapteyn-Murnane Laboratories: http://www.kmlabs.com/

Raydiance-Inc: http://www.raydiance-inc.com/our-products

Appendices

Appendix A

Polydimethylsiloxane (PDMS) on SU-8 Mold

1. Material Requirements:

1.1 Equipment: 4" wafer tweezers, polystyrene Petri dish, 2 pipettes, plastic spoon, plastic cup, razor blade, vacuum desiccator, Plasmod O_2 plasma asher, aluminum foil, hot plate, scale.

1.2 Preparation: You must prepare the SU-8 mold wafer prior to beginning the PDMS process.

This procedure is dealt with in a separate SOP.

1.3 Chemicals: PDMS, and silanizing agent (tridecafluoro-1,1,2,2-tetrahydrooctyl trichlorosilane)

1.3.1 Hazards associated with chemicals:

1.3.1.1 PDMS: May cause eye and skin irritation. May cause respiratory and digestive tract irritation.

1.3.1.2 Silanizing Agent: Corrosive. Causes sever irritation and burns. Harmful if ingested, inhaled, or absorbed through the skin. Lachrymator.

** Reacts violently with water releasing hydrogen chloride (HCL).

Incompatible with oxidizing agents, acids, alcohols, and bases. **

1.4 Engineering Controls: Conduct procedure in ventilated fume hood. Store bottles of chemicals (sealed tightly) in cabinets with secondary containment. Work area should contain an eye wash and safety shower.

1.5 Personal Protective Equipment: Nitrile gloves, apron, and goggles. While working in the hood, also use trionic gloves.

2.0 Procedure:

Complete all processes in the fume hood.

2.1 SU-8 Silanization – passivation of surfaces to aid release from PDMS:

2.1.1 Using wafer tweezers, place the SU-8 mold wafer along with 2-3 drops (use pipette) of the silanizing agent in a Petri dish and put in vacuum desiccator.

2.1.2 Attach the desiccator to a vacuum hose on the hood vacuum port. Open the faucet-style vacuum valve. Leave the wafer under vacuum for at least 1 hour.

2.2 Mix and Degas PDMS:

- Silicone raw material is very sticky. Tape a piece of aluminum foil down inside the

fume hood to act as a disposable work space. Place a piece of foil on top of the scale as

well.

2.2.1 Bring the scale into the fume hood. Place a plastic cup and spoon onto the scale

and tare.

2.2.2 Using the spoon to dispense the PDMS base and a pipette for the curing agent, weigh the PDMS pre-polymer components in a 10:1 (base:curing agent) ratio into the cup. Add the base first, making sure to weigh without the spoon in the cup. Pour a volume of base that is about equal to the total volume Add the curing agent next with the pipette. Mix well with the spoon (until mixture is milky due to air bubbles).

2.2.3 Turn off vacuum and remove the SU-8 wafer from the desiccator.

2.2.4 Put the PDMS mixture (in the cup!) into the desiccator and turn the vacuum back on. De-gas the mixture under vacuum until no bubbles appear (20~30 min). Make sure the PDMS mixture does not foam out of the container. When large bubbles form at the surface, vent vacuum to pop bubbles.

2.3 Pour PDMS:

2.3.1 Carefully pour the PDMS over the SU-8 master wafer already located in the polystyrene Petri dish.

2.3.2 Try to minimize introduction of bubbles.

2.4 Cure PDMS:

2.4.1 PDMS will cure without heating in ~24 hours.

2.4.2 To decrease cure time, place the Petri dish onto a hot plate (still in the Petri dish!) set at 65°C for ~1-2 hours (depending on the thickness of the PDMS layer).

2.4.3 After curing, the wafer is stable and may be stored for months if necessary.

2.5 Remove Mold:

2.5.1 Using tweezers (and a razor if necessary), carefully peel off the PDMS mold from the SU-8 master.

2.5.2 Cut the mold into the desired shape using razor blades, being careful to keep the mold clean.

2.6 Clean Up

2.6.1 Return all labware to the proper location.

2.6.2 Remove aluminum foil and wrap up all used materials and scraps. Discard in the photoresist waste container.

2.7 Oxidize Surfaces (if further bonding is required):

-- Read the March Plasmod SOP and the PDMS-Glass Bonding SOP before operation of asher.

2.7.1 Place the PDMS and glass pieces being bonded into the Tegal Plasmod plasma
cleaner with the surfaces to be bonded facing up.
2.7.2 Turn on the plasma cleaner and once plasma is stable, ash for 30 seconds.
2.7.3 The plasma oxidizes the surfaces creating dangling bonds which allow the PDMS to bond covalently to the glass. Over-ashing should be avoided due to a reduction in bond strength.
3.0 Storage:
3.1 Store PDMS components in the photoresist storage cabinet.
3.2 Store silanizing agent in solvents storage cabinet.
4.0 Waste Disposal:
4.1 Aluminum foil, cups, spoons, Petri dish, and wipes with PDMS on go in solvent/photoresist
waste container.
4.2 There should not be any silanizing agent left over… it should have evaporated away. If it has not, allow it to evaporate away in the hood and dispose of the container in solvent/photoresist trash.
4.3 Razor blades, broken glass or broken silicon waste goes in the "sharps" waste.
5.0 Accident Procedures:
5.1 Contact: Read MSDS prior to working with any chemical to familiarize yourself with the symptoms of exposure and recommendations for treatment.
5.1.1 Skin contact: Flush with water.
5.1.2 Eye contact: Flush with copious amounts of water for 15 minutes.
5.1.3 Ingestion: Do not induce vomiting. If conscious and alert, rinse mouth and drink 2-4 cupfuls of milk or water.
5.1.4 Inhalation: Remove to fresh air. Resuscitate if necessary.
5.2 Spill:

5.2.1 Any small spills should be wiped up immediately with wipes. Dispose the wipes in the photoresist waste container.

5.2.2 In case of large spill that you are not comfortable cleaning up, evacuate the lab and contact the lab manager and/or safety office. If at any time you feel a situation is dangerous, do not hesitate to call the safety office

Appendix B

A number of equations defining spiral groove bearing design and construction. They were set out by E. A. Muijderman in 1966 in the book *spiral groove bearings*. The terms are defined on in the list of terms on page 25.

$$F = \frac{3\pi\eta\omega R^4}{2h_0^2}(1 - \Delta D^4)g_1 C_2$$

$$g_1 = \frac{H^2\, cot(\alpha)\,(1-H)(1-H^3)}{(1+H^3)^2 + 4H^3\, cot(\alpha)^2}$$

$$H = \frac{\delta}{1+\delta}$$

$$\delta = \frac{h_0}{h_2}$$

$$\Delta D = \frac{r_i}{r_0}$$

$$C_2 = \frac{e^{\frac{-2\pi}{k}\left(1-\frac{2\alpha}{\pi}\right)tan(\alpha)} - \Delta D^4 e^{\frac{2\pi}{k}\left(1-\frac{2\alpha}{\pi}\right)tan(\alpha)}}{1 - \Delta D^4}$$